

**Construction of a Time Projection
Chamber as Focal Plane Detector
for MAGIX
and
Preparation of the Hoyle State
Measurement at MAGIX**

Dissertation

zur Erlangung des akademischen Grades
"Doktor der Naturwissenschaften"
am Fachbereich Physik, Mathematik und Informatik
der Johannes Gutenberg-Universität
Mainz

David Christian Alexander Gabriel Markus

MAINZ, 9. MÄRZ 2026



Autor

David Christian Alexander Gabriel Markus
MAGIX Kollaboration
Institut für Kernphysik
Johann-Joachim-Becher-Weg 45
Johannes Gutenberg-Universität
D-55128 Mainz
dmarkus@uni-mainz.de

Gutachter

Weitere Prüfungskommissionsmitglieder

Tag der Prüfung

1. Juni 2026

Abstract

As part of the PRISMA++ Cluster of Excellence, a new electron accelerator is currently being constructed at the Institute for Nuclear Physics at the Johannes Gutenberg University. This **Mainz Energy-recovering Superconducting Accelerator** (MESA) will host three experiments, whose goal it is to further our understanding of several areas of modern particle, nuclear, hadron, and astrophysics.

The innovative part of MESA is its capability to recapture part of the energy of the beam once it has passed an experiment. To fully utilize this capability, any experiment has to be designed with consideration of the requirements for the recapture. This has been done for the **Mainz Gas Injection Target Experiment**(MAGIX), which has been designed to be operated in an energy recovery mode to support beam recapture. MAGIX is in line to be the first experiment in the world to have a measurement run using this breakthrough technology.

To achieve this MAGIX employs a gas-jet target and will be run with no additional material in the beam or path of the scattering electron, minimising energy and precision loss by avoiding multiple scattering. Utilizing the 105 MeV beam at 1 mA beam current MAGIX aims to reach a luminosity of up to $1 \times 10^{35} \text{ cm}^{-2} \text{ s}^{-1}$. The detectors for MAGIX consist of two magnetic spectrometers which can rotate around the interaction point and which host two detector systems each: a focal plane tracking **Time Projection Chamber**(TPC), and a scintillator based Trigger Veto System.

With this setup, the focus is on areas that require very high precision high luminosity low energy data, one of which is the first planned experiment to be run at MAGIX, a measurement dedicated to the Hoyle State. The aim of this thesis is to show that MAGIX will soon be ready to take this data, with a specific focus on two major components, the simulation software and the focal plane detectors. As such, it is split into three parts.

The first part will deal with MESA and MAGIX, and the varied physics programs that will be run at them.

The second part deals with the focal plane TPCs of MAGIX by explaining the theory behind its construction, its major components and what has already been achieved with those components.

The third part deals with the preparation for the first measurement to be done at MAGIX. These preparations consisted of acquiring and characterising the target, preparing the theory, and writing simulation and analysis software.

Contents

I	The Mainz Gas Injection Target Experiment and its Multifaceted Physics Program	1
1	Physics of MAGIX	3
1.1	Dark Matter Physics	3
1.2	Electromagnetic Form Factors	6
1.3	Astrophysics	8
1.4	Few Body Physics	11
2	MAGIX and its Accelerator	13
2.1	MESA	14
2.1.1	Injector Section	15
2.1.2	Linac Section	16
2.1.3	P2	16
2.1.4	DarkMESA	17
2.2	MAGIX	19
2.2.1	Gas-Jet Target	19
2.2.2	Scattering Chamber	21
2.2.3	Silicon Strip Detectors	23
2.2.4	Beam Halo Veto	24
2.2.5	Alternate Targets	24
2.3	MAGIX - Spectrometers	25
2.4	MAGIX - Time Projection Chamber	30
2.5	MAGIX - Trigger Veto System	30
II	Constructing a Time Projection Chamber for Measuring Particle Tracks in the MAGIX Focal Plane	33
3	Theory of Gaseous Detectors in General and Time Projection Chambers in Specific	35
3.1	Gaseous Detectors	35
3.1.1	Ionisation in Gas	35
3.1.2	Drift	37
3.1.3	Diffusion	38
3.1.4	Charge Multiplication	39
3.2	TPC	40
3.2.1	Gas Mixture	41
3.2.2	GEM	43
3.2.3	Field Cage	44

3.2.4	Signal Processing	44
3.3	A short Interlude into Solid State Physics	46
3.3.1	UV LEDs	46
3.3.2	Photoelectric Effect	48
4	Design and Development of the Full Scale Focal Plane Time Projection Chamber	51
4.1	Structural Framing and Support Systems	52
4.1.1	Frame	53
4.1.2	Support Components inside the Spectrometer Housing	62
4.1.3	Support Components outside the Spectrometer Housing	63
4.2	Amplification Stage	64
4.2.1	Readout Anode	64
4.2.2	Four Layer GEM Stack	66
4.3	Readout Electronics	68
4.3.1	VMM Hybrids	70
4.3.2	FECs and DVMMs	72
4.3.3	VMM Configuration Registers	73
4.4	Field Cage	75
4.4.1	Active Area Field Cages	76
4.4.2	Open Field Cage Extension	76
4.5	Starry Night	78
4.5.1	Prototyping the Starry Night Concept	79
4.5.2	Designing a Starry Night	86
4.6	Software	89
4.6.1	Slow Control	89
4.6.2	Data Acquisition System	89
4.7	Analysis	91
5	Results	93
5.1	Amplification Stage	93
5.2	Starry Night	95
5.3	Construction	97
5.4	Conclusion	99
III Preparing the Target, Software and Analysis for the first Measurement at MAGIX		101
6	Preparing the Experimental Infrastructure for the first Measurement Run	103
6.1	Hoyle State	103
6.2	Signal Rates for Electron Scattering	104
7	Determining the Target Areal Thickness of the Diamond Target	107
7.1	Choosing a Target	107
7.2	Mach Zehnder Interferometers	108
7.3	Continuous Wavelet Transformation	110
7.4	Results	112

8	Electron Scattering Cross Sections	115
8.1	Electron Scattering	115
8.2	Form Factors	116
8.3	Distorted Wave Born Approximation	118
9	Monte Carlo Simulation with MXSim	121
9.1	Principles of Monte Carlo Simulation	121
9.2	MXSim	122
9.3	MXSim Modules for simulating the Hoyle State and its Background .	123
9.3.1	Inelastic and Elastic Scattering with GenerateHoyle	123
9.3.2	Generating the Beam	125
9.3.3	Target Integration with TargetDiamond	125
9.3.4	Cross Section Calculation with ModelHoyle	126
9.3.5	xfoubes and ELSEPA	126
9.3.6	Detector Simulation with MagixSpectrometer	130
9.4	Analysis	131
10	Results	133
10.1	Validating the Results	133
10.2	Expected Reach for the MAGIX Hoyle State Measurement	134
IV	Conclusion	143
	Conclusion	145

Part I

The Mainz Gas Injection Target Experiment and its Multifaceted Physics Program

Chapter 1

Physics of MAGIX

MAGIX will be the first experiment to run physics experiments utilizing a beam whose energy will be recovered after scattering on and passing through its target. As a consequence and result of this, MAGIX will be able to reach competitive luminosities while maintaining an exceptionally clean experimental environment. The MAGIX gas-jet target is also capable of providing a variety of gases as target. This makes MAGIX highly suitable for hosting high luminosity searches for rare particles, mainly those of the dark sector, as well as to provide high precision measurements of nuclear observables, ranging from the electromagnetic form factors of the proton to cross sections predicted by various few body theories as well as those of astrophysical relevance.

In the following chapter this multifaceted physics program will be investigated. The details of the setup to achieve these goals will be presented in the next chapter.

1.1 Dark Matter Physics

There are numerous astronomical observations that cannot be explained with the known interactions, provided by the Standard Model of Particle Physics and the General Theory of Relativity, of observable baryonic matter, measured by hundreds of observatories in different ways[1]. The most well researched disagreements of observations with models that can be validated by experiments on earth are baryon acoustic oscillations, rotation curves of galaxies, and gravitational lensing. Baryon acoustic oscillations as recorded in the cosmic microwave background reveal that the proportion of baryonic matter to the total gravitationally interacting matter is less than one. The rotation curves of galaxies show that mass distributions in galaxies do not correspond to observable luminous matter. Gravitational lensing of galaxies and galaxy clusters do not yield calculated mass distributions compatible with the observed mass distributions provided by measured emissions.

The best example of the last case is the Bullet Cluster, where two galaxy clusters 3.9 billion light years distant interpenetrated. The majority of the visible mass of the two clusters was intergalactic gas, which collided, slowing down and creating enough heat to radiate in the x-ray spectrum, while the stars continued without colliding due to the large distances between them. Measurements of the actual mass distribution of the two clusters by gravitational lensing, however, shows that the centre of mass of both clusters appears to have stayed with the stars of the galaxies, and not slowed down like the colliding gases did, as shown in figure 1.1[2]. The best

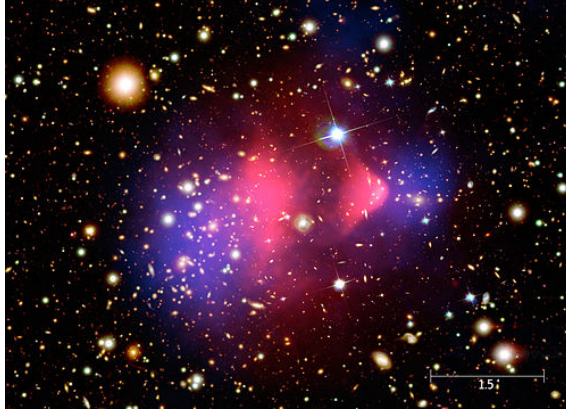


Figure 1.1: Reconstructed image of the collision between two galaxy clusters, labelled as 1E 0657-56, with the smaller cluster on right given the nickname bullet cluster for its shape. Background image of galaxies by the Magellan and Hubble Telescopes, superimposed by x-ray emission measured by the Chandra telescope in pink and mass distribution calculated from gravitational lensing in blue. Image from [3].

theories to explain this behaviour postulate an extension of the Standard Model with particles that interact only extremely weakly or not at all with all known particles and each other, but do have gravitational mass. Such particles would contribute to mass distributions on astronomical scales, but would be sufficiently hard to detect that we have not yet done so.

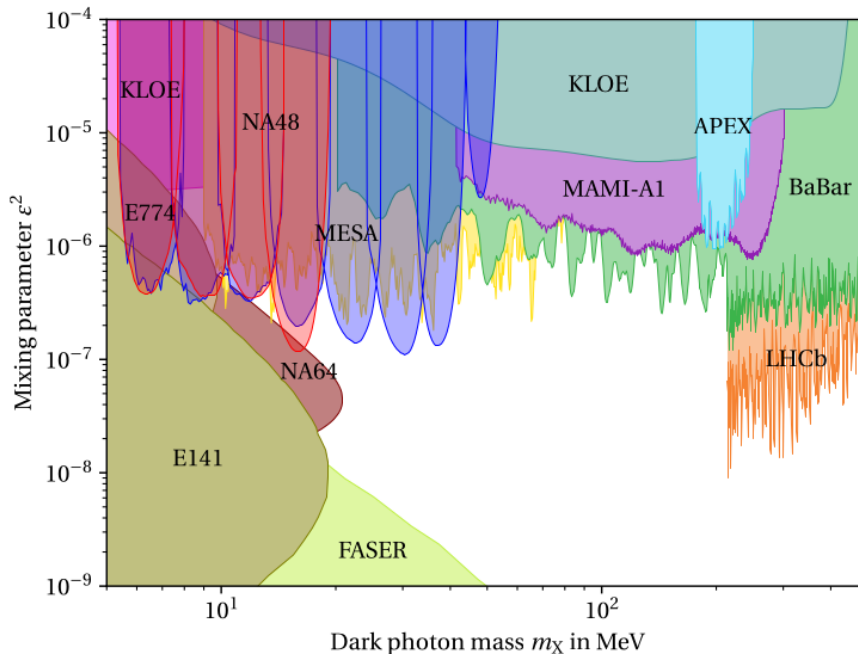


Figure 1.2: The γ' parameter space spanned by $m_{\gamma'}$ and ϵ for the dark photon electron positron pair production, with MAGIX - in red - compared to other experiments. Plot from [4].

Wide spanning searches have been conducted for signs of particles from this so-called dark sector, and have up to now been unsuccessful. Investigating the higher

energy reaches was promising in the past, but exceeded the energy region available to any accelerator. After the LHC did not discover any candidates at energies of up to 10 TeV, attention has turned back to particles of masses below 1 GeV, and to detecting signs not only of the particles themselves, but also of the messenger particle by which they interact with regular matter.

A simple model for this messenger particle assumes a similarity to a known force carrier, the photon, and as such postulates an extension of the Standard Model by an additional U(1) symmetry group, which generates a dark photon γ' with a mass $m_{\gamma'}$, which couples to a potential dark matter particle χ of mass m_χ with a dark fine structure constant α_D and to Standard Model particles with a mixing parameter ϵ [5].

In this model the presence of a dark photon could be detected via its various decay channels. Depending on whether it decays into Standard Model particles or not, the decay is termed visible or invisible, and each type requires different experimental treatment. MAGIX can contribute to searches for both scenarios. In both, a dark photon would be produced in a process equivalent to bremsstrahlung in an electron scattering of a heavy nucleus as the reaction $e^-Z \rightarrow e^-Z\gamma'$. The cross section of this process scales with Z^2 and so MAGIX would utilize a solid target for these measurements.

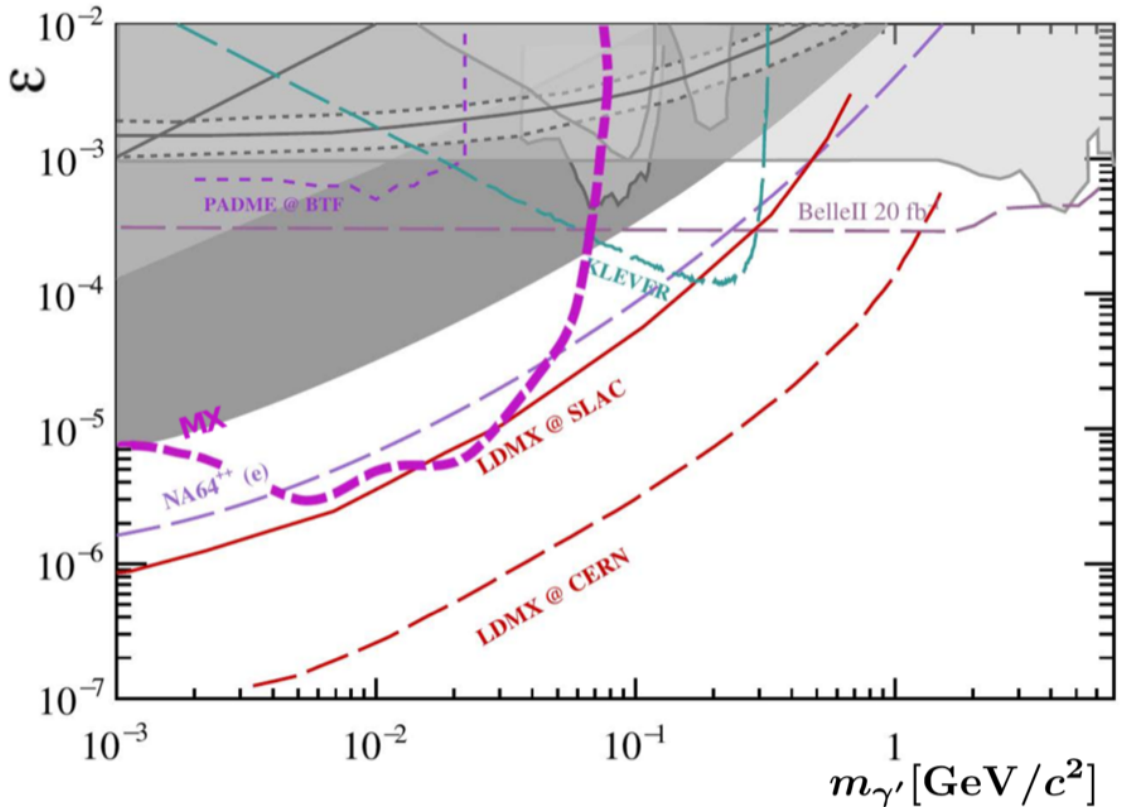


Figure 1.3: The γ' parameter space spanned by $m_{\gamma'}$ and ϵ for the dark photon invisible decay, with MAGIX - in purple - compared to other experiments. Plot from [6].

In the MAGIX kinematic region, the primary dark photon visible decays will be electron pair production $\gamma' \rightarrow e^-e^+$. A potential dark photon would thus manifest itself as a peak on the radiative tail of the invariant mass spectrum. The parameter

space MAGIX would be able to exclude in its first runs with tantalum is shown in figure 1.2.

For the invisible decay, the decay products could not be detected, and finding evidence of the dark photon would instead rely on detecting the missing mass it carried away. For this, a detection of the recoil nucleus as well as the scattered electron is required. To avoid complications due to nuclear excitations, hydrogen instead of a high Z gas would be used. The parameter space MAGIX would be able to exclude when searching for dark photon invisible decay is shown in figure 1.3.

1.2 Electromagnetic Form Factors

The electric and magnetic form factors G_E and G_M of a composite particle like a proton are the Fourier transforms of the distributions of charge and magnetization in the particle in the non-relativistic limit. From the form factors the charge radius r_E^p and magnetic radius r_M^p can be extracted as[7]:

$$(r_p^X)^2 = -6G'_x(Q^2 = 0). \quad (1.1)$$

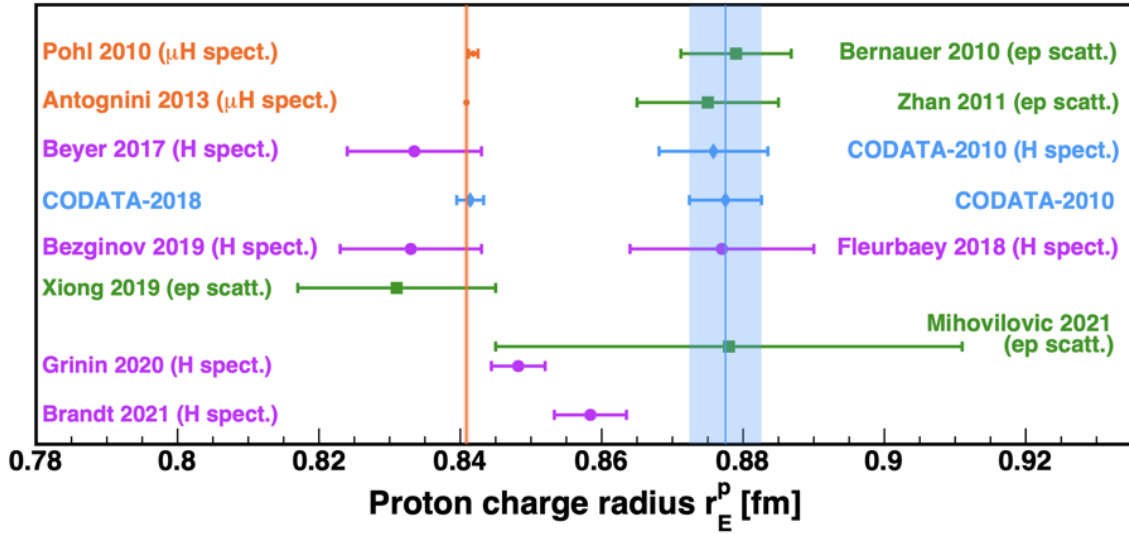


Figure 1.4: Overview of recent experimental results of the proton radius. Plot from [8].

The measurement accuracy of these form factors has significantly increased over time since their first determination by Hofstadter[9], which has led to an ever more precise determination of the charge radius of the proton. This was originally done in two ways: electron scattering measurements of the electric form factor at low Q^2 , from which the proton radius could be determined from extrapolation to $Q^2 = 0$ as per formula 1.1, and by spectroscopic measurements of atomic transitions of bound electrons in hydrogen, which accessed the same value directly[7]. Then, in 2010, a spectroscopic measurement of the proton radius using not electrons but muons was done, where a precision measurement of the lamb shift of the 2S-2P transition in muonic hydrogen was achieved. This gave a result with 7σ disagreement with the CODATA value of the time[10].

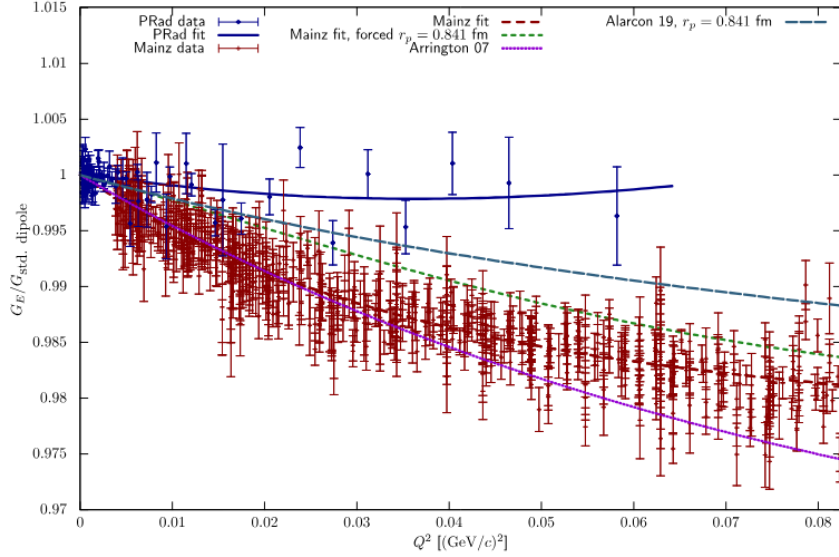


Figure 1.5: *PRad data and Mainz Data, with different fits. The Mainz data can be fitted to be in agreement with the current CODATA value for the proton radius, but are not by themselves in agreement with the data from PRad. Figure from [11].*

Since then, new results of all three measurement types have been published, which has led to the 2018 CODATA value of $r_p^E = 8.4075(64) \times 10^{-16}\text{m}$. An overview of the evolution of the measurements of the charge radius is shown in figure 1.4.

Two high precision low Q^2 electron proton scattering experimental data series have been released, one from PRad at JLab and one from the MAGIX predecessor experiment A1 at the MAInzer MIicrotron(MAMI). The same charge radius can be extracted from these data series using new theoretical models. However, the actual electric form factor data is not by itself in agreement between the two experiments, as shown in figure 1.5.

Now, both JLab, with its PRad2 experiment[12], and Mainz, with MAGIX, are aiming at generating new, higher precision electron proton scattering data at even lower Q^2 values. In addition, several other experiments are also aiming to contribute to resolving the electric form factor discrepancy. The MUon proton Scattering Experiment(MUSE) at the PSI π M1 beam line plans to generate muon proton scattering data as well as additional electron proton scattering data runs[13]. Apparatus for Meson and Baryon Experimental Research(AMBER) at CERN is planning to start taking data for muon proton scattering in 2026[14].

Besides the very well known proton charge radius puzzle, there also exist some tension in the value for the magnetic radius of the proton. This value is not as easily accessed by spectroscopic measurements as the charge radius, but can be calculated in Lattice QCD, which is not in full agreement with experimental results[15].

MAGIX will be able to contribute significantly to solving both these discrepancies by extending the reach and increasing the precision of form factor measurements, as shown in figure 1.6.

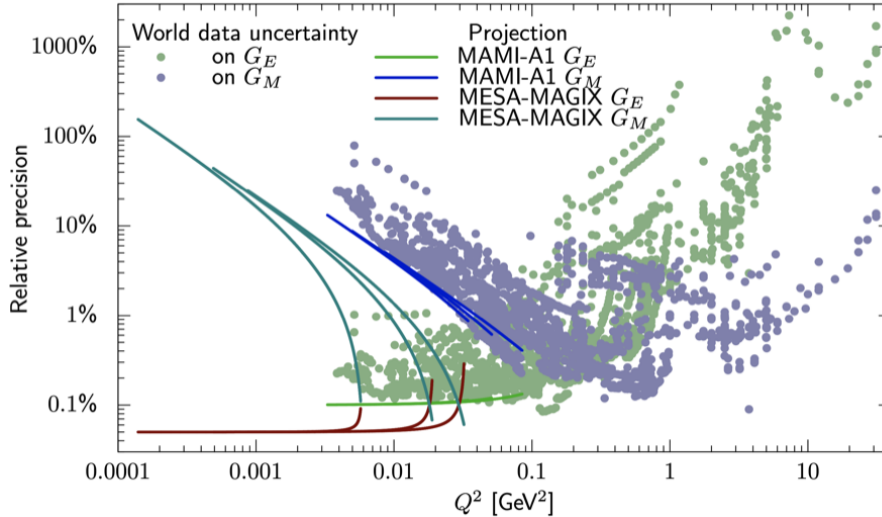


Figure 1.6: *Predicted precision for electric and magnetic form factor measurements at MAGIX, compared with world data uncertainties. Plot from [11].*

1.3 Astrophysics

One of the many subjects dealt with by astrophysicists is the question of how and where elements are created, and what explains their relative abundances. Following the big bang, after it was cool enough for hadrons to form, primordial nucleosynthesis created hydrogen and helium isotopes, and traces of the heavier elements like lithium and beryllium, distributed uniformly in the universe. All following nucleosyntheses took place heterogeneously in concentrations of matter, either steadily or very rapidly. Stars began to fuse light elements, with more massive stars creating heavier elements, up to the limit of exothermic fusion in stars of nickel 62, which has the highest binding energy per nucleon. Once at this point, stars reach an equilibrium for a short time where the temperatures facilitate the rate of α -particle production due to photodisintegration to equal the rate of α -capture. In this equilibrium, no more net energy is produced, even if α -capture would continue to be exothermic up to tin[16]. Once this happens, stars quickly collapse under gravitational pressure. The fusion of elements up to nickel 62 takes place in interdependent reaction chains and cycles, which have been organized in categories depending on their educts, such as carbon, oxygen, neon and silicon burning.

For hydrogen and helium, the two lightest and most abundant elements, being thus also the most involved components in nuclear fusion in stars, the reactions each happen in two distinct phases. For hydrogen, the proton-proton reaction chain is increasingly replaced by the CNO-cycle at higher temperatures, and as such higher masses, should the necessary catalytic component, carbon 12, be present. For helium, it is the triple- α and the α -process, where the former leads into the latter by producing the carbon necessary for its catalytic cycle. Later generations of stars incorporate the heavy elements of previous generations, changing their composition and which reactions are possible.

Elements exceeding the limit of exothermic fusion require more energetic events, such as the death of stars or the collision of neutron stars. Some rare light isotopes not involved in stellar nucleosynthesis are believed to be created as the result of

cosmic ray impacts on non-stellar matter, and some isotopes common on earth are the result of radioactive decay chains of the heaviest elements. The relative abundance of chemical elements therefore depends on a multitude of reaction rates and the history of stars and galaxies[17][18].

The rate at which fusion reactions occur depends on the abundances of the educts, the temperature T , which determines the relative velocity v and centre of mass energy E over the Maxwell-Boltzmann distribution, and the cross section. The cross section increases with higher energies, but the Maxwell-Boltzmann distribution tells us that higher energies are less common. The intersection between these two trends, the energies where the reaction is most likely to occur, are called the Gamow Peak. The plot in figure 1.7 shows that peak for three different reactions.

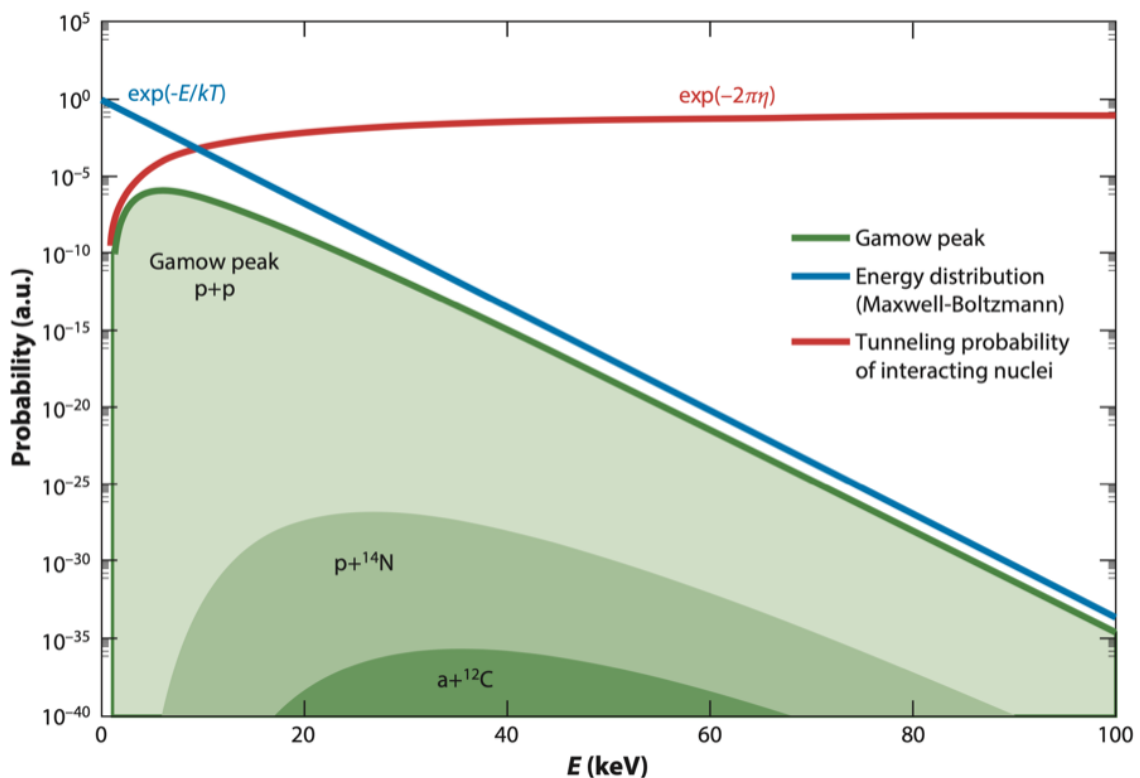


Figure 1.7: Reaction probability of three different nuclear fusion reactions in green, with the two contributing factors in red and blue. The fusion of heavier elements has its peak at higher energies. Plot from [19].

The cross section of a reaction is given by

$$\sigma(E) = \frac{1}{E} \exp(-2\pi Z_1 Z_2 \frac{\alpha c}{v}) S(E), \quad (1.2)$$

where the $1/E$ factor comes from the de Broglie wavelengths of the interacting nuclei, Z_1 and Z_2 are the atomic numbers of the involved nuclei, α is the fine structure constant and c is the speed of light. $Z_1 Z_2 \frac{\alpha c}{v}$ is often condensed as ν , the Sommerfeld parameter. The factor $S(E)$ contains the nuclear physics effects of the reaction, which are treated phenomenologically and extracted from experimental data. It is called the astrophysical S-Factor of that reaction[19][20].

One of the reactions currently under intensive investigation for their impact on predictions of isotope abundances is the alpha capture of a carbon 12, $^{12}\text{C}(\alpha, \gamma)^{16}\text{O}$,

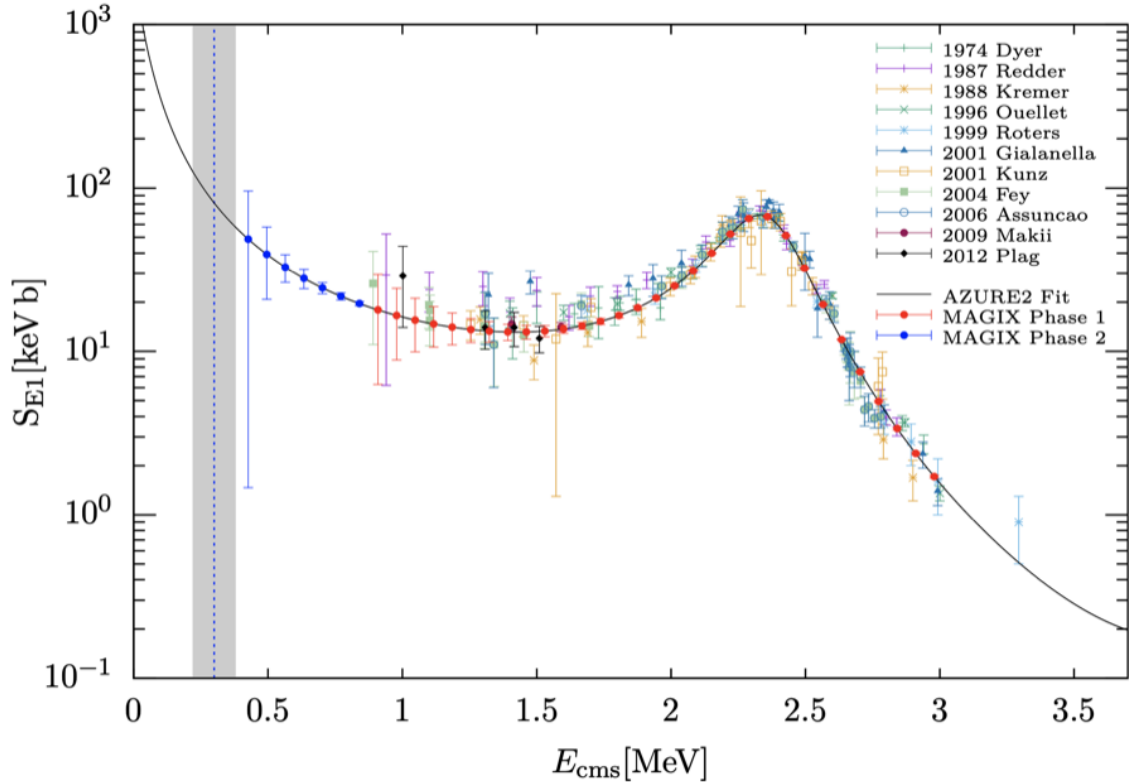


Figure 1.8: Projection of the reach of MAGIX for the S-Factor of the $^{12}\text{C}(\alpha, \gamma)^{16}\text{O}$ reaction, with existing experiments and a fit from the AZURE2 software into the region of interest. Figures from [20].

as it is one of the processes responsible for the relative abundance of carbon and oxygen, with its significant role into both stellar nucleosynthesis and biological life on earth. The current limit for the accuracy of the prediction at which rate this reaction occurs in stars is the accuracy of the S-Factor of the reaction in the energy region of interest. This limit exists, because the cross section of the reaction has to be measured at very low energies, around 300 keV and up to now, no experiment has measured the S-Factor at centre-of-mass energies much lower than 1 MeV. For predictions of the stellar production rate, the S-Factor therefore has to be extrapolated to lower energies.

MAGIX plans to lower the energy limit of this measurement not by measuring the reaction directly, but instead by extracting the S-Factor from a measurement with a much higher cross section that shares that S-Factor: the electro-disintegration of oxygen, $^{16}\text{O}(e, e'\alpha)^{12}\text{C}$. This reaction shares a time reversed interaction vertex with the reaction of interest and as such has the S-Factor as part of its cross section. For this measurement, MAGIX will use oxygen 16 as a target, and utilize its silicon strip detectors for the measurement of the recoil α -particles and one of its spectrometers for the scattered electron, to first reach 900 keV at higher precision than previously achieved experimentally in Phase 1. In Phase 2, there are plans for an additional forward spectrometer to operate as a zero degree tagger. This would measure electrons scattered at extreme forward angles, allowing us to reach energies as low as 400 keV. The expected reach is shown in figure 1.8.

The method of measuring the time reversed interaction vertex can also be used

for other reactions involving α , proton or neutron capture that are of relevance in astrophysics, such as the α -capture of deuterium, ${}^2\text{H}(\alpha, \gamma){}^6\text{Li}$.

1.4 Few Body Physics

Quantum Chromodynamics(QCD) is the theory describing the behaviour of the strong nuclear force and as such is the foundation for calculations of the behaviour of quarks bound into hadrons by the QCD carrier particle, the gluon. Unlike for QED, a QCD perturbation theory cannot easily be established at energies relevant to nuclear physics due to its coupling constant increasing with lower energies. This leads to confinement, where the particles carrying the QCD charge equivalent, colour, cannot be isolated. At the energy scales of bound, stable hadrons, this results in the degrees of freedom not being the quarks and gluons themselves, but rather their bound states, lower mass hadrons. Due to this, QCD is theoretically and computationally complex.

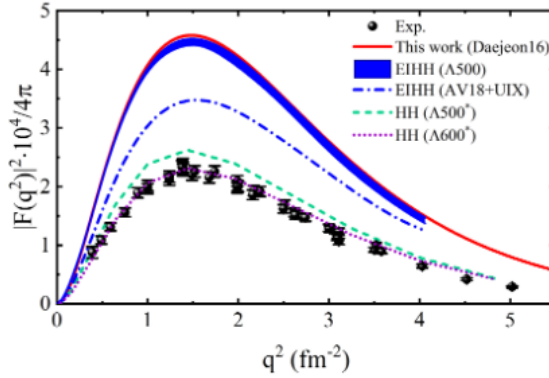


Figure 1.9: *Transition form factor of the α -particle monopole transition $0_+^1 \rightarrow 0_+^2$ as a function of the squared three-momentum transfer q , from theoretical calculations and data from inelastic electron scattering. Plot from [21].*

Ab-initio calculations are capable of providing accurate predictions for simple bound systems such as protons and neutrons[22], but fail at higher complexity. Theoretical research in this area first led to Chiral perturbation theory, which was then generalized into Chiral Effective Field theory. χ EFT, as the name implies, is an effective field theory that makes use of the chiral symmetries of low energy QCD and removes the contributions of the high energy scales that involve quarks and gluons, thereby reducing the degrees of freedom to hadrons in the form of pions and nucleons. From this, an effective Lagrangian is constructed that can be used to derive multi nucleon forces, which allows predictions of the behaviour of complex hadronic systems[23]. To calibrate and validate this theory, more high precision experimental data is required. One example of this, for which MAGIX is ideally suited to provide that data, is the $0_+^1 \rightarrow 0_+^2$ monopole transition in helium 4, as shown in figure 1.9. The ground state of four bound nucleons, two protons and two neutrons, can be described to sub-percent accuracy. However, the first excited state 0_+^2 is still heavily dependent on the choice of model. Recent theoretical results for this transition form factor from Yin et al[21] agree with previous calculations[24], but exceed the latest experimental results by more than a factor 2 at a q^2 of 1.5 fm^{-2} .

Chapter 2

MAGIX and its Accelerator

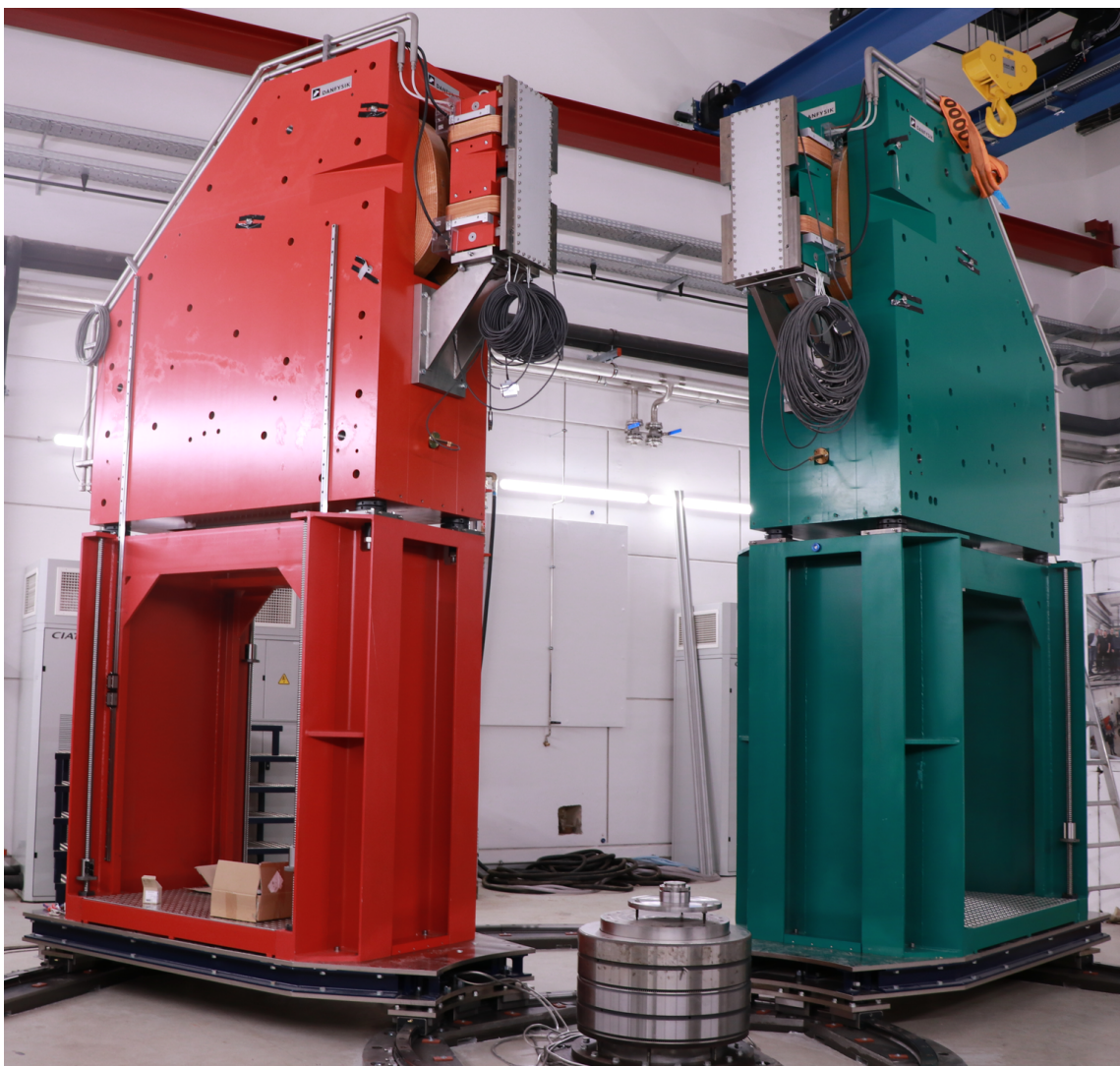


Figure 2.1: *MAGIX Spectrometers, after installation of the magnet system, but before installation of the detectors. The red spectrometer on left is called PORT, the green on the right STAR, referencing nautical navigations buoys.*

To achieve the goals presented in the previous chapter, the MAGIX setup has to accomplish a number of design goals. To start at the beginning, with the funda-

mental idea for the new accelerator, the beam that will be delivered to MAGIX is intended to be recirculated to achieve much higher intensities than otherwise possible. This ambitious goal places numerous requirements on the instruments and facilities of the accelerator itself, but also has major implications for MAGIX, with the primary and most difficult being that the beam has to pass the experiment with minimal interaction, reducing multiple scattering and preserving emittance. Only by the experiment minimally interacting with the beam is it possible to recover its energy.

To achieve this, MAGIX has to operate with a limit on the total areal thickness the beam interacts with. This limit means that the only material we can allow to enter the path of the beam is that of the target itself, and that the thickness of that target has to be tightly controlled. This means we need a windowless target setup and a gaseous target. However, these restraints also ensure that the experimental environment will be free of a major source of background, allowing for much higher precision.

The following chapter begins with an explanation of the **Mainz Energy Recovering Superconducting Accelerator**(MESA), with its major components and the two other experiments it hosts, P2 and DarkMESA. The rest of the chapter deals with MAGIX, with its two major components, the gas-jet target and the magnetic spectrometers, which contain the two major detector systems, the Time Projection Chamber and the Trigger Veto System.

2.1 MESA

MESA is the low energy quasi-continuous-wave recirculating electron linear accelerator that is currently under construction at the Institute for Nuclear Physics on the campus of the Johannes Gutenberg University in Mainz, Germany. The funding for this accelerator was mainly provided by the PRISMA++ cluster of excellence. The construction of new and refurbishment of existing halls for the facility were completed at the end of 2023. It is currently planned to have a first beam around June 2027. MESA's design principles, as part of providing an energy recovering beam, place a heavy focus on beam quality and intensity, to allow for high precision particle and nuclear physics experiments.

The MESA halls house the two major components of the accelerator itself, the injection section and the linac section with two cryomodules housing two superconducting accelerator cavities each, and its recirculating arcs, as well as three experiments, P2, DarkMESA and MAGIX. A floor plan is shown in figure 2.2. For more information about MESA see the dissertation of Daniel Simon[25], which was used as the main source for this section.

P2 and DarkMESA will only be operated in the first mode of MESA, the **Extracted Beam**(EB) mode. For this, no energy recovery takes place, since the P2 target is liquid hydrogen, which requires containment. The EB mode delivers a maximum beam energy of 155 MeV at a maximum current of 0.15 mA. In the EB mode, the beam will reach a polarization of over 85%. P2 will make use of this highly polarized beam to measure the weak mixing angle and expects to reach a luminosity of $2.38 \times 10^{39} \text{ cm}^{-2} \text{ s}^{-1}$ [26]. DarkMESA operates parasitically to P2 and will conduct light dark matter searches[5].

Only MAGIX will operate in the second mode, the **Energy Recovery Linac**(ERL)

mode, where beam recirculation will take place. For the ERL mode, the beam passes through MAGIX, and is reinjected into the linac section, with a phase shift of the entry timing of the beam relative to the accelerator cavity standing electric field of 180° , meaning the electrons will lose energy to the field instead of gaining it. This energy recovery allows for an increase in beam current to 1 mA, with plans to reach 10 mA in the future. The ERL mode provides an unpolarized electron beam with a maximum energy of 105 MeV. Depending on setup and beam current, MAGIX can reach its intended luminosity of up to $1 \times 10^{35} \text{ cm}^{-2} \text{ s}^{-1}$. MAGIX, in the beginning and when making use of solid targets, will also be operated in the EB mode.

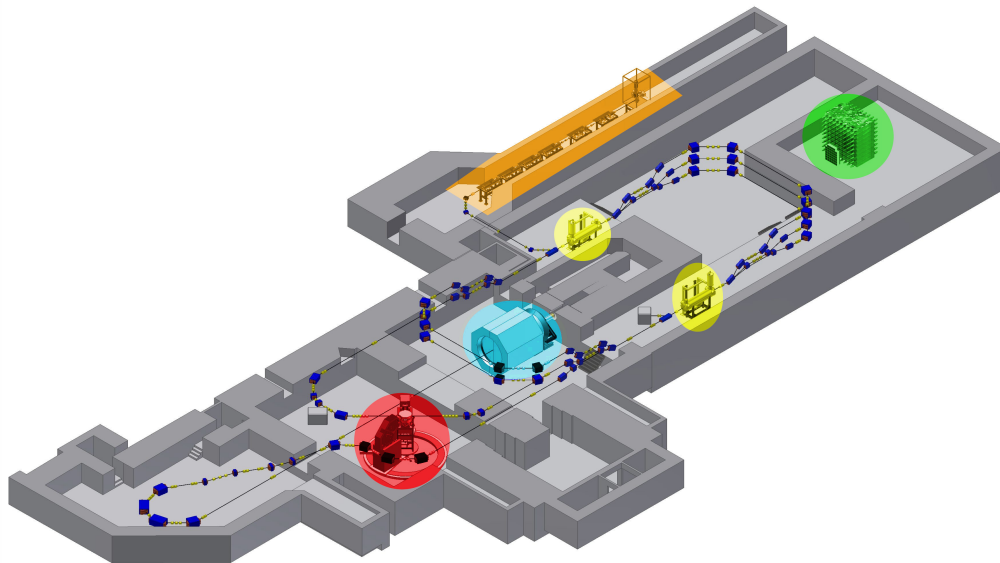


Figure 2.2: *Schematic drawing of the MESA facility, with the injector section coloured in orange, the accelerator cavities at the heart of the linac section in yellow, P2 in blue, DarkMESA in green and MAGIX in red. Modified image from [25].*

2.1.1 Injector Section

The MESA beam originates in one of two possible photoguns: either in the polarized **S**mall **T**hermalized **E**lectron **S**ource **A**t **M**ainz (STEAM), or the unpolarized **M**ESA-**I**njector **S**ource **T**wo (MIST). In both of these, a pulsed laser beam triggers the photoeffect in a photocathode, causing it to emit electrons. STEAM uses a gallium arsenide based superlattice to achieve a beam current of up to 1 mA with a polarisation of up to 85%. MIST is planned for a higher beam intensity of up to 10 mA, but does not require the beam to be polarized and so uses a more robust caesium potassium antimonide photocathode[27].

The created electrons are accelerated to 100 keV and directed into the beam preparation system **M**ESA **L**ow-energy **B**eam **A**pparatus (MELBA). MELBA utilizes two Wien-filters combined with a solenoid magnet to freely decide the beam polarization direction, and a chopper-buncher system. The pulsed laser already creates particle bunches with the intended operation frequency of 1.3 GHz, the chopper-buncher system increases the quality and tightness of the bunches. After this, the beam is guided into the normal-conducting booster linac **M**illi**A**Mpere **B**Ooster (MAMBO). MAMBO accelerates the electrons to 5 MeV, at which energy further acceleration

no longer meaningfully increases their speed. With this boost, the beam enters the linac section.

2.1.2 Linac Section

After reaching near light speed, accelerator cavities no longer need to account for a change of speed. As such, a beam can pass through the same cavity multiple times. At MAMI, the prior generation accelerator in Mainz, this is utilized extensively in a racetrack microtron setup, where the beam would pass through the same cavity several dozen times. MESA instead uses superconducting cavities, which allow for much higher electric field gradients and so greater acceleration per pass. In total four **S**uperconducting **R**adio **F**requency(SRF) cavities of the **T**eraelectronvolt **E**nergy **S**uperconducting **L**inear **A**ccelerator(TESLA) type are installed, in two **E**lectron **L**inac for **B**eam with **H**igh **B**rilliance and **L**ow **E**mittance(ELBE) cryomodules, two in each, called the **M**ESA **E**nhanced **E**LBE **C**ryomodules(MEEC).

Each SRF cavity provides up to 12.5 MeV acceleration or deceleration for passing electrons, with the fields oscillating at the same operation frequency as bunches are created by MELBA, 1.3 GHz. A single pass through a module means a change in energy of up to 25 MeV and a complete circulation through both modules up to 50 MeV. Connecting the MEECs are the recirculation arcs. Each energy requires its own arc, with lower energy beams running in higher arcs.

Adjusting the energy gains in the MEECs and the number of circulations allows for some control of the beam energy, with EB mode operation ranging from an as to now undefined energy somewhere below 30 MeV to the full 155 MeV. After the beam passes the P2 experiment, it terminates in the P2 beam dump.

ERL operation is limited to two circulations and a minimum energy of 30 MeV by the specific injection-extraction-chicane in use for it. Decelerated electrons with their remaining 5 MeV that cannot be regained will terminate in the ERL beam-dump.

To operate MAGIX in the EB mode a separate beam dump in the MAGIX hall is required, since the beam cannot be reinjected into the accelerator.

2.1.3 P2

The P2 experiment aims to measure the parity-violating cross section asymmetry A^{PV} of elastic electron-proton scattering. This asymmetry arises from the weak charge of the proton $Q_{\text{W}}(\text{p})$ and is in the order of 10^{-8} . It will be the smallest asymmetry measured so far in electron scattering experiments. From the weak charge of the proton, the weak mixing angle $\sin^2\Theta_{\text{W}}$ can be extracted. If the measurement goals are reached, this value will be determined to a precision of 0.15% at a four-momentum transfer value of $Q^2 = 4.5 \times 10^{-3}\text{GeV}^{-2}$. This precise determination serves as another test for the Standard Model and a potential hint for physics going beyond it[26].

P2 will operate in the EB mode and requires both a maximally high polarization and a precise measurement of that polarization. To achieve this, a total of three polarimeters will be employed: a double Mott polarimeter as part of the electron source STEAM, a single Mott polarimeter at the end of MAMBO, and a Møller polarimeter after the last beam line arc aligned to the target.

Said target consists of a 60 cm tube filled with liquid hydrogen, which is surrounded

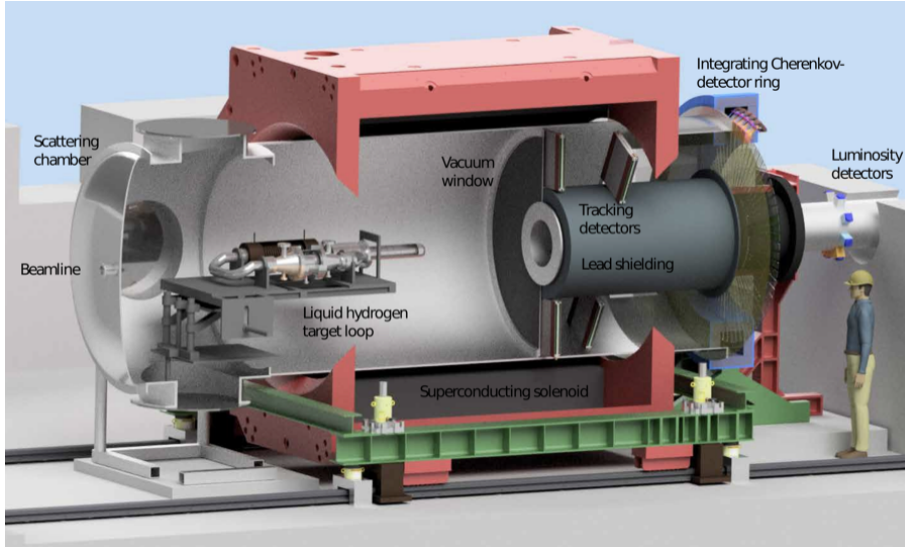


Figure 2.3: *Construction Model of the P2 setup. Figure from [28].*

by a scattering chamber under vacuum, which is in turn surrounded by a superconducting solenoid spectrometer. Forward scattered electrons leave the scattering chamber through a carbon fibre window and enter the tracking section, which is filled with liquid helium for detector cooling purposes and equipped with **H**igh **V**oltage - **M**onolithic **A**ctive **P**ixel(**HV-MAP**) detectors to determine Q^2 . Behind the tracking section, protected by a lead shield except where elastically scattered electrons under forward direction are expected, lie the integrating Cherenkov detectors, which are used to measure the electron asymmetry. Most electrons leave the scattering chamber through the exit beam line, along which the luminosity monitoring section are placed. An overview of the P2 components is shown in figure 2.3.

Finally, after leaving the exit beam line, the beam terminates in the P2 beam dump, which can also be considered the target of DarkMESA, as it operates in tandem with P2.

2.1.4 DarkMESA

DarkMESA is intended to search for indications of a potential dark sector, the theory of which is explained in section 1.1.

Should exchange particles of that dark sector, like the dark photon, exist, they could be created in bremsstrahlung-like processes in the beam dump of P2. After that, they could potentially create a pair of dark matter particles, which could in turn interact with regular matter, either electrons or nucleons. The recoil of that interaction can be detected. A visualization of the idea behind DarkMESA is shown in figure 2.5.

The rate at which these particles would be created and detected in this setup, which depends on the mass of the dark sector particles and the dark photon, as well as its interaction strength, is constrained by existing experiments. To set new limits the number of expected events is extremely low, requiring a very tight control of potential background.

As such, DarkMESA is separated from the beam dump, the biggest source of Standard Model background noise, by 15 m of air and 8 m concrete, and by 10 m of earth

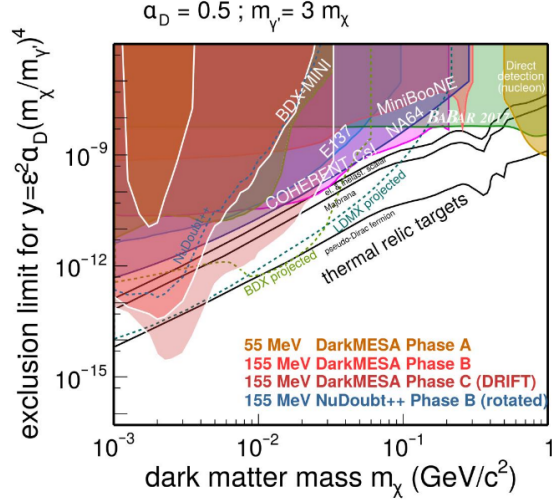


Figure 2.4: Expected reach for the different phases of DarkMESA. Figure from [29].

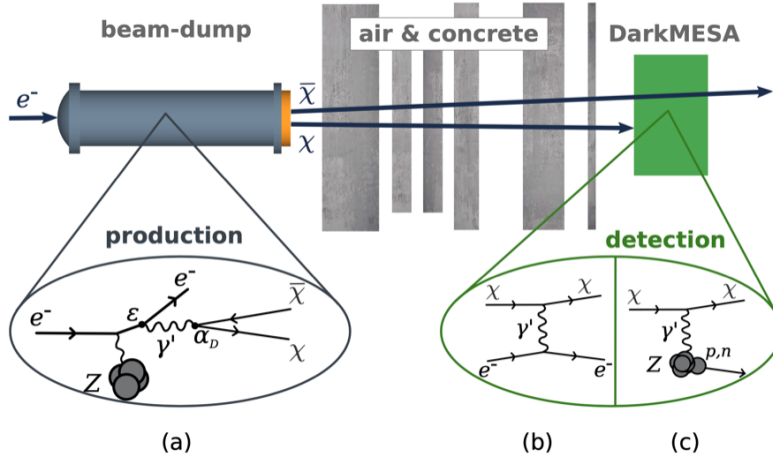


Figure 2.5: A visualization of the idea behind DarkMESA with Feynman diagrams of production and detection of dark matter particles. Figure from [5].

and concrete from the second-biggest source, cosmic background. Any potential dark sector particles would not be stopped in this material.

Construction of DarkMESA will take place in multiple phases, with a prototype Phase A already finished. The principal design consideration is increasing the signal-to-noise ratio, by first increasing the probability of dark matter detection by utilizing a high Z material in the form of high-density Cherenkov crystals, and second using multiple layers of vetoes and shielding to reduce Standard Model background. Figure 2.6 shows a concept drawing of the first two phases.

Phase B intends to multiply the existing prototype and supplement it with an additional wall of a second type of Cherenkov crystal. There are currently multiple ideas for a potential Phase C, ranging from several methods to reduce background by improving veto capability to increasing signal background discrimination capacity by increasing signal height with the addition of new types of detector crystals. For more information, see the dissertations of Matteo Lauss[30] and Mirco Christman[5]. Now that the accelerator MESA and the other two experiments hosted at it have

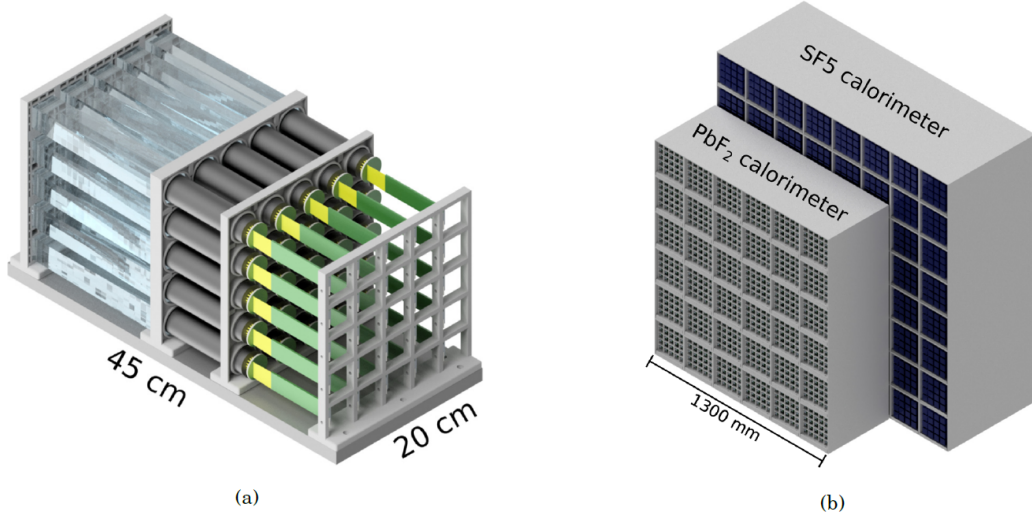


Figure 2.6: *Concept drawings of DarkMESA Phase A (a) and Phase B (b). Phase A will utilize 25 PbF₂ crystals, Phase B expands that to 900 PbF₂ and 1024 SF₅ crystals in two sections. Images from [5].*

been explained, we turn to MAGIX and its major components.

2.2 MAGIX

MAGIX intends to measure electron scattering reactions utilizing a gas-jet as its target, two high resolution magnetic spectrometers as its instruments, a **Time Projection Chamber**(TPC) as its focal plane detector, and an assembly of plastic scintillators as combined trigger and veto system. Electrons from the MESA beam will scatter of its target and some of them will be within the acceptance of our spectrometers. Accepted electrons enter the magnetic fields of the spectrometers, where they are bent and focused onto a focal plane. The tracks of the particles within that focal plane are measured by the TPC, allowing event-wise reconstruction of the scattering event. After passing through the TPC, the scattered electrons enter the trigger veto system, where their precise arrival times are determined, and optionally used to detect coincidences between the spectrometers. Potential background, from the accelerator, beam dumps, or of cosmic origin, is vetoed by means of particle type, energy, and travel direction.

These components of MAGIX will now be explained, beginning with the one at its physical centre, the gas-jet target.

2.2.1 Gas-Jet Target

MAGIX supports operations with an energy recovering accelerator by using a coherent stream of particles as target. In other words, a beam of molecules that does not require any material to contain it. To achieve acceptable target densities, neither so high as to impede energy recovery of the beam electrons, nor so low as not make experiments infeasible due to lacking luminosity, this requires cooling the gases. The MAGIX target based on this technology was developed by the AG Khoukaz of the University of Münster and is called a cryogenic supersonic gas-jet target. A sketch

of the principal of its operation is shown in figure 2.7, and a CAD model of the apparatus generating this gas-jet in figure 2.8.

At its core lies the idea of cooling a gas close to its condensation point and then sending it at high pressures through a Laval nozzle. As the gas is forced through the narrow opening of the nozzle the shape of that Laval nozzle causes some of the thermal energy of the gas to turn into kinetic energy, simultaneously condensing the gas and accelerating it to supersonic speeds. The thus produced particle stream is then ejected into the scattering chamber, where it crosses the electron beam in the interaction point. After that, it reaches a catcher, where the gas beam is extracted using a pumping cascade setup.

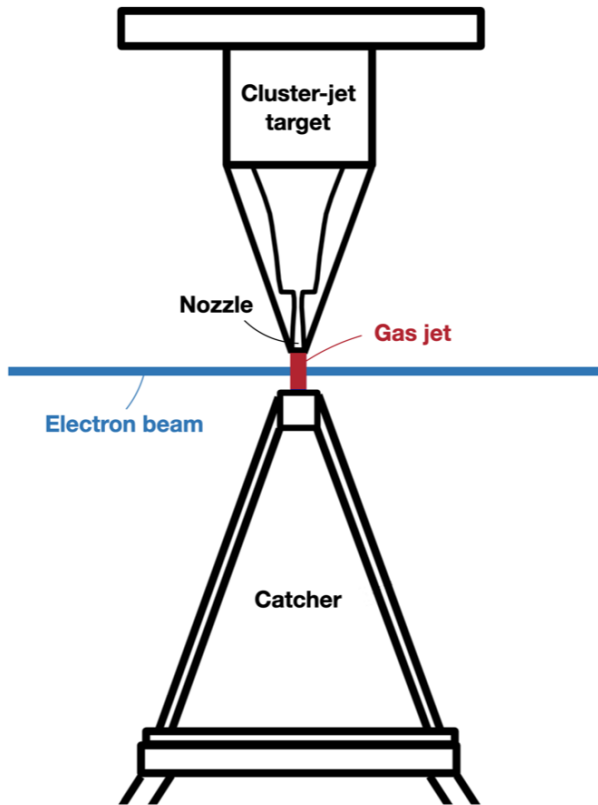


Figure 2.7: *Principal of operation of a gas-jet target with a Laval nozzle.*

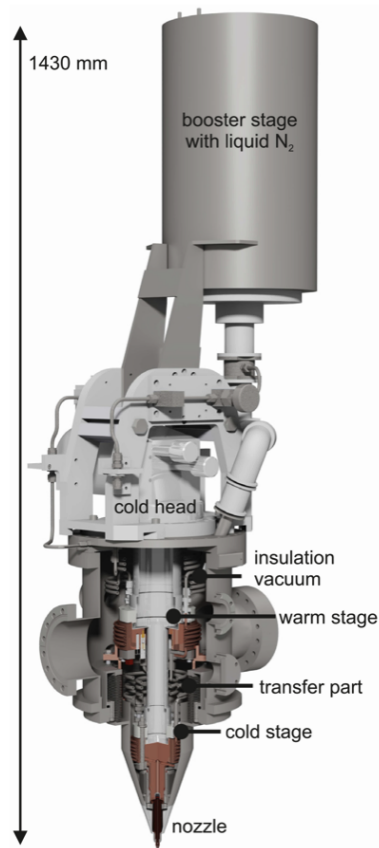


Figure 2.8: *CAD Model of the MAGIX gas-jet target apparatus. Figure from [31].*

This setup is usable with a variety of gases, with the main ones currently planned to be used being hydrogen, helium, argon, oxygen, nitrogen and xenon. Each gas requires individual consideration and variation in operation due to variance in phase diagrams and chemical inertness.

A test of this gas-jet target at A1 has shown that using hydrogen while operating at 40 K and 15 bar with a flow of 40 L min^{-1} creates a particle density of $1.6 \times 10^{18} \text{ atoms/cm}^2$ while reducing the vacuum in the scattering chamber from around 10^{-8} mbar to 10^{-1} mbar . With a beam current of 1 mA, corresponding to a particle rate of $I/e = 6.2 \cdot 10^{15} \text{ atoms second}^{-1}$, this equates to a luminosity of around $1 \times 10^{34} \text{ cm}^{-2} \text{ s}^{-1}$ [32]. For this, it is assumed that the MESA beam spot at the interaction of MAGIX will have a Gaussian profile with a standard deviation in

both directions of 100 μm .

Besides this more generally applicable type of operation, recently a prototype for a droplet type target intended for operation specifically with hydrogen has been completed. Hydrogen can be brought close to its triple point and liquefied, such that slight cooling is sufficient to freeze it. When the stream of liquid is periodically interrupted with a piezo actuator, this creates solid pellets of hydrogen that can travel considerable distance. One such target has been prototyped for operation at PANDA, where these pellets have to cross more than 2 meters until they reach the interaction point[33].

Further development of the droplet target has created the concept of a filament target, where the actuator is tuned such that the stream of liquid hydrogen is no longer disrupted sufficiently to form droplets and instead generates a solid filament. This would allow an order of magnitude increase of particle density to 4.5×10^{19} atoms/cm². However, as this also reduces the absolute size of the particle stream in the interaction point and so the overlap with the electron, this only means an increase in luminosity of a factor 4. Additionally, it reduces gas flow to 160 mL min⁻¹ and decreases the vacuum pressure by three order of magnitude due to much tighter containment and less loss of gas from the solid surface of the filament, compared to the liquid surface of the clusters[34].

The operation of the gas-jet target, and indeed MAGIX's other targets, requires a place for the interaction with the electron beam to take place in a vacuum, which is provided by the scattering chamber.

2.2.2 Scattering Chamber

The interaction point is surrounded by a vacuum containment vessel, the scattering chamber, that besides the nozzle of the gas-jet target also houses two auxiliary detector systems and an alternate target ladder. The scattering chamber also has to be connected to the two spectrometers of MAGIX, the main detector systems for scattered electrons.

This connection has to be windowless, to maintain the advantage of a low material budget given by the gas-jet target design. These connections present the biggest challenge with the construction of the scattering chamber, because they are intended to be freely rotatable around the interaction point.

To maintain a shared vacuum while moving the spectrometers will require a sliding seal, where the walls of the chamber and the flange of spectrometer would slide relative to each other, for instance on polytetrafluoroethylene surfaces. As an additional complication, this sliding seal will have to operate without the use of lubricating or sealing liquids, which would escape into the vacuum and degrade the performance of high performance turbo pumps necessary to maintain a beam quality vacuum.

Until the completion of a technical implementation of this design, a preliminary fixed angle multi-flange design will be used, where each spectrometer repositioning requires breaking vacuum and reconnection of the spectrometer connection.

The jet target catcher, directly under the interaction point, is connected to a high power pumping cascade to keep the vacuum contamination, caused by surface evaporation of jet target molecules, contained to the scattering chamber as much as possible. In line with the interaction point are also the electron beam ingress and egress pipes, along which are mounted additional differential pumping systems, to

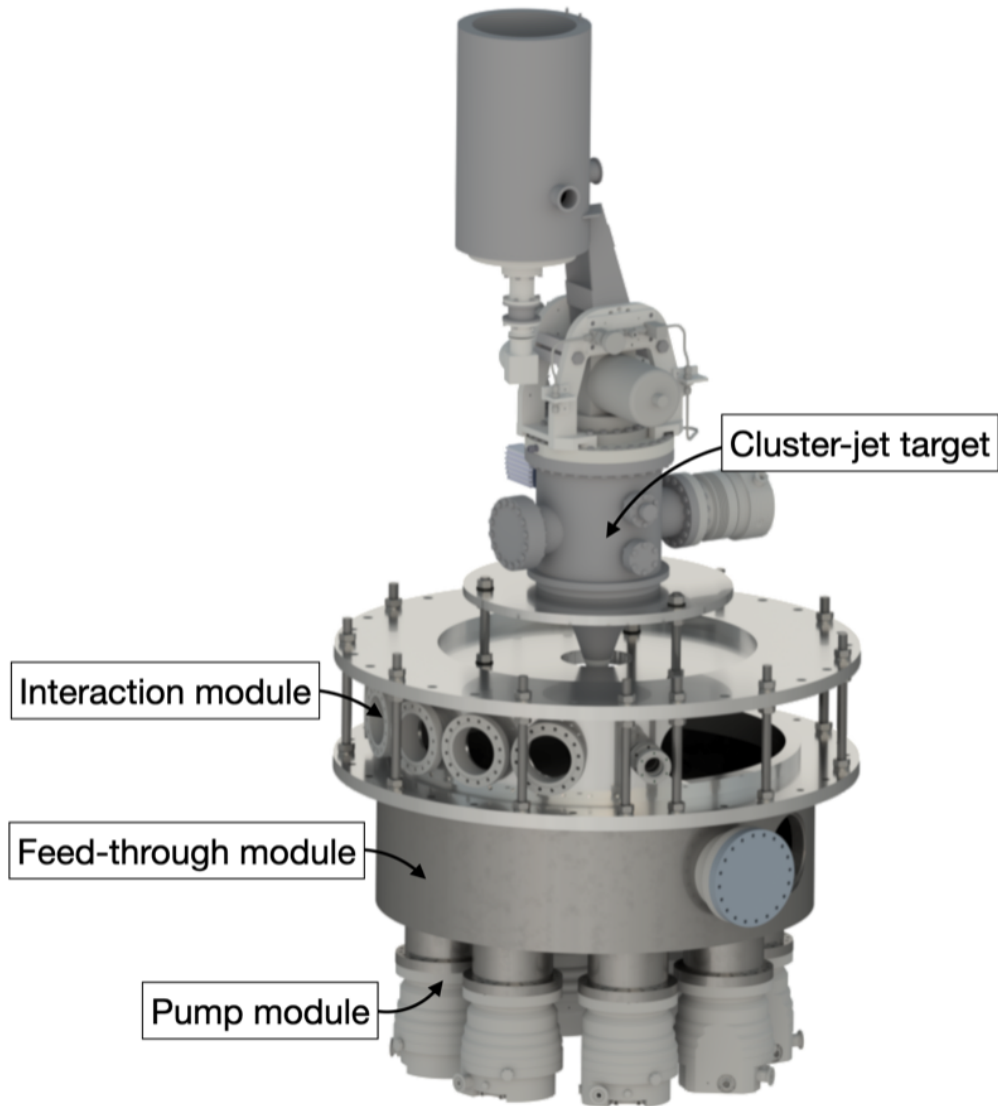


Figure 2.9: *Design sketch of the MAGIX scattering chamber, with the jet target from figure 2.8 at the top, followed by the interaction module, showing the beam entry pipe in the middle, with an opening to the left and the flanges of the preliminary fixed angle design to the left. The feed-through module below that is intended for the electrical and signal connections to the components in the chamber. At the very bottom, the pumping stage is visible. Figure from [35].*

aid and ideally eliminate the drift of target molecules from the contaminated scattering chamber into the rest of the accelerator beam line. With all these measures, we are aiming for a maximum of 10^{-6} mbar at the beam entry and exit points into the differential pumping systems.

Further along in both directions are also sets of five focusing quadrupoles and in forward direction the first bending dipole will also be used as a forward spectrometer, to extend to possible energy range and to serve as luminosity monitor.

A current design sketch is shown in figure 2.9. It consists of three separate modules, due to the differing requirement and increasing difficulty and risk of constructing a single shared vacuum chamber. The interaction module is supported by the feed-through module below, which contains the openings for bringing signal and power

lines out of and into the interaction chamber, and the pump module, which connects to the catcher.

The connection to the accelerator beam line both forwards and backwards hosts additional differential pumping systems, as a further measure to reduce any drift of target gas molecules into the vacuum of the accelerator.

2.2.3 Silicon Strip Detectors

The first auxiliary detector system housed in the scattering chamber itself is intended for the measurement of nuclear recoil particles. In its current iteration, the system utilizes the X1 chip by Micron Semiconductor[36], which has a $50 \times 50 \text{ mm}^2$ active area segmented into 16 strips. Energetic particles depositing energy create electron-hole pairs, which are split by an applied voltage. The thus created charge is detectable on both ends of the strip, allowing two-dimensional coordinate reconstruction from the charge asymmetry and strip position.

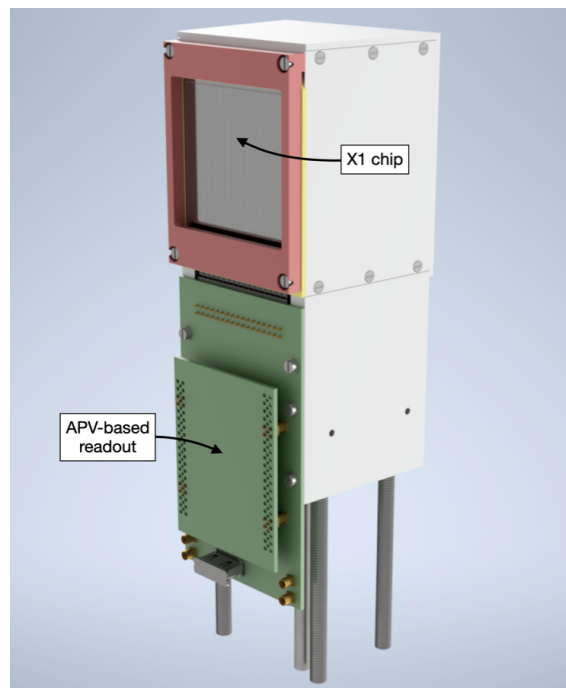


Figure 2.10: *Current design sketch of the silicon strip detector and its readout. Figure from [35].*

The silicon strip detectors will be mounted on a chandelier in the scattering chamber, 30 cm away from the interaction point. They will be supplemented by a plastic scintillator mounted directly behind the strips to serve as electron veto and for particle discrimination.

The silicon strip detector's primary purpose is the detection and energy measurement of nuclear recoil particles, which is a requirement for measurements of the electro disintegration of oxygen 16, where a low energy α -particle is produced. A design sketch for the silicon strip detector is shown in figure 2.10.

2.2.4 Beam Halo Veto

The planned beam path of MESA only intersects with molecules of the gas-jet. In reality, however, the beam will have a component that is spread out from its ideal size, the beam halo, from interactions between beam electrons and residual gas. These beam halo electrons are not confined to the interaction point and may scatter off nozzle or catcher. This presents a significant source of background for MAGIX, in absence of other sources of scattered background.

To eliminate this, the second auxiliary detector system in the scattering chamber is the beam halo veto, which consists of two scintillators, which are mounted on movable platforms to move them into or out of the beam as required. With this mobility the detectors can be placed such that any beam electrons that hit the nozzle or catcher create a signal that can be used as a background veto[37]. A sketch is shown in figure 2.11.

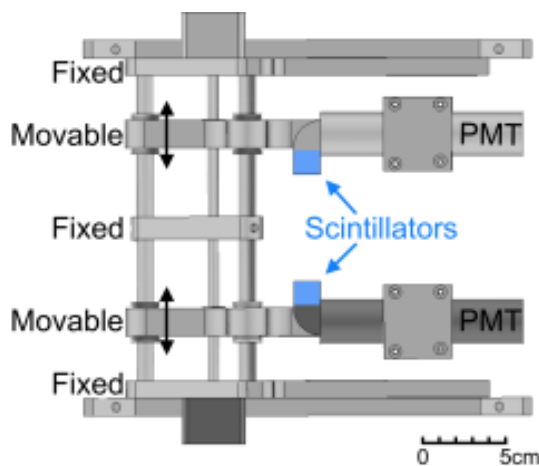


Figure 2.11: Sketch of the beam halo veto from [31].

2.2.5 Alternate Targets

To provide beam position information using a beam monitor and due to the expected complexity of the commissioning of the gas-jet target and the desire to test the other components of MAGIX independently, it is currently planned to also install a target ladder in the MAGIX scattering chamber. Included in that target ladder will be an aluminium oxide screen, a tantalum target, and a thin diamond plate. The aluminium oxide screen serves as a means to determine beam position.

The latter two are intended as commissioning and testing targets. Both will be used to generate calibration data and to confirm the particle optics derived from the measured magnetic fields. Besides this, the tantalum target will also be used for the dark photon investigations. The diamond target will be used for the first physics experiment at MAGIX, a measurement of the Hoyle State Transition Form Factor, which will be explained in much more detail in Part III.

The target ladder in which these targets are installed will be mounted such that during gas-jet operation no part provides a scattering surface that could interfere with measurement, and rotates into position as required. When the target ladder is in position and a solid target is in the beam, no ERL mode operation is possible.

This means that the beam cannot re-enter the MESA beam line and instead has to be dumped close to the experiment, for which a beam dump will be installed.

2.3 MAGIX - Spectrometers

The main instruments of MAGIX will be its high resolution magnetic spectrometers. The purpose of these spectrometers is to enable us to measure the position, angles and momentum of the scattered particles in the target frame with high precision.

To achieve this, the spectrometers use magnetic fields to bend the tracks of the particles. The magnetic fields generating that bending are designed so that momentum information in the target frame is translated, in the first order, to position information in the focal plane, while angle information is preserved. This position measurement is easier and more precise than a direct measurement of the particle momentum.

The translation between target angles and vertex resolution into focal plane angles and position is shown in figures 2.12 and 2.13.

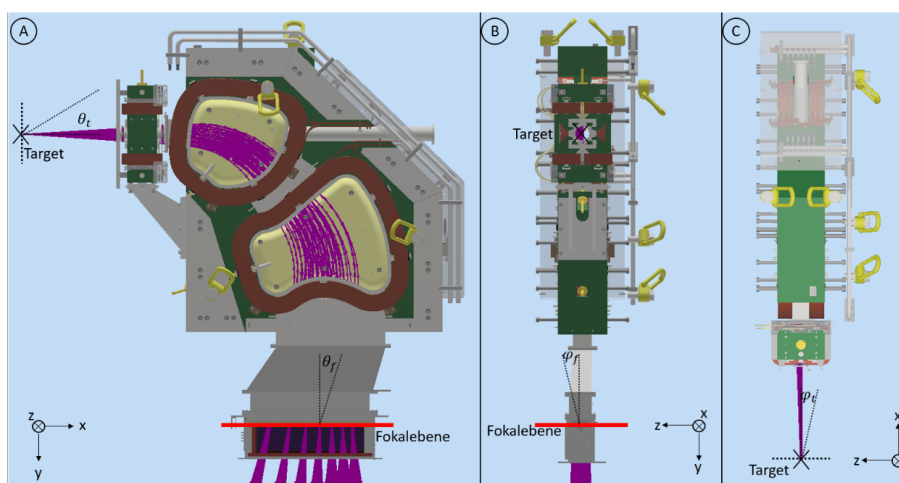


Figure 2.12: Visualisation of one spectrometer in the target coordinate system, with the z -axis corresponding to the beam direction. The spectrometer is positioned at 90° to the beam line. The spectrometer is shown from three directions in A, B, and C. The interaction point is shown with a black cross and is the origin of the target frame coordinate system. The purple lines show particle tracks. ϑ_t and φ_t are the scattering angles in the target frame, and ϑ_f and φ_f are those angles translated into the focal plane. Figure from [38].

A construction sketch of the spectrometers with all components installed is shown in figure 2.14.

The MAGIX spectrometers consist of magnets built out of coils and yokes. The design of how these coils and yokes are arranged into magnets is informed by the desired translation between target frame and focal plane. To calculate the fields that are required for this translation and to later calculate translation matrices, particles have to be tracked through a given field by solving the following first order linear differential equation:

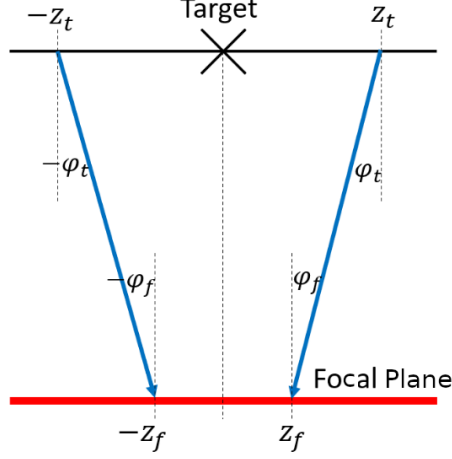


Figure 2.13: Coordinate translation between target frame and focal plane. z_t is the scattering vertex position in the target frame, z_f is the translation of that coordinate into the focal plane. Figure from [38].

$$\dot{\mathbf{k}} = \begin{pmatrix} \dot{x} \\ \dot{y} \\ \dot{z} \\ \dot{p}_x \\ \dot{p}_y \\ \dot{p}_z \end{pmatrix} = \frac{1}{m} \begin{pmatrix} p_x \\ p_y \\ p_z \\ e(B_y p_z - B_z p_y) \\ e(B_z p_x - B_x p_z) \\ e(B_x p_y - B_y p_x) \end{pmatrix} = \frac{1}{m} \begin{pmatrix} 0 & 0 & 0 & 1 & 0 & 0 \\ 0 & 0 & 0 & 0 & 1 & 0 \\ 0 & 0 & 0 & 0 & 0 & 1 \\ 0 & 0 & 0 & 0 & -eB_z & eB_y \\ 0 & 0 & 0 & eB_z & 0 & -eB_x \\ 0 & 0 & 0 & -eB_y & eB_x & 0 \end{pmatrix} \begin{pmatrix} x \\ y \\ z \\ p_x \\ p_y \\ p_z \end{pmatrix} =: \frac{\mathbf{A}}{m} \mathbf{k}, \quad (2.1)$$

with the particle vectors

$$k := \begin{pmatrix} \vec{x} \\ \gamma m_0 \dot{\vec{x}} \end{pmatrix} = \begin{pmatrix} \vec{x} \\ \vec{p} \end{pmatrix} \quad (2.2)$$

and

$$\dot{k} := \begin{pmatrix} \dot{\vec{x}} \\ \dot{\vec{p}} \end{pmatrix} = \begin{pmatrix} \frac{\vec{p}}{m} \\ e \frac{\vec{p}}{m} \times \vec{B} \end{pmatrix}. \quad (2.3)$$

In the simplest case, a single dipole magnet is enough to separate particles by their momentum. Such a simple dipole has a dispersive direction, in which the particles are split up according to their momenta, and a non-dispersive direction, in which particle trajectories are not significantly impacted by its magnetic fields. To increase resolving power by doubling the number of edges and to better align the focal plane with the horizontal, the MAGIX spectrometers will use two dipoles[39].

The acceptance of such a double dipole setup is limited by the maximum size of the magnets and their vacuum chamber, and especially by the magnetic fields and chamber size at the exit, where the particle tracks have dispersed the most. The dipole magnets' field is strongest and most uniform along the centre, but unavoidably the areas along the edges in direction of the scattered electrons include portions in which undesirable bending would take place.

The spectrometer acceptance is therefore enforced by a collimator at the very beginning of the spectrometer vacuum chamber. This collimator ensures that no particle

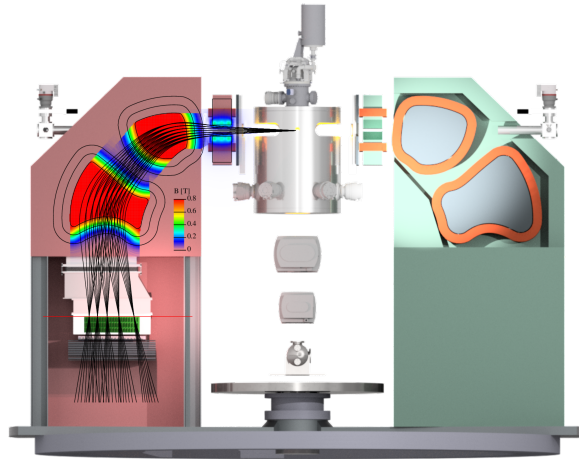


Figure 2.14: A construction sketch of the spectrometers with all detectors installed and an overlay of magnetic fields and particle tracks on PORT, on the left. The cutout of the design of PORT additionally show the two detector systems, and how the detector is positioned such that the beginning of its active area corresponds to the focal plane, shown by the focusing of the particle tracks and the red line. The cutout on STAR, on the right, shows the quadrupole-dipole-dipole configuration of the spectrometer magnets. In the middle a stand-in for the scattering chamber is shown.

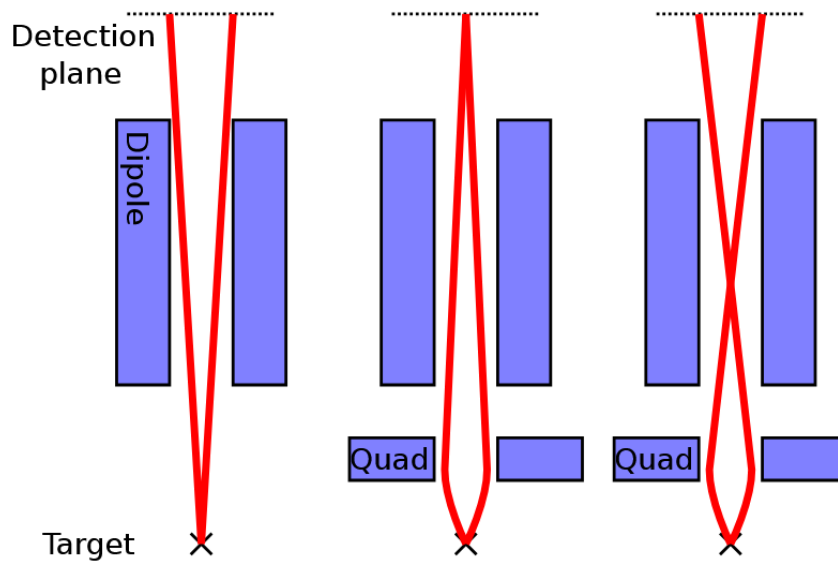


Figure 2.15: Sketch showing the effect of the quadrupole on particle tracks. Image from [39].

that would traverse those undesirable area enters the spectrometer, and thus aren't detected in the focal plane.

To achieve a higher angular acceptance and greater momentum resolution, an additional quadrupole is used. It does so by focusing the particle in the non-dispersive direction, thereby allowing a larger spread of particles to fit through the dipole exit,

and defocusing in the dispersive direction, increasing the momentum dispersion, as shown in figure 2.15.

The MAGIX design was therefore chosen to consist of a double-focusing quadrupole-dipole-dipole configuration. The magnetic fields of these magnets and an explanatory sketch are shown in figure 2.16.

The design goals for the spectrometers were a relative momentum resolution of better than 10^{-4} , an angular resolution of better than 0.05° , a central momentum range of 3-282 MeV/c, a relative momentum acceptance of 15% and a circular angular acceptance of 4.35° [39], which later had to be reduced to 2.75° , due to restrictions arising from the necessities of mechanical and vacuum chamber construction.

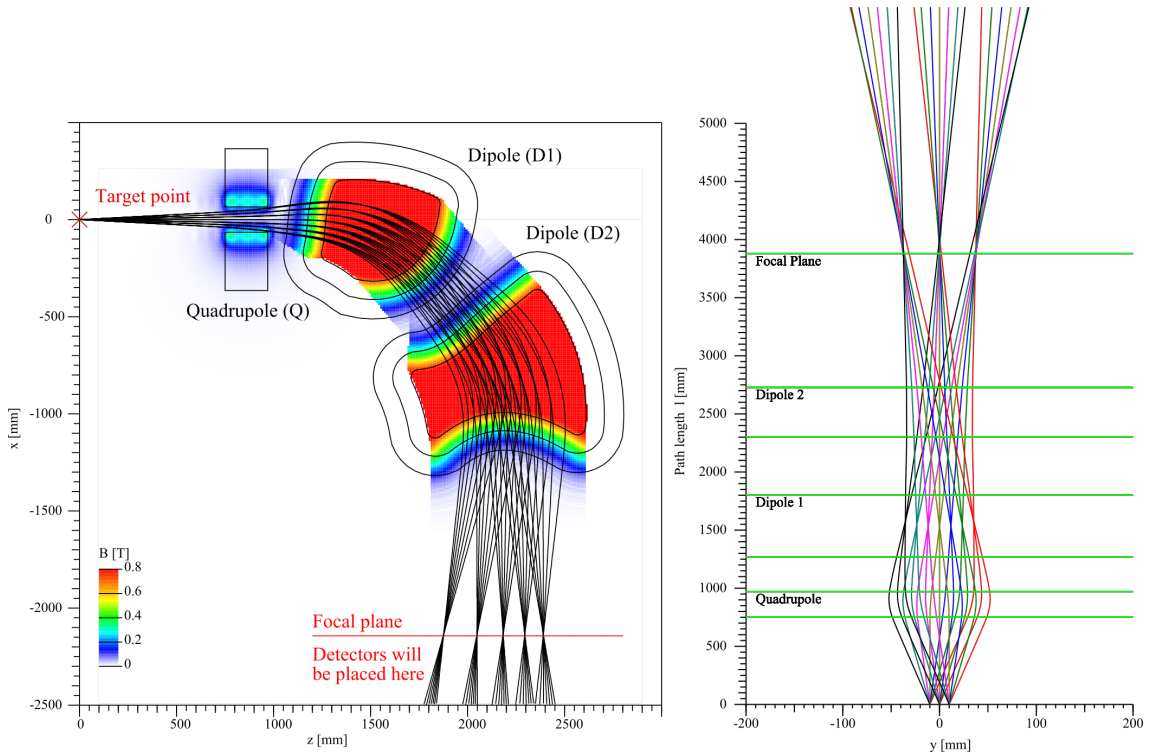


Figure 2.16: Particle tracks defining the behaviour of the magnetic fields of the MAGIX spectrometers, showing that particle position in dispersive direction corresponds to particle momentum, and in non-dispersive direction with target coordinates. Also visible is the focusing effect of the quadrupole, which enables a higher angular acceptance. Figure from [39].

To determine if a given configuration of the magnetic field fulfils these requirements, a number of particle tracks at different energies and angles are generated, sent through a simulation of the magnetic fields from the target frame into the focal frame, and a matrix representation of that translation is formed. The inverse of the matrix can be used to translate a position in the focal plane back into the target frame.

To calculate the resolution of the spectrometers, it is now necessary to choose a desired resolution of the detectors and an expected size of the beam spot, corrected for spectrometer magnification, to calculate an expected spread of a particle track in the focal plane. Given that spread and with the particle tracks and their associated translation matrices, the spectrometer resolution can then be calculated by varying all particle track representations in the focal plane by the spread expected due to

detector error and beam spot size, translating them back into the target frame and measuring their standard deviation. For more information about the design process for these spectrometers see Julian Müller's Diploma Thesis[40].

To generalize the translation between target and focal plane for all possible particle tracks instead of being restricted to only those for which the full tracking through the magnetic fields was done, an multi-variable fit was performed. This was done by utilizing the already generated tracks and their forward and backward translation matrices. Based on this fit, two algorithms were implemented, one for each direction of translation between target and focal plane frames. For more information, see Felix Höwelberend's Bachelor's Thesis[38].

To achieve the desired spectrometer resolution, the position and angles of the particle tracks in the focal plane have to be measured with the position resolution of $100\ \mu\text{m}$ and the angular resolution of $3.5\ \text{mrad}$ that were assumed in the spectrometer design process.

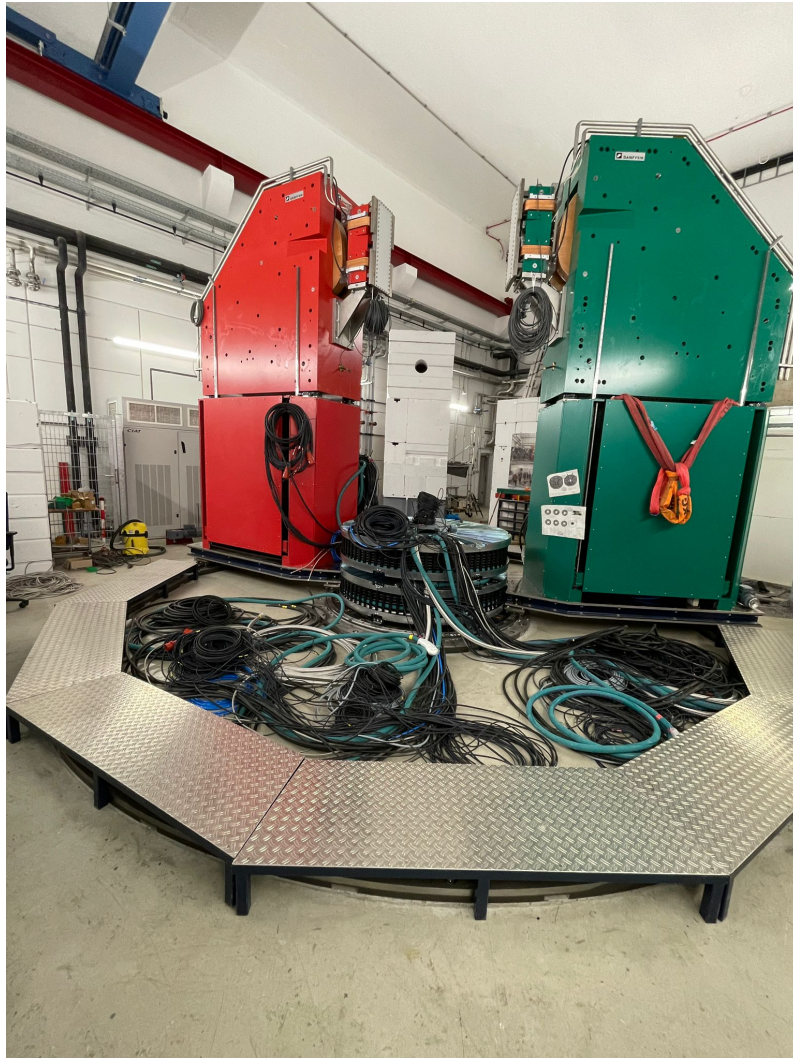


Figure 2.17: *MAGIX Spectrometer after installation of the energy chain system on the 6.2.2026. In the foreground, the myriad of cables and pipes that will be used to connect the spectrometers are still visible.*

The two spectrometers are not constructed identically, and are instead mirror symmetric with the vertical plane along the beam. The spectrometers are each mounted

on their own steel platform, which run on two ring rails, on opposite sides of the beam line. Each platform can be positioned between 15° and 165° off the forward beam direction. The rails and platform are calibrated so that these rotations share a vertical axis, which runs through the interaction point. To provide the spectrometer magnets and detector systems with power, cooling, and data connection, an energy chain system is installed. This system runs inside the inner perimeter and carries power, water and data lines to the rotating spectrometers.

The spectrometer magnets, manufactured by Danfysik, sit on shielding houses, which contain detectors and electronic equipment. For their protection and to reduce beam-induced background they will be surrounded by 100 mm thick lead bricks, for electromagnetic shielding, and 70 mm thick borated polyethylene plates, for neutron shielding.

A picture of the in construction spectrometers is shown in figure 2.17.

2.4 MAGIX - Time Projection Chamber

Mounted directly onto the vacuum chamber of the spectrometers is the focal plane tracking detector system for MAGIX, our TPC. With an extension of the vacuum chamber to bridge the gap between the end of the spectrometer and the focal plane, it is positioned so that scattered electrons leave the shared beam and spectrometer vacuum, pass through a $75\ \mu\text{m}$ thick polyimide foil, and enter the TPC. Additionally, the position of the TPC, and thus the entry of the particles into the active area, is optimised so that it coincides with the focal plane of the spectrometer optics.

The TPC uses ionisation in a counting gas to detect the particle tracks. In the setup employed by MAGIX, an electric field is used to separate the ions and electrons, and drift them to anode and cathode. The anode is equipped with **G**aseous **E**lectron **M**ultiplier(GEM) foils to increase the deposited electron charge that gets detected by a segmented pad layout. Combined with the timing of the charge deposition, it is possible to reconstruct all three dimensions of a particle track, if precise information about the time when the particle entered the detector is provided.

The theory, design and construction of this detector will be discussed in much greater detail in Part 3 of this thesis.

2.5 MAGIX - Trigger Veto System

By choosing a time projection chamber as focal plane detector it became necessary to add another detector to provide precise timing information. Additionally, the arrangement of the spectrometers means that cosmic muons cannot be distinguished from scattered electrons by information about the particle's track alone, which also necessitates some manner of muon veto. Additional sources of radioactive background, such as beam induced neutrons, strengthen that necessity. MAGIX has chosen to answer these two requirements with two closely related detectors, which are thus combined into a trigger veto system.

The trigger layer is mounted directly below the TPC and provides trigger and timing information for that detector. This trigger layer consists of 22 fast-rise plastic scintillators, which are read out on both sides by photo multiplier tubes to provide both timing and rough position information. The scintillator bars are wrapped first in a

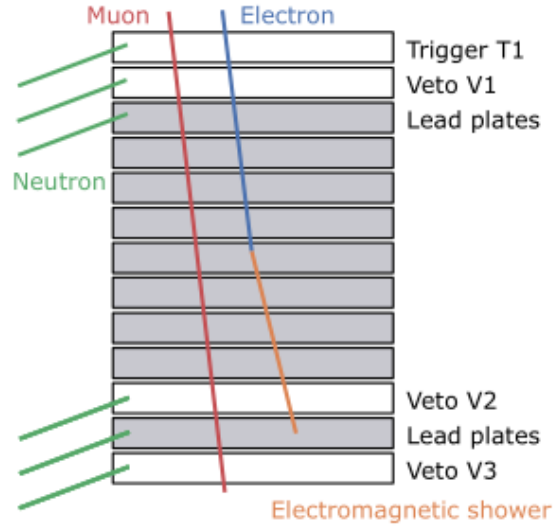


Figure 2.18: *Design scheme behind the MAGIX trigger veto system. Different particles create different response patterns, allowing particle identification. Figure from [35].*

white polytetrafluorethylene foil for internal reflection and then in a light isolating black polyethylene foil.

The trigger layer is followed by the veto system. This veto system consists of eighteen layers, stored in nine drawers. Of the eighteen layers, fifteen are passive lead plates and three active scintillator layers. The scintillator layers of the veto system have a larger segmentation of just 3 bars each. These scintillators are read out with silicon photomultipliers, and serve to identify particle penetration depth and thus provide particle identification[35].

With the background of the physics program and experimental setup explained, the following part will deal with the theory, design and construction of the MAGIX focal plane tracking detector.

Part II

Constructing a Time Projection Chamber for Measuring Particle Tracks in the MAGIX Focal Plane

Chapter 3

Theory of Gaseous Detectors in General and Time Projection Chambers in Specific

As previously mentioned in section 2.4, the focal plane detector of MAGIX is a **Time Projection Chamber**(TPC), which functions by detecting the ionisation products of high energy particles passing through the gas in its active volume. As background for the design and construction that will be described in the following chapter, this chapter will first deal with gaseous detectors and their operating principles in general. The second section details the function of a TPC and its components as we use them, the counting gas, amplifier stage, field cage and signal processing electronics.

In the third section a short interlude into solid state physics is required as background for the calibration system of the TPC, specifically UV-LEDs and the transmissive photo effect.

3.1 Gaseous Detectors

All gaseous detectors function according to the same principle: the particle to be observed passes through a gas, where it triggers ionisation. Based on the amount, position and timing of the ionisation products, information about the ionising particle can be collected. The following section details how these ionisations occur, how charges travel in the gas, what conditions are necessary for the information to be collected, and how the information is processed. The explanation is based on the book Particle Detectors by Herman Kolanoski and Norbert Wermes[41].

3.1.1 Ionisation in Gas

When a charged, highly energetic particle passes through matter, it collides with the electrons in that matter. It also collides with the nuclei, of course, but for our purposes those interaction are rare enough to be disregarded. In each of the electron collisions, the colliding particle loses a random fraction of its kinetic energy to the electron it collides with. The maximum energy transfer in this process is:

$$E_{Kin}^{Max} = \frac{2m_e p^2}{m_0^2 + m_e^2 + 2m_e E/c}, \quad (3.1)$$

where m_e is the mass of an electron and m_0 the mass, p the momentum, and E the energy of the colliding particle. When the energy transferred to the electron is greater than its ionisation energy E_I , the electron is completely separated from the nucleus and the atom becomes ionised. Some of the ionised electrons have sufficient energy to themselves cause additional ionisations, so called δ -electrons, and recombinations of high energy electrons with recently produced ions leads to high energy photons also being produced. These high energy photons, called streamers, can smear out the signal left by the primary ionisations when they create more ionisations some distance off the track if the medium is optically transparent to their passage.

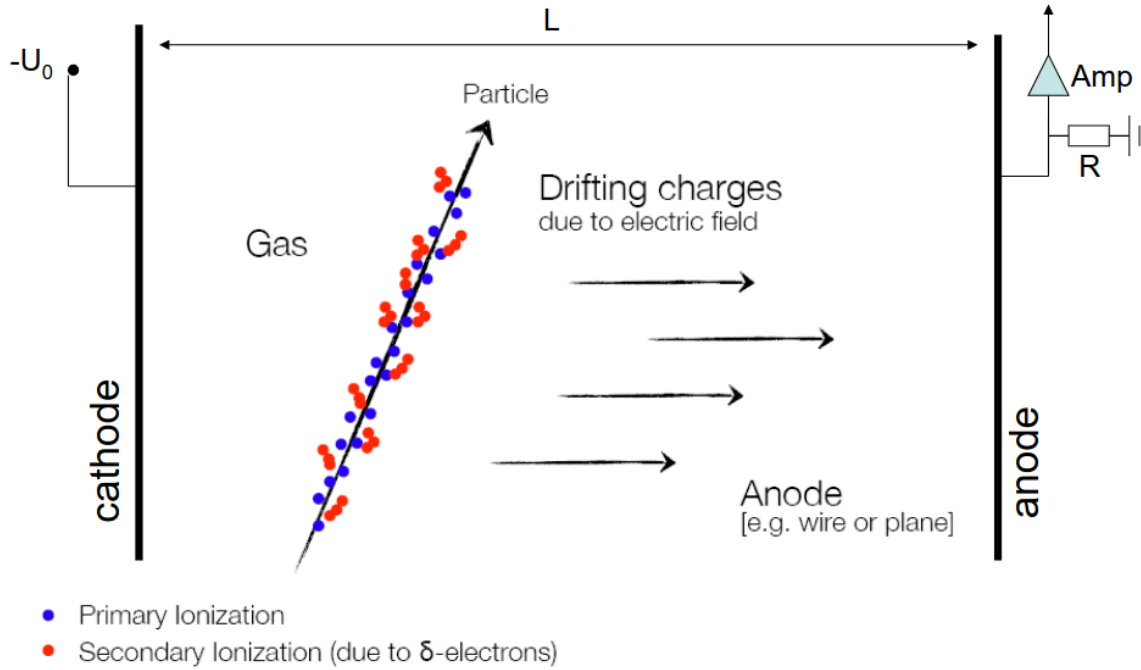


Figure 3.1: Principle of operation of gaseous detectors. Figure from [42].

The average energy per created electron-ion pair W depends on the material and the energy and type of incident particle, and is proportional to E_I .

The total number of ionisations n_T is therefore proportional to the ratio between the energy loss ΔE and W :

$$n_T = \frac{\Delta E}{W}. \quad (3.2)$$

In the case of electrons, the most significant energetic particle at MAGIX, the energy loss of the particle dE per distance travelled dx is given by the Bethe-Bloch formula:

$$-\frac{dE}{dx} = \frac{4\pi n}{m_e c^2 \beta^2} \cdot \left(\frac{e^2}{4\pi\epsilon_0}\right)^2 \cdot \left[\ln\left(\frac{2m_e c^2 \beta^2}{I \cdot (1 - \beta^2)}\right) - \beta^2 \right], \quad (3.3)$$

with $\beta = \frac{v}{c}$ the speed relative to the speed of light, n the electron density of the material and I a medium excitation energy specific to the material. The formula

predicts a rapid decrease in energy loss with increasing electron energy, reaching a minimum at approximately 1 MeV, followed by a logarithmic increase.

In the absence of an electric field, the particles produced recombine and no drifting charges are created, making detection difficult. By applying an electric field to the ionised material, the ionisation products can be separated and more easily measured, as long as electrons and ions can travel through the material, which is the case in most gases. This general case of a gaseous radiation detector can be seen in figure 3.1.

The electrons and ions are not only separated by the electric field, they continue to be accelerated by it. While drifting through the gas, they will, like the initiating particle, collide with the electrons of the gas atoms. Due to these collisions, the electrons and ions diffuse away from each other and spread throughout the gas. In the two following subsections we deal with a mathematical description of first the drift and the diffusion.

3.1.2 Drift

The motion of ionised particles along the direction of the electric field consists of a series of accelerations and decelerations—the former due to the field, the latter due to collisions with electrons of the gas. The overall motion is chaotic, but an average drift velocity, denoted as \vec{v}_d , can be determined as the mean of all movements.

\vec{v}_d can be calculated using the Boltzmann Transport equation, which describes the absolute temporal derivative of the distribution density $f(\vec{x}, \vec{v}, t)$ as an integral of collisions. f contains the information about the velocity \vec{v} and location \vec{x} of the drifting, charged particle at time t . With these, the transport equation can be expressed as:

$$\left(\frac{\partial}{\partial t} + \vec{v} \cdot \nabla_{\vec{x}} + \frac{\vec{F}}{m} \cdot \nabla_{\vec{v}} \right) f(\vec{x}, \vec{v}, t) = \frac{\partial f}{\partial t} \Big|_{\text{coll}}. \quad (3.4)$$

The first term on the left side, the partial derivative with respect to time, is equal to 0 in a closed system. The second term describes diffusion, which can and will be treated differently for our purposes and as such will be detailed in section 3.1.3. The third term describes external forces and for our case of a purely electrical field is equal to $\frac{q}{m} \vec{E} \cdot \nabla_{\vec{v}}$.

The collision integral $\frac{\partial f}{\partial t} \Big|_{\text{coll}}$ on the right contains all information about what happens during the collisions of all particles, and as such can become arbitrarily complex. Under the assumption that a closed system will return to its equilibrium state f_0 after a relaxation time τ following an excitation, the collision integral can be rewritten as $\frac{f-f_0}{\tau}$. The relaxation time corresponds to the mean time between collisions and as such can be defined using λ , the mean free path, as $\tau = \frac{\langle v \rangle}{\lambda}$. The medium free path for these collisions is inversely proportional to the number of gas particles per volume N_m and the energy dependent cross section of the collisions $\sigma(\epsilon)$: $\lambda = \frac{1}{N_m \sigma(\epsilon)}$. With that the transport equation can be simplified to:

$$\frac{q}{m} \vec{E} \cdot \nabla_{\vec{v}} = \frac{f - f_0}{\lambda}. \quad (3.5)$$

With this solution of the distribution density the drift velocity can be calculated as the mean of the velocity vector[41], which reduces it to:

$$\int \vec{v} f(\vec{v}) d^3\vec{v} = \vec{v}_D = \frac{q}{m} \vec{E} \left(\frac{2}{3} \left\langle \frac{\lambda}{v} \right\rangle + \frac{1}{3} \left\langle \frac{\delta\lambda}{\delta v} \right\rangle \right) = \mu \vec{E}. \quad (3.6)$$

In this simplification the mobility μ contains all information about the drifting particle and the medium, while being independent on the electric field, and can be easily measured and predicted. Due to its inverse dependence on the mass, electrons in general have a drift velocity three order of magnitude higher than ions, which makes them the better choice for multiplication and fast readout.

However, while the assumption that underlies this simplified collision integral holds true for ions up to very high field strength, electrons are light enough that they gain enough energy between collisions to invalidate the assumption that they return to the equilibrium state, even at low field strengths. There is no derivation of the drift velocity of electrons in this case, and it is instead extracted from numerical simulations.

One further complication for drifting electrons is that with each collision with a gas atom, there is a risk that instead of continuing their path, the electron recombines. This effect depends on both the energy of the colliding electron, and so the electric field, and the shell configuration of the gas atom. The probability of attachment is negligible for noble gases, but for gases with high electronegativity like oxygen, the mean lifetime of a thermal electron is 200 ns[43]. Even small inclusions of such a high electronegativity contaminant can therefore ruin a measurement.

3.1.3 Diffusion

Free electrons and ions will distribute in a gas following the concentration gradient of the charge density. How and how fast they do this is described by the particle flow \vec{j} of the particle density ρ .

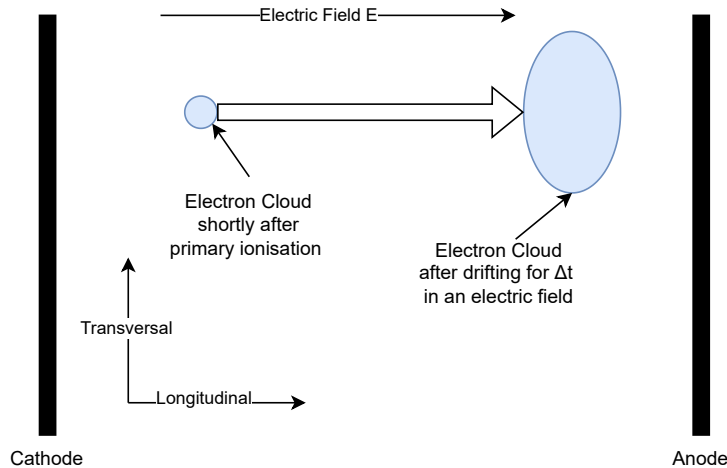


Figure 3.2: Schematic picture of an electron cloud produced by a primary ionisation event drifting through the electric field of a detector.

\vec{j} can be determined as a solution to Fick's law, in our case modified with an additional term due to the drift in one direction as:

$$\vec{j} = \frac{\partial \varrho(\vec{x}, t)}{\partial t} = D \vec{\nabla}^2 \varrho(\vec{x}, t) - \varrho(\vec{x}, t) \vec{\nabla} \cdot v_D, \quad (3.7)$$

with the diffusion constant D . This diffusion constant is then separated into two cases: movements in direction of drift, called the longitudinal diffusion constant D_L , and orthogonal to the direction of drift, called the transverse diffusion constant D_T . With that separation, a generalized solution for the flow \vec{j} is given by:

$$\varrho(\vec{x}, t) = \frac{1}{(4\pi D_T t) \cdot (4\pi D_L t)^{\frac{1}{2}}} \cdot \exp\left(-\frac{x^2 + y^2}{4D_T \cdot t} - \frac{(z - |v_d|t)^2}{4D_L \cdot t}\right). \quad (3.8)$$

The diffusion coefficients for the different directions can be extracted from the distribution density of the gas molecules. However, just like with the drift velocity of electrons at high fields, this cannot be done analytically, and is most often determined experimentally or in simulation.

From equation 3.8, the standard deviation of the particle distribution can be extracted as:

$$\sigma_{T/L} = \sqrt{2D_{T/L} \cdot t}. \quad (3.9)$$

An electron cloud drifting through an electric field is shown in figure 3.2.

3.1.4 Charge Multiplication

In addition to drift velocity, the strength of the electric field in gas detectors has a second important effect: charge multiplication. When ionised particles are sufficiently accelerated, they can ionise gas molecules upon collision. Figure 3.3 shows the relationship between voltage and the number of electron-ion pairs. At very low field strengths, the field is not strong enough to separate all created charges before they recombine, corresponding to region A, which is not used for any detectors. When the electric field is strong enough to completely prevent recombination, the detector is operated in the saturation regime, corresponding to region B. Here, the number of detected electrons matches the number of primary ionisations and is proportional to the energy loss of the ionising particles.

Once the field is strong enough that the drifting particles are sufficiently energetic to lead to ionisations on collision, the number of ionising particles increases geometrically. This process is called a Townsend discharge. The multiplication is described by:

$$N(x) = N_0 \cdot e^{\alpha x}, \quad (3.10)$$

where $N(x)$ is the number of particle at x from start of the field, depending on the starting number N_0 and the first Townsend coefficient α , which depends on medium and applied field. For a finite field, the number of new particles remains proportional to the number of starting particles, corresponding to region C, thus called the proportional region.

At some point this proportionality is no longer given, as the number of ionisations is limited by the available gas particles. This corresponds to region D and is not typically used in particle detectors.

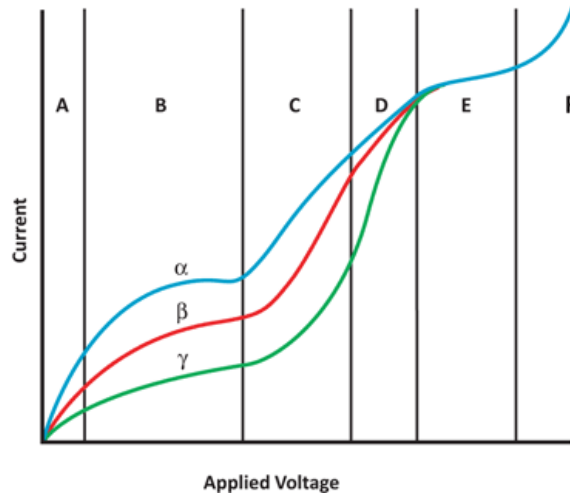


Figure 3.3: Plot showing detector response in dependence on electric field strength for three different radiation types. Figure from [44].

When the voltage is high enough, each incoming particle causes a full ionisation of the counting gas. This corresponds to region E, called the Geiger region for its use in the original particle detector, the Geiger counter. Eventually, the field is strong enough so that a discharge occurs even without ionising particles, meaning no further information about possible particles can be obtained from the discharges, corresponding to region F. Additionally, it is likely that constant discharge of voltage across the gas causes damage to the detector’s surfaces.

3.2 TPC

A TPC consists of an active ionisation region, a multiplication region, and a readout system. An exemplary structure and its functional principle are illustrated in figure 3.4.

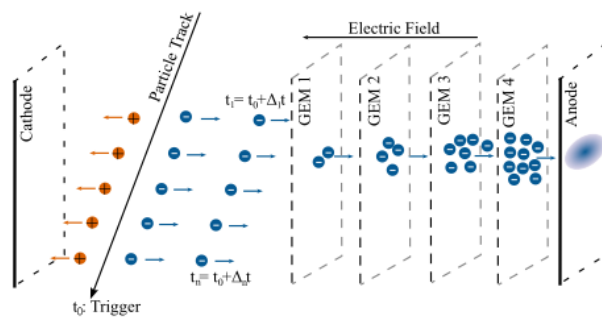


Figure 3.4: General function of a TPC with GEMs in their multiplication region. Figure from [45].

The special property of a TPC is its capacity to perform a three-dimensional reconstruction of a particle’s track by using not only the two-dimensional signal given by the projection of the ionisation product onto the readout structure but also its timing. When combined with information about the entry time of the primary particle into the drift volume, such as from a trigger detector, and a known drift velocity,

the third dimension of the track can be determined. Since multiple position measurements are taken along the TPC, the reconstruction is both robust and precise. Additionally, by summing the measured charges, the TPC allows conclusions to be drawn about a particle's energy loss and thus its energy.

In this arrangement, the readout of the generated signal occurs outside the expected path of the particle, meaning the particle does not need to pass through the material of the readout system. As a result, the particle's trajectory is only minimally affected by interaction with the detector. When using electrons as signal, the readout and multiplication happen on and above the anode, with the cathode bordering the other side of the active region.

A TPC as such consists of the active region, filled with a gas mixture, which has a charge multiplying system in front of its anode, and is surrounded by a field cage to generate a homogenous drift field. Its anode is equipped with signal processing electronics.

3.2.1 Gas Mixture

The choice of the gaseous medium defines most properties of a gas detector. In general, no gas by itself fulfils all the requirements. Experience from previous applications has shown that a combination of two or more gases, each playing different roles, can significantly improve detector performance. These two roles are those of the counting gas and the quenching gas. The counting gas is the main component of the gas mixture and defines the bulk of its behaviour, while the quenching gas and further possible additives are used to compensate for deficiencies of the counting gas.

The counting gas needs to provide both a high primary ionisation density and a high charge amplification, but without transitioning too quickly into discharges. This requires a start of amplification at low electric field strengths. Specifically for our TPC, the heavy noble gases of krypton and xenon would be suitable in this regard, but will not be used because their high radiation lengths would run counter to our desire to reduce multiple scattering as much as possible. Helium and neon, on the other hand, have insufficient ionisation densities. Argon is suitable, but suffers from instabilities in its amplification behaviour.

Of equal importance to its ionisation properties are the transport properties of the gas, its ion and electron mobility and diffusion constants, as well as its attachment rate. Here the halogens and oxygen disqualify themselves from use in our TPC because of their high attachment rates, as mentioned above.

An unavoidable aspect of gases with high ionisation densities is that they are easily ionised, which indicates a low propensity towards energy dissipation in other ways. This in turn implicates a low probability for these gases to absorb or attenuate photons. Indeed, the gases with the lowest ionisation threshold are the mono-atomic, ie noble, gases, since they don't have any energy dissipation pathways before ionisation. This is a concern for gaseous detectors because this means that good counting gases cannot be good at suppressing streamers. The addition of at least a quenching gas for this purpose is therefore evident.

The quenching gas is mainly responsible for lowering the absorption threshold of photons with energies above the ionisation threshold of any material inside the active volume, to prevent streamers from causing correlated secondary ionisation

events following the primary. This absorption has to happen without causing an ionisation, corresponding to a high ionisation threshold, which is provided by organic gases, which have a multitude of rotational and vibrational states to accept and dissipate energy. Correspondingly, they make ideal quenching gases.

In addition to all these conditions for ideal detectors, they must also meet the demands of experimental reality, enabling safe operation at low cost and causing no damage through potential chemical processes, and ideally also low environmental impact.

Of the remaining candidates for a counting gas, neon is precluded due to its high cost, owing to its relative scarcity in air compared and high industrial demand. Argon, like neon, is produced as a by product from liquid air distillation and with its abundance remains affordable.

For the quenching gas, a number of complex and high performing additives have been discovered. Unfortunately, most of them have significant global warming impacts, either in production or by themselves when released into the atmosphere, due to containing fluor. Most alternatives suffer from high cost or chemical instability[46]. However, a low cost, comparatively low environmental impact alternative with sufficient chemical inertness exists, in the form of carbon dioxide[47].

A mixture of argon and carbon dioxide has been tested and found to satisfy all our requirements, at a volumetric mixing ratio of 90 to 10. The drift speed and transversal and longitudinal diffusion constants of this gas mixture as a function of applied electric field are shown in figure 3.5.

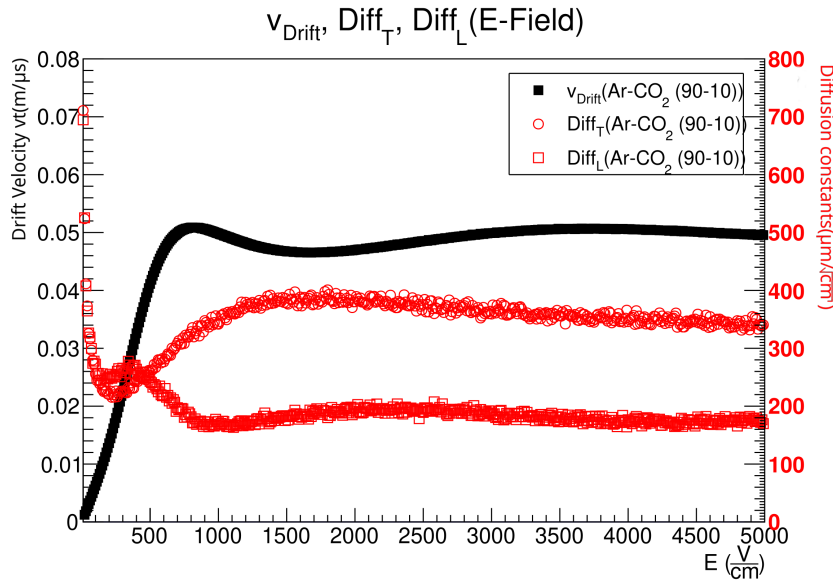


Figure 3.5: *Electron drift properties of the MAGIX argon CO2 90:10 gas mixture. The two green dotted lines show the intended range of the electric field to be applied across the drift region, between which drift velocity is approximately linear. Figure from [35].*

Besides these primary, desired, components, a gas system will also include impurities. These impurities are brought into the system both from the gas bottle, as no commercially available source of gas is entirely pure, and from infiltration into the system from the surrounding atmosphere, as no gas system is entirely airtight. The most worrisome impurity for our gas detector is oxygen, as it has a high electron

attachment rate. Over long drift distances, high oxygen impurities can cause a cloud of drifting electrons to thin out enough to drop below detection threshold. As such, high purity, 99.9999%, gases are employed, and all source of atmosphere infiltration have to be minimised.

3.2.2 GEM

For the MAGIX TPC we will use **Gas Electron Multiplier**(GEM) foils. Such foils consist of a non-conductive material coated on both sides with a conductive material. The foil contains holes with a regular hexagonal pattern. When a voltage is applied between the two conductive layers, an electric field is created, whose field line shape is shown in figure 3.6, with very large field strength in the hole region.

A voltage is also applied between the surface of the GEM foil and the cathode of a gas detector. The electric field above and below the foil, in the drift and induction regions, operates in the saturation range of charge multiplication. The electric field lines which the electrons follow are desired to be as straight as possible in the drift region, to allow precise location reconstruction. Directly above and below the foils, the field lines bunch together as they are funnelled into the comparatively conductive holes in the isolating foil. In this collection region, the electrons, still following the field lines, are concentrated in the holes. Inside those holes, in the amplification region, the field lines are concentrated and thereby sufficient to trigger electron avalanches, multiplying the measurable charge by a factor on the order of 10^2 and 10^4 .

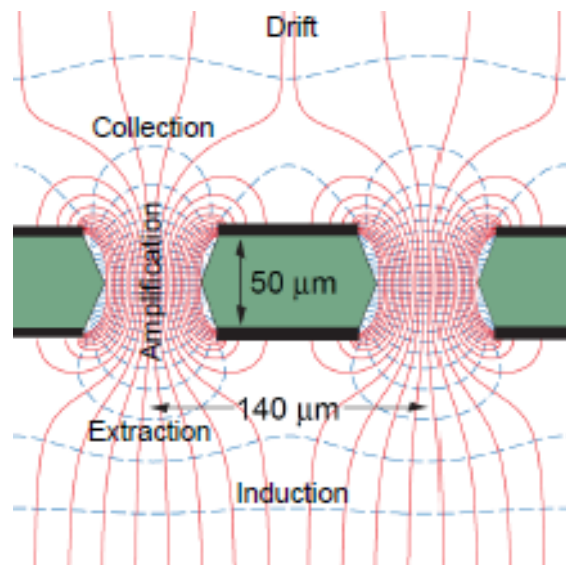


Figure 3.6: Schematic drawing of a GEM foil. The red lines are electric field lines, the blue lines show equipotential. Figure from [48].

At the same time, however, undesired ions are also created. Due to the difference in mass, most of the electrons leave the vicinity of the hole, while the opposite happens for the ions: most of them recombine with electrons from the foil on the top surface. Until this recombination occurs, the hole has a dead time during which new primary electrons cannot trigger avalanches. The remaining free ions, known as ion backflow, carry a field charge that distorts the electric field on their way back to the cathode.

The multiplication and ion backflow properties of a GEM foil depend on the thicknesses of the conducting and non-conducting layers and on the geometry and distribution of the holes, as well as the configuration of its electrical field.

The biggest restrictions on the operation of a GEM foil are the ion backflow and the limit on the maximum voltage difference that can be applied across a single foil. While higher voltages correspond to higher multiplication, a too strong field reaches the breakdown region, and constant discharges, sparks, can melt the conducting layers together, ruining the foil. To prevent both of these, multiple foils are operated on top of each other, with a lower voltage applied to each[48].

3.2.3 Field Cage

Since a TPC obtains information about one dimension of a particle's position through the arrival time of the charge at the readout elements, the measurement of this coordinate is sensitive to the homogeneity of the drift velocity within the active region of the TPC. Because the drift velocity is directly proportional to the electric field, a classic capacitor setup is unsuitable for the electric field, as the field lines distort at the edges, as can be seen in figure 3.7 (a). This makes a field cage a necessity for a TPC. This cage consists of conductive elements that surround the active region at multiple heights and maintain height-proportional gradations of the total voltage between the cathode and anode, see figure 3.7 (b). This straightens the field at the edges.

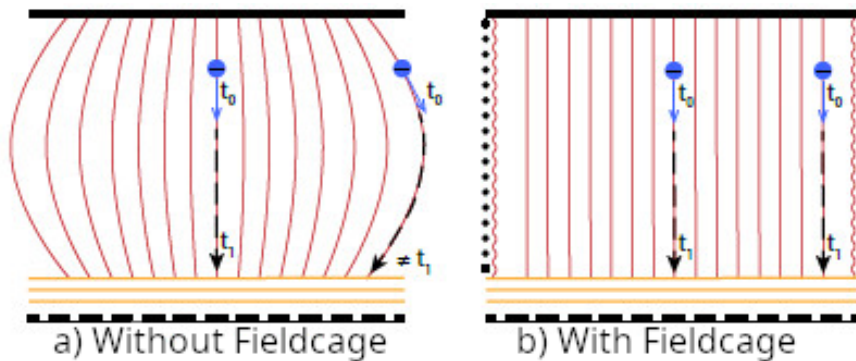


Figure 3.7: *Principle of operation of a field cage. Figure from [49].*

3.2.4 Signal Processing

The readout of the signal can be done in various ways. The moving charges induce a current in conductive surfaces by changing the electrostatic field lines. The current begins as soon as the electron avalanches have passed through the last GEM foil and ends once the charges have fully reached the surface. The sum of the induced charge is equal to the sum of the inducing charges. The instantaneous induced current of a charge q with drift velocity v_{Drift} is given by the Shockley–Ramo law:

$$i = E_v \cdot q \cdot v_{Drift}. \quad (3.11)$$

In this context, E_v is the electric sample field, which depends on the geometry of the readout surface.

There are various ways to segment the anode, where the electrons to be measured induce their current. The segmentation consists of conductive surfaces that are separated from each other, so each surface has its own channel for readout. The geometry of the anode is defined by whether one uses strips or pads, and what the dimensions of the strips or pads should be. The difference between strips and pads is illustrated in figure 3.8.

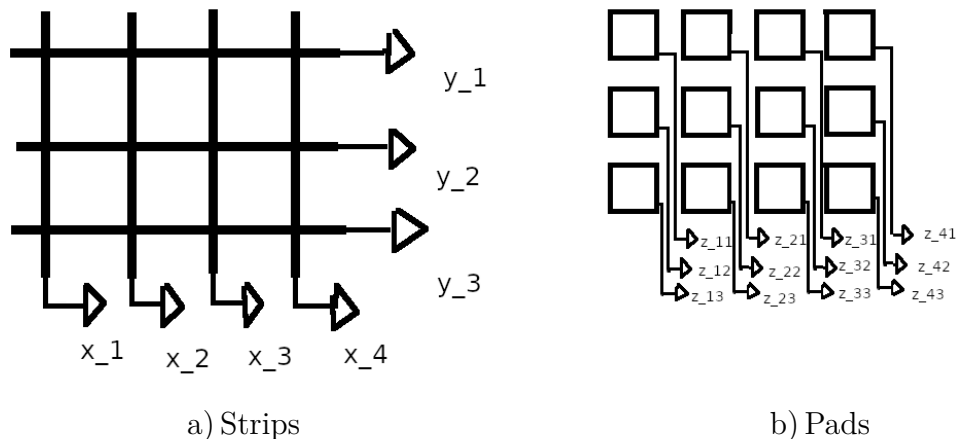


Figure 3.8: Channels of strips and pads. Their number rises linearly with the dimensions of the chamber for strips, quadratically for pads.

Using strips, fewer channels are required for the same resolution, which means less electronics and thus lower costs. However, simultaneously arriving signals generate complementary ghost hits. The effort required to exclude such ghost hits more than offsets the reduced number of necessary channels in most TPCs so pads are generally preferred.

The choice of pad dimensions is based on two factors. First, the spatial resolution of the readout elements is better the smaller the dimensions of the strips or pads. Second, the electrical charge arriving on the elements, even with charge multiplication, is on the order of only 10 fC. If the area is too small, it may not receive enough charge to produce a signal distinguishable from electronic noise. This trade-off also considers that a single avalanche can affect multiple neighbouring elements.

The number of elements per row responding to an avalanche is called multiplicity. A multiplicity greater than one allows the position of the primary ionisation to be determined by a weighted average based on the charge per element. In this case, the resolution is limited more by the diffusion of the avalanche than by the size of the readout elements, which can be quantified by the width of the charge distribution.

The induced current of the pads that flows from the channels of the anode has to be brought into a suitable form to be analysed. For this the analogue charge signal is generally first amplified, then turned into a more easily measurable voltage and finally digitized. This is achieved using an integrating amplifier, which takes the charge Q arriving over a defined period and simultaneously amplifies it and converts it into a voltage U_A , depending on its capacity C_A :

$$U_A = -\frac{Q}{C_A}. \quad (3.12)$$

This integrated signal is brought into an approximate Gaussian shape, whose amplitude corresponds to the original charge, and thereby, through the chain of amplification in electronic and gas, to the original number of ionised particles that reached the anode. The height and timing of this Gaussian can now be measured to determine charge and signal time. This chain of signal processing is shown in figure 3.9[50].

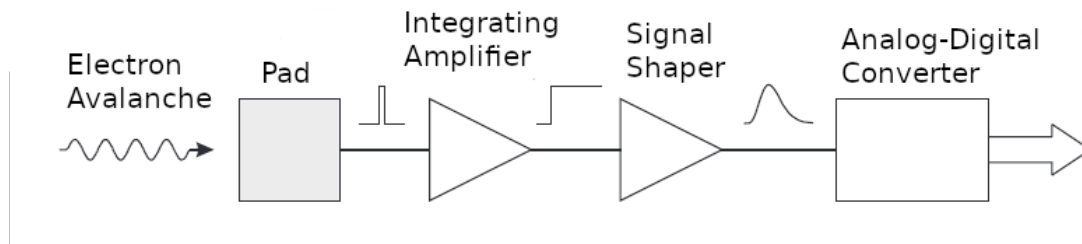


Figure 3.9: *Symbolic representation of the chain of transformation of the signal. Figure from [50].*

3.3 A short Interlude into Solid State Physics

The MAGIX calibration system is required to determine the actual drift conditions within the active area of our detector. Without a precise knowledge of on what paths and with what velocity the ionised electrons drift, we cannot reconstruct the particle track that created them. As explained in the beginning of this chapter, the drift conditions are influenced by both the gas and the electric field. Both of these conditions can have local and temporal variance that would not be apparent without a known signal to calibrate against. For this known signal, we require a timed release of electrons at a known position. To achieve this, an electron recombines with a electron hole in a semiconductor to create a high energy photon, in an **Ultra Violet(UV) Light Emitting Diode(LED)**. This UV photon kicks an electron out of the conduction band of a thin film of aluminium, which leaves out of the surface of the film, by the photoelectric effect. These two elements will be explained in the following two sections.

3.3.1 UV LEDs

A simple LED consists of pn-junction in a semiconductor that has been tuned such that the energy of an electron-hole-recombination is released in the form of a photon, a light emitting diode. The pn-junction of the simplest possible LED consists of a semiconductor material that has been doped such that an excess of holes is present on one side and an excess of electrons on the other side. Hole excess, p-doping, is achieved by adding in atoms with three valence electrons, electron excess, n-doping, by adding atoms with five electrons. At the plane where the dopants switch, an applied voltage drives electrons and holes together, and recombination of the two creates photons, the energy of which depends on the band gap energy, as can be seen in figure 3.10[52].

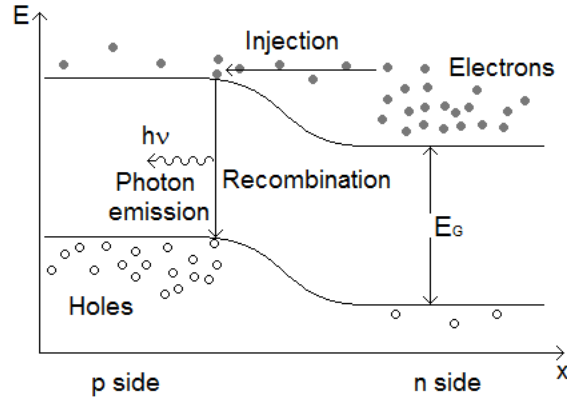


Figure 3.10: Sketch of the principal of operation of an LED. Image from [51].

To enable this, the geometry of the energy bands of the pn-junction requires that a direct emission of photons is kinematically possible, without requiring intermediate states or involvement of phonons for momentum conservation, which would mean other energy dissipation pathways, like Shockley-Read-Hall-recombinations, are favoured. For these reasons most diodes are based on an alloy of gallium, like gallium arsenide, and not the more common semiconductor material silicon, as can be seen in figure 3.11.

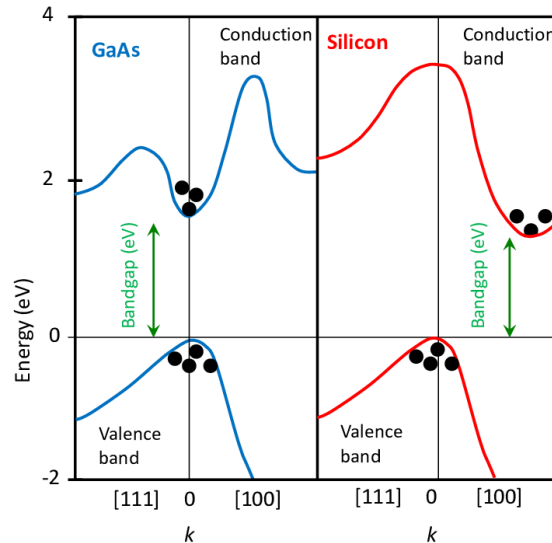


Figure 3.11: Difference of energy band structure between gallium arsenide and silicon, with its conduction band and valence band plotted in dependence of the crystal momentum k . In the gallium arsenide, the valley of the conduction band and the peak of the valence band align, unlike in silicon, so that a transition is directly possible. Figure from [53].

To tune the wavelength the band gap energy has to be modified, which is done by changing the substrate material, adding in different dopants, and changing the geometry of the pn-junction. Lower energies are easier to achieve, meaning that near infrared LEDs based on gallium arsenide became available first[54].

Following the development of a blue LED based on gallium nitride by Shuji Nakamura[55], more complex architectures have enabled the production of LEDs with

wavelength down to 255 nm.

3.3.2 Photoelectric Effect

The photoelectric effect as originally described by Einstein[56] is the emission of an electron from the surface of a material induced by an impinging photon that carries sufficient energy to overcome the work function W of the material. The maximum kinetic energy of the electron is then

$$E_{kin} = \frac{hc}{\lambda} - W, \quad (3.13)$$

with the photon wavelength λ . In the century since, this process has been analysed further, and new descriptions are now available, one of which is the three step process. With this, the photon striking the surface of a material is not immediately followed by an electron leaving it. Instead, the photon first penetrates some depth into the material, depending on the absorption coefficient α of the material. The penetration depth δ_p for a given material and photon wave length is given by[57]:

$$\delta_p = \frac{1}{\alpha} = \frac{\lambda}{4\pi k(\lambda)}, \quad (3.14)$$

with $k(\lambda)$ the imaginary part of the index of reflection of the material for that wavelength. After δ_p , the number of photons has been reduced by a factor of e . The energy of the lost photons has been transferred to the electrons of the material, some of which have received more than the binding energy E_b , and are now free electrons with a kinetic energy no larger than $\frac{hc}{\lambda} - E_b$. Some of these free electrons will reach the surface of the material without colliding at all with still bound electrons of the material, or only losing some of their energy in those collisions. If the energy they have when reaching the surface is greater than the energy needed to escape that surface, which is that material's work function, they leave the material with a maximum kinetic energy of[58]

$$E_{kin} = \frac{hc}{\lambda} - E_b - W. \quad (3.15)$$

The proportion of liberated electrons to number of incident photons is the photoelectric yield of a surface. This yield is 0 when the energy of the incident photons is below the energy needed to overcome the binding energy of an electron and the work function of the surface. The work function of a surface is not solely dependent on its material, and both surface geometry and applied electric fields can impact it. Rising photon energies lead to higher kinetic energies of the ionised electrons, and with that a higher chance that the electrons leave the surface. However, the processes of absorption, scattering of electrons in the material and surface exiting each heavily depend on the crystal structure and surface geometry of the material. Furthermore, the process is influenced by environmental conditions like temperature and electric field. A theory predicting the photoelectric yields can be found in Berglund[58], though for practical purposes it is most often determined experimentally.

With this view on the photoelectric effect we can explain the process in which the electron that is liberated from the material exits it from the opposite surface from which the photon entered the material. In the case of a thin film deposited on a

substrate transparent to photons of the wavelength used, those photons can enter the undeposited side of the substrate, travel through it and enter the deposited film. At that point the three step process takes place, and ionised electrons exit the film. With the theoretical background explored, the following chapter will deal with how this theory is turned into practical application by detailing the design and construction of all components of the MAGIX TPC.

Chapter 4

Design and Development of the Full Scale Focal Plane Time Projection Chamber

With the theory of gas detectors summarized, this chapter will deal with how this theory is implemented for MAGIX. MAGIX requires a tracking detector in the focal plane of its spectrometers. The detector will have to reach the resolution goals chosen for the spectrometer design, a spatial precision of particle track reconstruction better than 0.1 mm and angular precision better than 3.5 mrad, to achieve the desired relative momentum resolution of better than 10^{-4} and angular resolution of better than 0.05° . The acceptance of our spectrometers in turn also defines acceptance of our detectors. For a relative momentum acceptance of 15% and a circular angular acceptance of 2.75° , the plane of the active area facing the scattered electrons has to have an area of $140 \text{ mm} \times 760 \text{ mm}$.

To achieve the resolution goal, this detector has to be constructed with the minimum possible material in the path of the scattered electrons until they are detected, owing to the low energy of the experiment and the desired precision.

MAGIX plans to build three of these detectors, with two to be installed in its spectrometers and one to remain in the laboratory for tests and as a replacement if needed.

The final design of our TPCs follows up from lessons learned from the construction[49] and characterization[59] of a prototype TPC, which served as a test platform for operation of the amplification system, the electronics, their processing and data acquisition, and for the Starry Night calibration system.

The following chapter will provide an overview of the detector systems by grouping them into five hardware component groups, which will be explained in detail, along with the software.

The heart of the detector and first group of components is the amplification stage, which contains the amplifying elements in the form of the four-layer GEM stack and the readout anode.

The second is the readout electronics connected to the readout anode and their associated hardware.

The third group contains the field cage elements, both the standard field cage surrounding the active area as well as the non-standard open field cage design.

The fourth is the cathode and the Starry Night calibration system integrated into

it.

The final group is what binds all the previous ones together: the structural framing and support systems, primarily the gas mixture and high-voltage supply systems. The software consists of two main pieces: the integration of the TPC into the experiment wide slow control system, and the custom data acquisition and readout electronics configuration software called MiniDAQ.

For spatial orientation in the following, consider figure 4.1, and the coordinate system drawn therein. Due to the rotatability of the spectrometers around the central axis of our experiment, directions in an absolute coordinate system are unhelpful, and instead a co-rotating one is used.

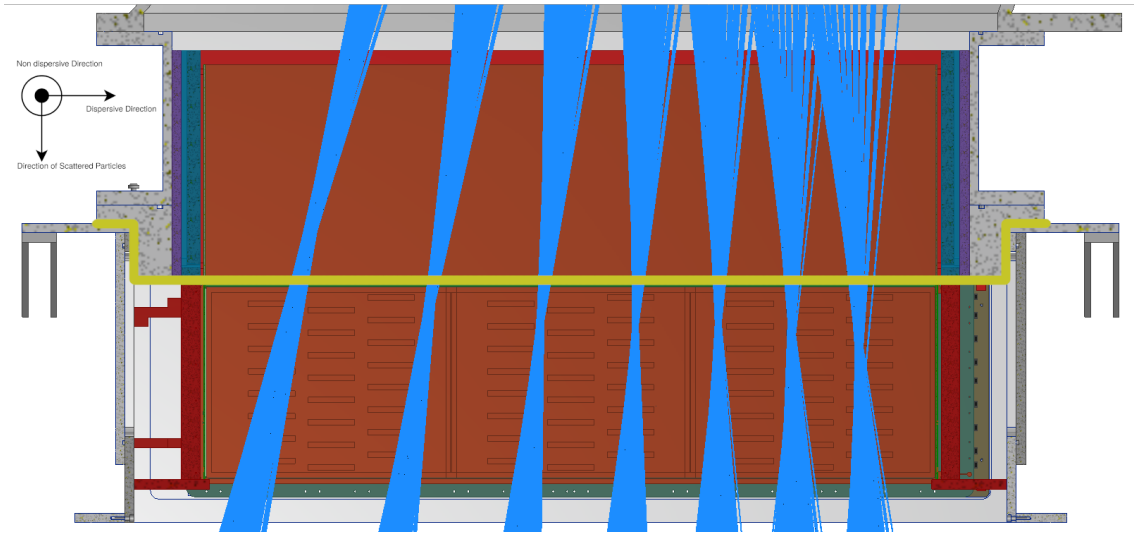


Figure 4.1: CAD rendering of the TPC active area, rendering cut in half in viewing plane to show an overlay of simulated particle tracks, with each bundle showing particles of equal momentum that fully illuminate the momentum-defining collimator. In the top left is the coordinate system most useful in describing the components of the TPC. The top component is the field cage extension and the bottom is the actual detector. The two are separated by the yellow line, a not-to-scale representation of the vacuum separation foil. The active area of the detector begins directly below this line, aligned with the focal plane, minimising the loss of angular resolution due to interactions of the scattered particles with the material of the foil.

The horizontal directions perpendicular to the vertical ideal particle track are split into dispersive and non-dispersive. The dispersive direction is outwards along the radius from the centre of rotation, and the position of scattered electrons along this direction correlates to their momentum. The non-dispersive direction is along the direction of rotation and position here relates to the target coordinates of the scattering, as explained in more detail in section 2.3.

4.1 Structural Framing and Support Systems

The structural frame and position-defining elements, which hold the detector at the correct point so that the focal plane lies directly beneath the vacuum separation foil and above the first row of the readout plane, are provided by three aluminium frames. In addition to this structural support, the detector also requires further

supporting elements, dealing with counting gas and power supply, as well as data handling. These support elements are partly situated in the spectrometer housing and partly outside the spectrometer, either in the shielded area inside the MAGIX hall or in the counting and server rooms located above.

Space inside the spectrometer shielding house is highly restricted, and components located there are exposed to an increased level of radiation, despite the shielding provided by the shielding house. As such, any components that do not necessarily have to be in close vicinity of the detectors are not installed inside the shielding house. Those that do need to be are the power supplies and the first stage data processing infrastructure.

The MAGIX hall is equipped with a shielded area for components that have connections to the detector systems sensitive to distance, but for which there is no space in the shielding house. The shielded area is connected to the spectrometers over the energy chain system. One example of such a component is the counting gas supply. All components that are not distance sensitive are installed in the above ground counting and server rooms.

4.1.1 Frame

The detector system requires three aluminium frames in total, two under vacuum, and one with the gas-filled active area and active detector components inside, all of which can be seen in figures 4.2 and 4.3. The two frames under vacuum are the spectrometer connection frame and the field cage extension. The spectrometer connection frame connects directly to the spectrometer vacuum chamber. The field cage extension hosts the components of the open field cage, explained in more detail in section 4.4.2.

All of these frames are constructed out of solid aluminium plates machined into the desired shape. This material was chosen as a compromise between four competing requirements: weight, stability, machinability and cost.

If the mass of detector systems connected to the vacuum chamber inside the spectrometer magnets exceeds the design specifications, the deformations of the chamber may reach problematic levels. The manufacturer has certified the flange to which our detectors connect to have a maximum permissible attachment weight of 120 kg. The calculated weight of the detectors, which primarily consists of the weight of their aluminium frames, has to be below this.

Simultaneously, the two upper frames under vacuum have to withstand atmospheric pressure, which places a lower limit on the mechanical strength of the frame, as well as on its construction. The large size of the vacuum chamber created by the frames and the fact that its manufacturing required welding, additionally meant that a certain degree of over-sizing was necessary. A welded connection introduces a potential structural weakness that has to be compensated for to ensure that the chamber maintains its vacuum tightness.

To fulfil these two requirements for the final product arising purely from its intended use, a material like titanium would be ideal. However, there is a step between design and finished product that gives rise to our two other requirements: construction. The frames of our detector were manufactured by our in-house mechanical workshop and were not the main focus of financial expenditure. As such the material had to be reasonably affordable and machinable. The only material that fulfils all four of

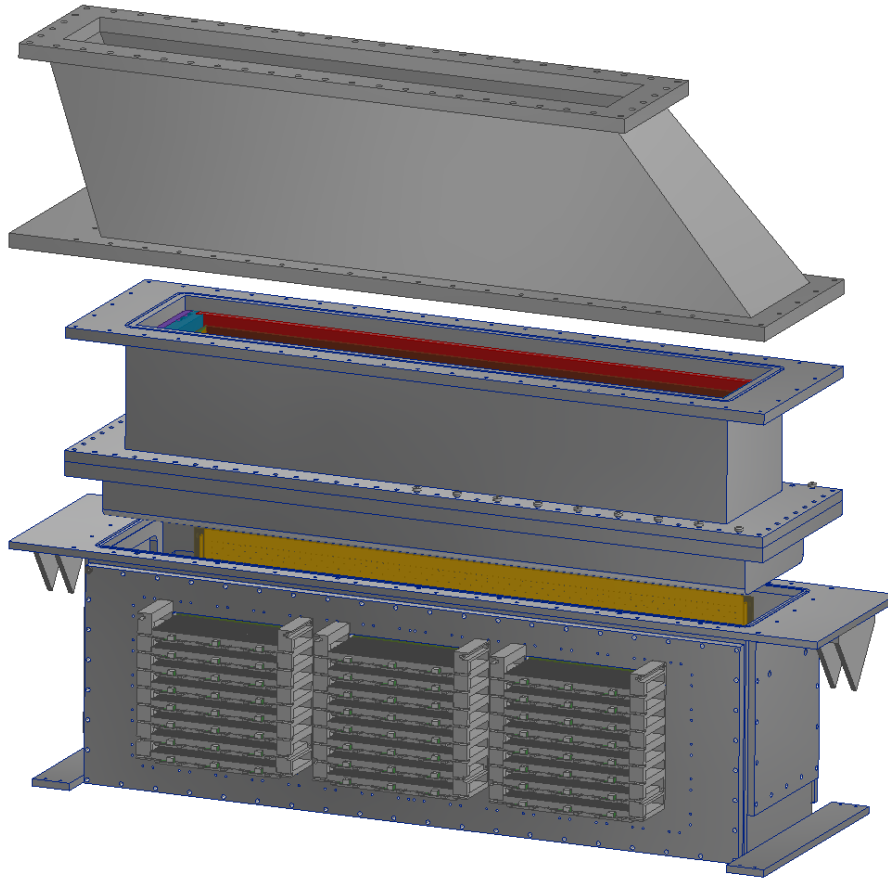


Figure 4.2: *The three frame elements of the TPC, separated for visibility. The two upper elements share the spectrometer vacuum, the lowest holds the actual detector and is filled with an argon-carbon dioxide mixture at 1 bar. The top element is the spectrometer connection frame, which contains no detector components and only serves to position the TPC at the correct position. The slanted walls of this frame ensure that the centre of the spectrometer vacuum chamber’s flange’s opening and the centre of the focal plane aligned. The middle element is the field cage extension, which contains the electrical components that enable our open field cage. The lowest element is the active area of the TPC, which hosts the amplification stage, the Starry Night calibration system, and the high-voltage and gas connectors.*

these requirements is aluminium: Aluminium can be easily machined by the CNC machines of our workshop, is inexpensive and has an acceptable strength-to-weight ratio.

After the choice of material, the choice of thickness and method of construction of the frames remained. Each of the three frames requires flanges with nuts for O-rings and screws to ensure vacuum tightness and walls of sufficient thickness to reduce the buckling caused by vacuum decompression below 1 mm at the point of highest displacement. To create this design a **C**omputer **A**ided **D**esign(CAD) software called Autodesk Inventor was used, in which all parts of the final detector were modelled. The frame surrounding the active area has to support the amplification stage with its electronics, the cathode with the Starry Night system, and two interface plates, which host the openings to bring electricity and gas into the detector. The active area is the rectangular prism within which particle tracks are detected, defined by

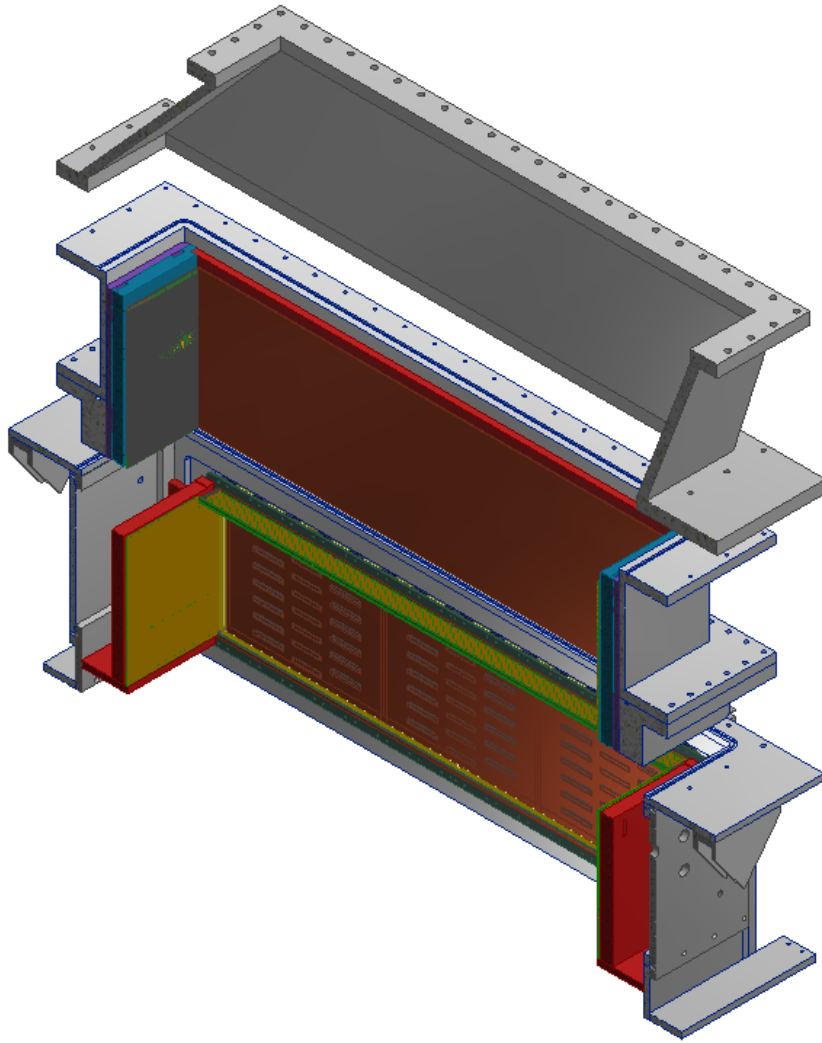


Figure 4.3: *The three components of the TPC, cut along the same plane as in figure 4.1. Not shown here is the vacuum separation foil between the field cage extension and the active area. The spectrometer connection frame is shown as empty as it will be in the final construction.*

the dimensions and position of our readout anode, the cathode above that anode and the field cage elements surrounding it. The amplification stage is stepped back 5 cm from the opening through which the particles enter the active area, to ensure that no primary particles travel through it.

The position of that active area in relation to the focal plane of the spectrometer magnets and the vacuum separation foil is crucial for both resolution and acceptance of the detector. The resolution is impacted as a higher distance of the active area from the focal plane and from the vacuum separation foil reduces the resolution of the angle and position of the particle track in that focal plane, which defines the resolution of our particle reconstruction (see section 2.3). The acceptance is more obviously influenced, as any scattered particles that do not pass through the active area cannot have their tracks reconstructed.

To optimise the position of the active area relative to the focal plane a fully parametrised

CAD model of all detector components was created, meaning that the position of each component is defined relative to the flange of the spectrometer vacuum chamber. With those models of the active components, a model of the structural frame surrounding the active area was created, which initially consisted of only a single part, as shown in figure 4.4. With this, the position of the active area was optimised until the position in figure 4.1 was found. This was mainly done by varying the dimensions of the spectrometer connection frame, which contains no active components. Due to the curving of the particle tracks created by the spectrometer magnets, the centre of the focal plane is not situated in a vertical line with the centre of the opening in the flange of the spectrometer vacuum chamber. This means that the two flanges of the spectrometer connection frame are not aligned.

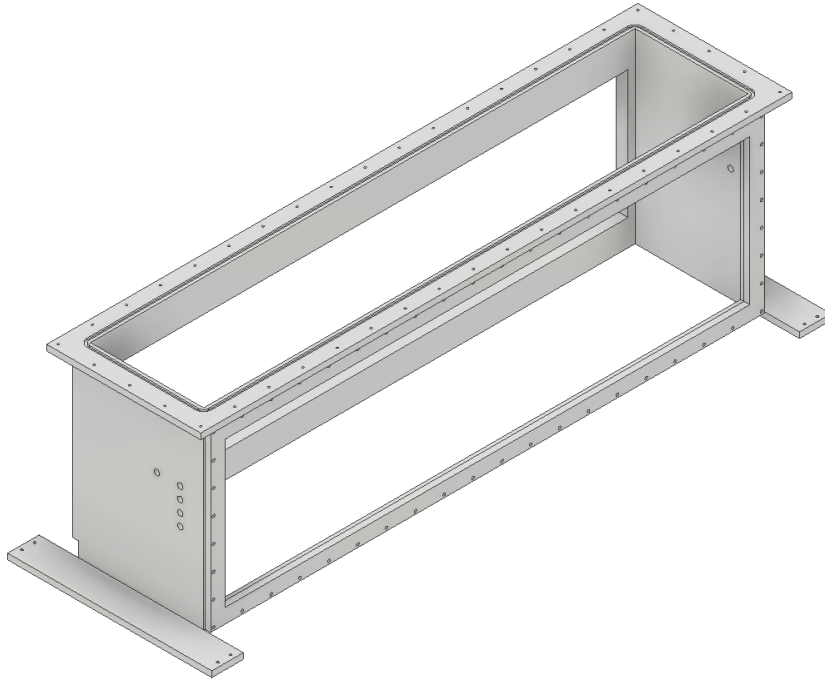


Figure 4.4: *Active area frame filling the space between the active components, before being sectioned into constructable parts.*

After the optimal position of the frame was determined, the thicknesses and construction of the vacuum containing frames was then varied and a finite element analysis performed to determine how the forces acting on the parts deform them. After several design iterations and consultation with our mechanical workshop, a design and construction method was found that fulfilled all our requirements. As a result of this iteration, it was determined that the walls of the frames had to be machined out of 10 mm thick aluminium plates, while the flanges required 20 to 30 mm to withstand the forces created by the vacuum.

As part of this iterative process, the single solid part of the active area frame was turned into five individual parts, each of which hosts a connection to one other component. The two walls in the dispersive direction are flanges to which the two interface plates connect, and the non-dispersive direction has the cathode with the Starry Night system on one side and the amplification stage on the other. These four flanges are screwed and glued to each other and into the fifth and final flange, which connects the frame to the field cage extension. The CAD model of the final design

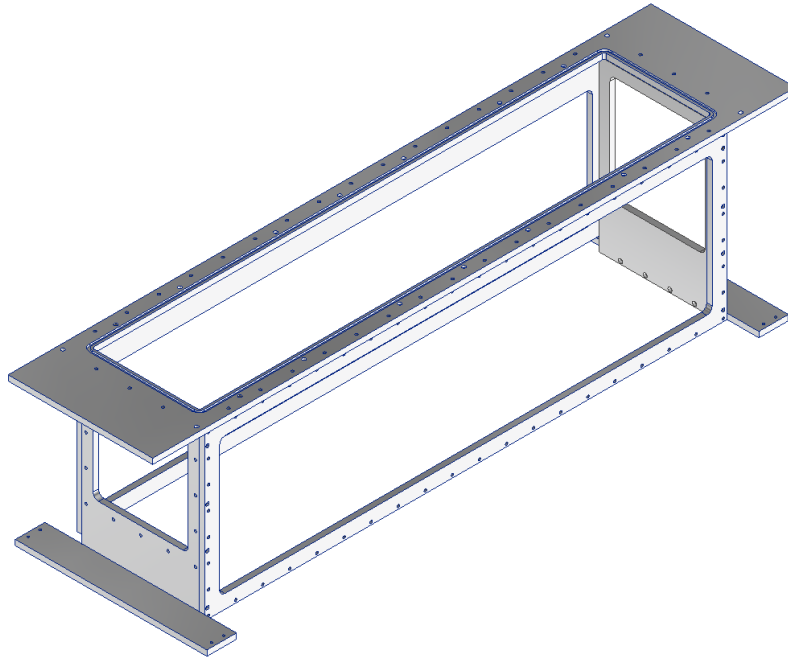


Figure 4.5: *CAD Model of the active area frame, now consisting of five separate parts.*

of this frame is shown in figure 4.5 and the constructed frame with the interface plates leaning on the sides in figure 4.6.

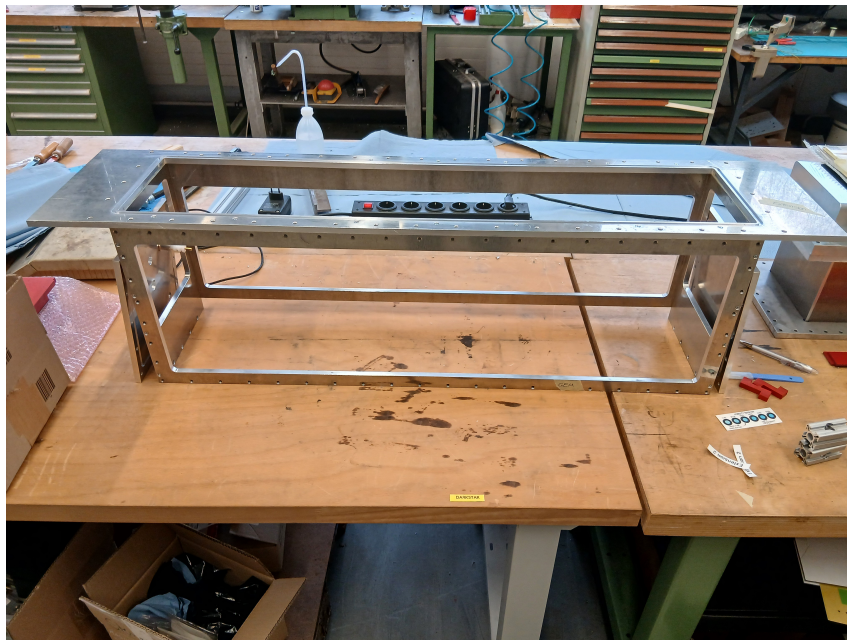


Figure 4.6: *Picture of the active area frame after component parts were screwed and then glued together.*

How the amplification stage and cathode are constructed is detailed in their respective sections 4.2 and 4.5. The interface plates can be seen in figure 4.7 and consist only of a plate with the requisite number of holes for the intended feed-throughs,

two gas connectors on both sides, four high-voltage power plugs on one side and the O-ring nut. The gas connection is split into two to enter the detector on both sides. This improves the ventilation and minimises the risk of creating areas within the detector that are insufficiently ventilated. For the same reason, the gas inputs are on the upper edge of the plate and the output on the lower, increasing turbulent flow as the heavy gas enters the chamber.

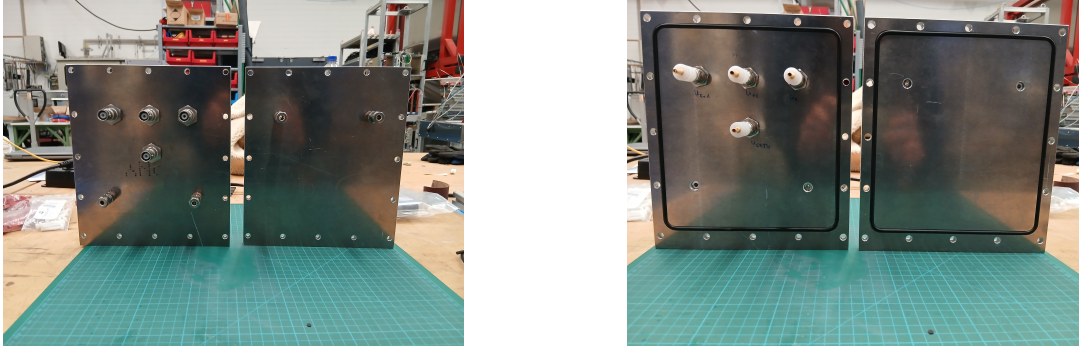


Figure 4.7: *Outside view (left) and inside view (right) of the two interface plates with four high-voltage feed-throughs on top and two gas connectors on the bottom of the left plate, and with two gas connectors on the top of the right plate.*

The spectrometer connection frame is made out of four aluminium plates and the two flanges. The plates are machined into trapezoidal shapes to accommodate the required offset. The flanges are also machined and bored with screw holes, to connect to the elements above and below.

These six elements were then welded together. One of the two spectrometer connection frames required can be seen in figure 4.8. The lower flange of the spectrometer connection is machined out of 30 mm aluminium, in excess of what was needed for mechanical considerations, to create a 10 mm buffer in case the position of the active area has to be corrected upwards in the future. A correction downwards can be achieved with a correction flange inserted between the spectrometer connection frame and the field cage extension. The spectrometer connection frame has no interface openings in its walls, as this reduces the structural integrity.

The field cage extension consists of two individual components, since the part hosting the interface between vacuum and gas filled detector requires a piece machined out of a single piece of cast aluminium, instead of an assembly of multiple parts, as is done for the spectrometer connection frame and the other component of the field cage extension. This piece has a height of 70 mm, with the flange making up 20 mm. The 50 mm elevation on top of the flange, onto which the vacuum separation foil will be glued, is needed to offset the position of the foil from the position at which the flanges meet. This offset ensures that the foil is in position directly before the first row of the readout.

The second part of the field cage extension is created out of plates like the spectrometer connection flange, without the need for trapezoids, since no horizontal offset is required or desired at this point. The pieces will be permanently fused with screws and glue. One of the two pairs is shown in figure 4.9. Like the spectrometer connection frame, the field cage extension has no interface openings in its walls, as it also contains a vacuum. Unlike the spectrometer connection frame, the field cage extension does host active components, which have to be connected to the rest of



Figure 4.8: *Spectrometer connection frame, assembled out of six parts that were welded together.*



Figure 4.9: *The two components of the field cage extension frame.*

the detector.

After the design of these CAD models was completed, they were turned into construction drawings, which were then realised by our mechanical workshop. The two

vacuum frames were additionally tested for deformation and the vacuum tightness of their welded connection by the vacuum workshop of the institute.

Glue

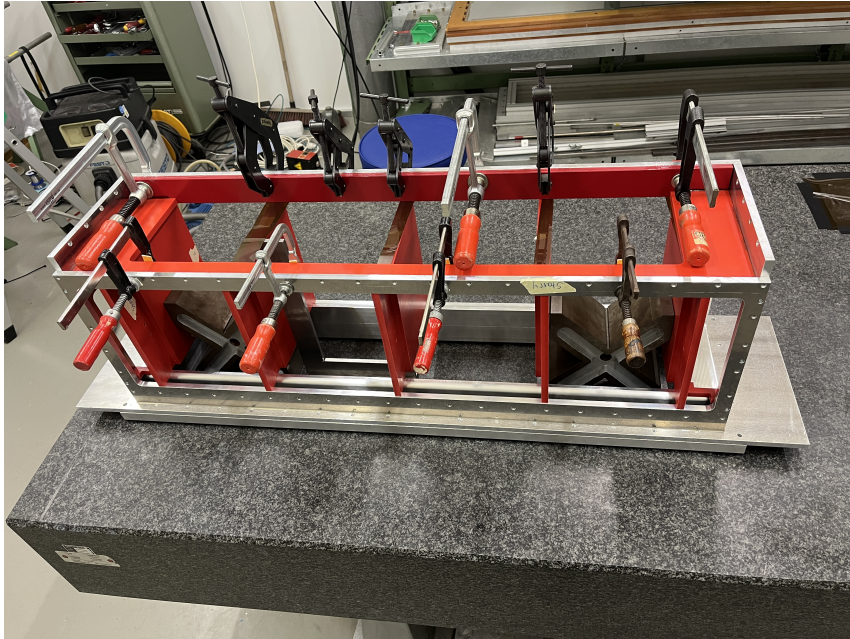


Figure 4.10: *Trovidur elements of the frame being kept in place by screw clamps while the glue is hardening.*

To connect those components that are not intended to be separated again, a two component epoxy resin called Araldite 2011 was used as glue[60]. In the following, the term glue will refer to Araldite 2011. Araldite 2011 is liquid after the two components are mixed and can be easily applied to join surfaces. It is suitable for all materials in use in our detector. It hardens at room temperature within 24 hours after application, though a temperature of 60 °C decreases hardening time and increases bond strength. The glue was chosen due to prior experience with both its radiation hardness and safety of its outgassing when combined with sensitive GEM foils[61].

Surfaces to be joined first have to be cleaned of any dust or chemical contamination that could interfere with the bonding process. After that the surface is chemically roughened to increase epoxy adhesion. With the surfaces prepared, the pieces to be joined are aligned according to the construction plans, and then fixed in place using either screw clamps for smaller pieces or small screws for large aluminium elements. Those screws exist only to ensure precision in position of the pieces during the gluing process and are not structural. With the pieces in place and their relative position confirmed, the epoxy resin is then applied by means of plastic scrapers and rubber rollers.

While the epoxy is hardening, any fixing elements remain in place to ensure no shifting while the glue settles. Figure 4.10 shows on such gluing process in progress.

Vacuum Separation Foil

The vacuum separation foil is a crucial interface. It separates the vacuum of the spectrometer from the active detector volume, in which there is a gas volume under slightly above atmospheric pressure. On the one hand, any insufficiencies in the foil or its application could lead to an implosion of the spectrometer vacuum. On the other hand, every micrometer of material decreases our detector resolution due to multiple scattering. This is complicated by the fact that thinner foils would have a larger displacement into the vacuum. This increased displacement also increases the distance between the point of scattering and detection, which worsens angular resolution. The result of this consideration was the choice of a 75 μm thick polyimide foil[62].

To ensure that our intended method of stretching the foil would not introduce any failure points, a test with such a foil was performed. The test showed that the chosen foil with our method of application could withstand atmospheric pressure, and was thus deemed suitable. An image of this test is shown in figure 4.11

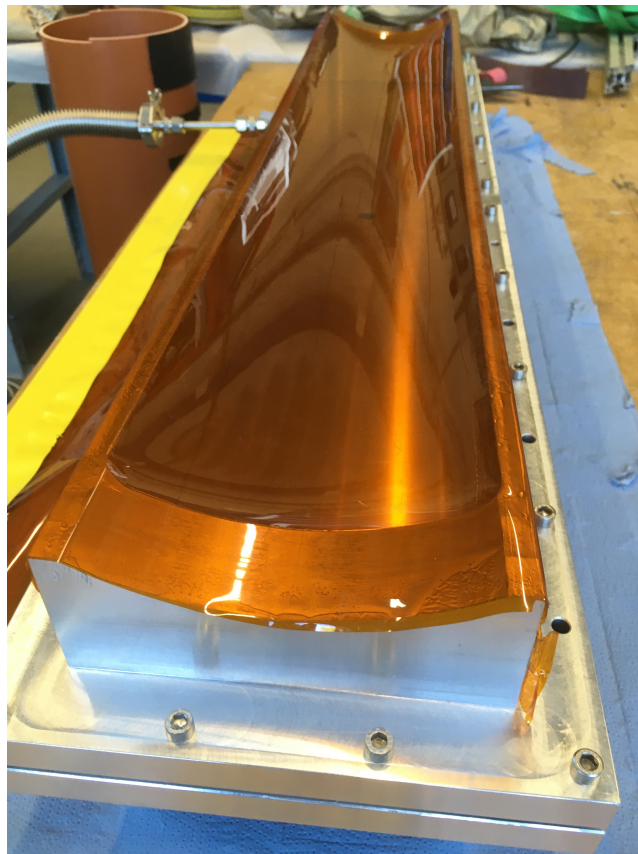


Figure 4.11: *Test setup to for the polyimide vacuum separation foil. The curvature of the elevation of this test piece is not reproduced in the final part, as it did not bring about any desired improvements, and presented a complication in foil application.*

4.1.2 Support Components inside the Spectrometer Housing

The detector also needs a gas connection to provide the counting gas mixture. The computers and electronics providing the data readout and slow control also require power, and the data they produce has to be passed out of the spectrometer. The gas moving out of the detector also has to be removed from the spectrometer, both for safety and monitoring reasons. The fans providing the cooling of the detector electronics also require a low voltage high current supply, meaning three categories of power are needed: 12 V direct current, 230 V main electricity, and a highly monitored 20 kV direct current.

As an additional consideration, all connections to the spectrometers have to reach the rotating spectrometers and must neither impede nor be impeded by that rotation for which the energy chain system of the spectrometers is essential.

High-voltage supply

The detector system and the field cage require voltages of up to 20 kV, at currents not exceeding 10 mA, with a requirement of a high-voltage stability, to reduce fluctuations of the electric field. For this, a high-voltage supply crate is installed inside the spectrometer housing.

Our high-voltage system is the EHS 40 200n[63] from ISEG, combined with a CC24[64] control board for slow control and monitoring, mounted in an ECH 242[65] crate, as shown in figure 4.12. The EHS 40 200n provides four channels of up to 20 kV and 0.4 mA, with ripple and noise below 10 mV. The output current and voltage are monitored with a relative accuracy of 0.01%, allowing for the detection of any changes of detector resistance, indicating potential damage. The CC24 board hosts a server for manual control and provides an interface for our slow control software. The managing software allows for the setting of ramp up and ramp down speeds, important for the charge up and down of the electric fields of our amplification stage, and the trip conditions in terms of threshold and time over threshold. The ECH242 crate houses one control board and up to two primary boards, manages the AC-DC transformation, providing the EHS 40 with a 24 V DC supply, and isolates the more vulnerable high-voltage boards from power surges.

Computing

To perform live filtering and trigger integration, and to reduce the number of data links needed to the outside by collating data from all detector electronics, a server is mounted inside the spectrometer housing. This server is connected to the detector readout electronics over a switch, on a **Small Formfactor Pluggable+(SFP+)** port that has a maximum throughput of 10 Gbit s^{-1} . The detectors are connected to SFP ports that have a maximum throughput of 1 Gbit s^{-1} . The switch itself has a maximum processing capability of 128 Gbit s^{-1} . This infrastructure was chosen as 10 Gbit s^{-1} is the maximum data rate produced by our data taking equipment and thus avoids presenting a choke point.



Figure 4.12: 2 EHS 40 200n voltage supply boards and CC24 control board mounted in an ECH 242 crate.

4.1.3 Support Components outside the Spectrometer Housing

All support components not situated inside the spectrometer housing are located either in the radiation protection bunker in the MAGIX hall or the counting and servers rooms.

Gas Supply and Mixing

The MAGIX TPC is intended to operate at a 9:1 by volume Argon : Carbon Dioxide gas mixture (see section 3.2.1). The mixing is done on site from high-purity gases. Flow for both gases is controlled by thermal mass flow controllers and they are combined in a gas mixing cell before being pushed out. The construction of the gas mixing and monitoring system is detailed in Constantin Szyszka's Bachelor's Thesis[47].

The gas mixture then flows by pipes into the energy chain, which runs around the interior of the spectrometer rings, bringing the gas mixture into the spectrometer shielding house. There, the gas enters the detector through the two gas connectors on the upper part of one of the two interface plates, and leaves it on the lower end of the interface on the other side.

The gas is then returned to the gas mixing system, where it is monitored continuously for its oxygen and water content.

Data storage and processing

After any potentially occurring live filtering, the data streams of the detectors are collated and have to be moved from the servers housed in the spectrometer hall to the servers that will store and process them. These are housed in the shared server room of the institute and the counting room of MAGIX, respectively. The connection between bunker and counting room is provided by ten RG58 screened cables, for diagnostic signals, twenty CAT.7a, and 5 OM5 duplex glass fibre cables, and between counting room and server by ten CAT.7a, and 5 OM5 duplex glass fibre cables. Bunker, counting room and server room are all equipped with the same switches that are installed in the spectrometers, which enables a single CAT.7a or glass fibre cable to carry 10 Gbit s^{-1} . This amount of connection exceeds the currently expected data production rates and is designed for network and damage redundancy as well as for possible future expansion.

4.2 Amplification Stage

On both spectrometers, the amplification and readout of our signals is done by a system we call an amplification stage. The amplification stage is mounted on the side of the TPC frame in direction of the incoming beam. This orientation was chosen to maximise the shielding of the sensitive electronics from beam induced background. The amplification stage consists of a GEM stack and a readout anode glued into an aluminium frame. The aluminium frame also has a nut milled into it to host a 4 cm O-ring for gas tightness.

The active detector elements of the amplification stage consist of a GEM stack above a readout anode. The amplification stage shortly before installation into the TPC is shown in figure 4.13. The amplification stage requires three total voltage levels to be supplied: ground level, supplied from the frame ground at the same interface plate the voltage feed-throughs are mounted on, the voltage of the highest GEM foil, and the voltage of the copper ring on top of the GEM supply board, which defines the lower edge of the field cage. The latter two voltages are supplied externally.

Figure 4.14 shows a CAD rendering of the amplification stage, where the voltage supply board is green instead of yellow, and the GEM foils are hidden, showing the surface of the readout anode.

4.2.1 Readout Anode

The readout of our electron signals is done by a pad-segmented readout anode. This readout anode is a multi-layered **Printed Circuit Board (PCB)**. The backside of this readout anode is facing the outside of the TPC. 72 HRS connectors are located on this face of the PCB outside the TPC. The connectors connect the channels of the readout anode to the readout electronics. The readout electronics will be explained in the following section.

The face of the anode inside the TPC is segmented into 384×24 pads with a size of $2\text{ mm} \times 8\text{ mm}$, each of which is connected to an individual readout channel for a total of 9216 channels, with an active readout area of $768\text{ mm} \times 192\text{ mm}$. The 9216 channels are distributed over three PCBs, owing to the limits of the maximum manufacturing size of PCBs by our supplier.

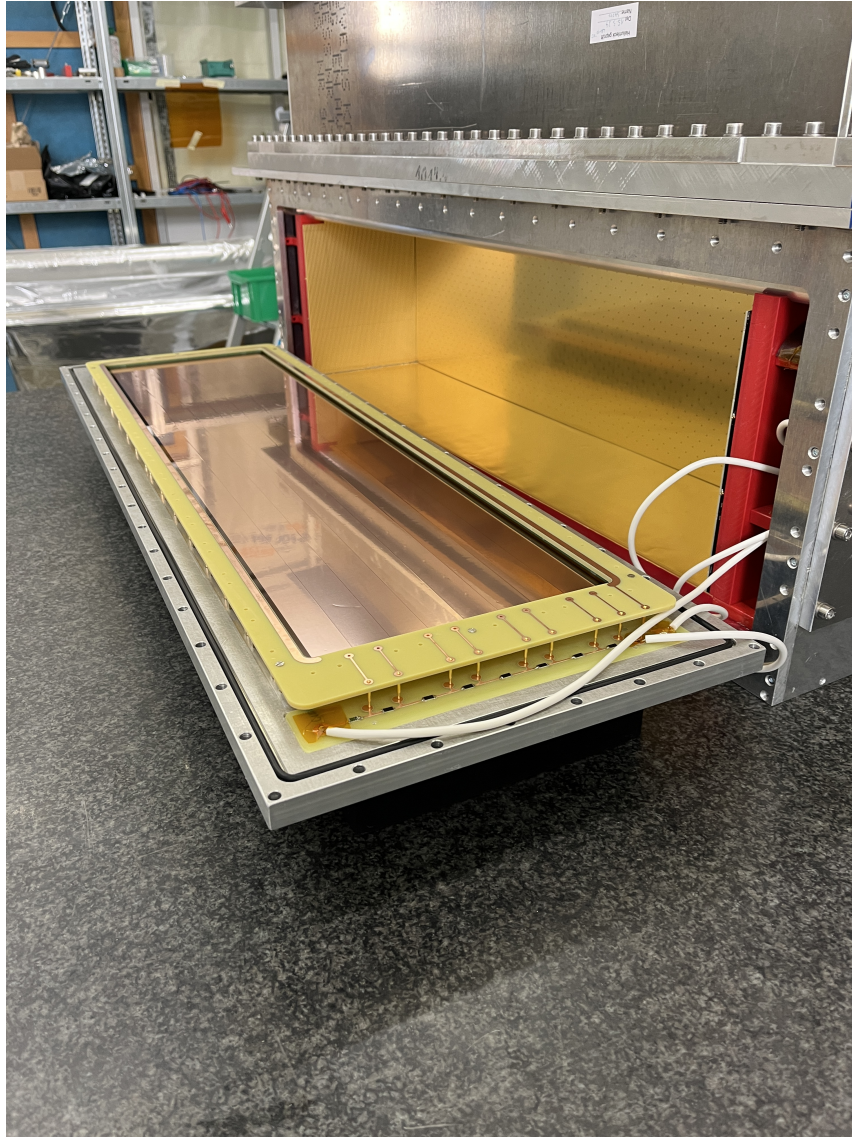


Figure 4.13: *Amplification Stage (on the left) shortly before being mounted onto the TPC frame, showing the aluminium frame, the black O-ring around its outer edge and the GEM stack in the centre. The yellow PCB visible at the top is the voltage supply board that also hosts the copper ring defining the voltage of the lower edge of the field cage. In the front, three white cables supply the three voltages required by the GEM stack to the voltage divider board. Not visible is the readout anode, being completely covered by the GEM stack.*

The design of this readout area arises from the competing desire to minimise the cost and complexity and improving signal to noise ratio with larger pads. This would minimise the number of channels required, while simultaneously achieving the desired resolution, which depends on the number of data points, requiring a high number of pads. The final choice was based on simulations[66] and compromises by choosing a rectangular pad, with the longer side running in the direction of the incoming electrons, as the resolution is more impacted by higher data point density in the focal plane, which lies perpendicular to said electrons. As an additional consideration to maximize the number of data points the rows are staggered with a periodicity of 3, to avoid regularities reducing the number of pads a track crosses.

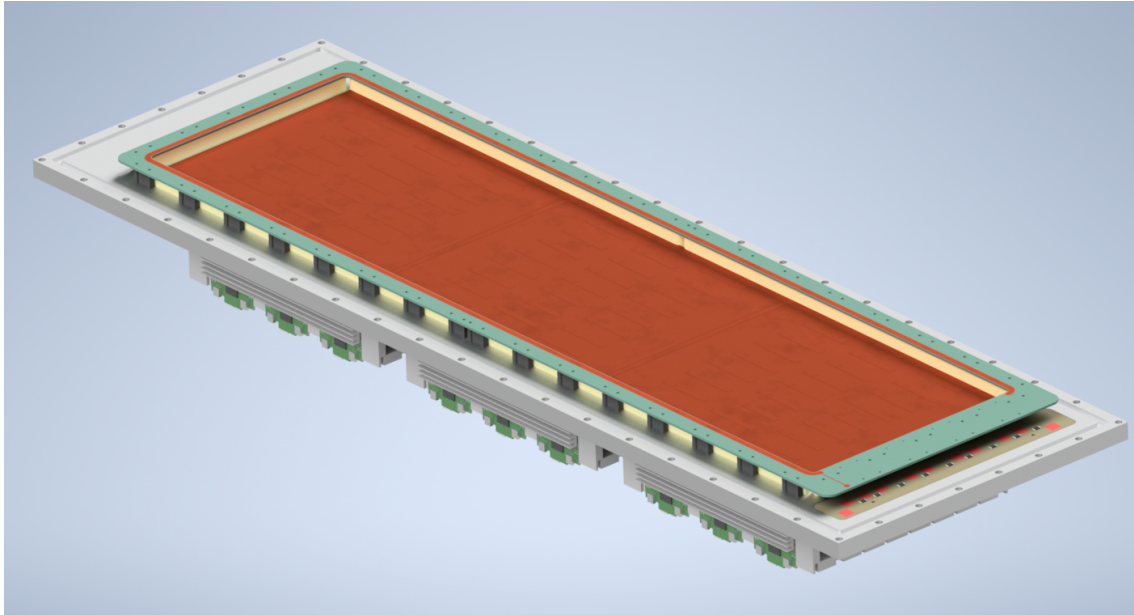


Figure 4.14: *CAD Render of detector side of the amplification stage. GEM foils and pad pattern are not included for increased visibility. The copper-coloured area in the middle is the surface of the readout anode PCBs facing the inside of the TPC. Rising above that is the NS2 stretching system, topped by the voltage supply board. On the front right edge, partly below the voltage supply board, lies the voltage divider board. The tops of the readout electronics PCBs are visible below the aluminium frame.*

Figures 4.15 to 4.17 show the readout anode PCBs, first as they are being glued into the frame, and then the finished surface of all three PCBs.

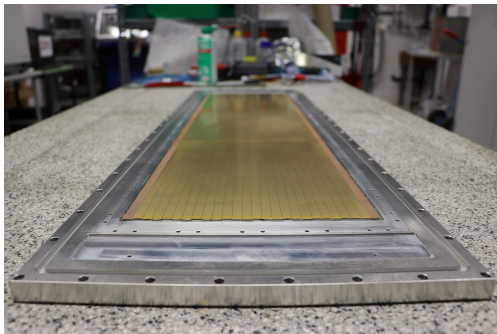


Figure 4.15: *The frame during the gluing process. The aluminium surface has to be prepared for bonding.*

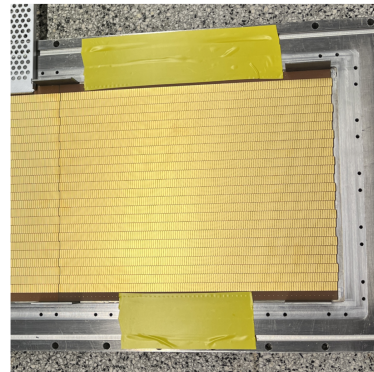


Figure 4.16: *Top view of a single readout PCB as it is being glued into the frame, the yellow tape holds it in place while the glue hardens.*

4.2.2 Four Layer GEM Stack

Mounted above the readout anode, four layers of GEM foils provide the electron amplification system. The MAGIX GEM foils have an area of $770 \text{ mm} \times 200 \text{ mm}$.



Figure 4.17: A single readout PCB glued into their aluminium frame, with the glue being applied for the next one. The yellow tape fixes the PCB in place.

All four foils per stack consist of $50\ \mu\text{m}$ thick polyimide foil with $5\ \mu\text{m}$ of copper deposited on each side. All foils have the same conical hole dimensions: an inner diameter of $50\ \mu\text{m}$ and an outer diameter of $70\ \mu\text{m}$, arranged in a hexagonal pattern. The top and bottom foils have a distance of $140\ \mu\text{m}$ between neighbouring holes, the middle foils $280\ \mu\text{m}$, and each foil has its hole pattern 90° rotated with regard to the previous foil. Varying hole pitch and pattern arrangement optimizes charge distribution and minimises the possibility of a single discharge affecting multiple foils by preventing line of sight between anode and cathode through the holes. The GEM foils are stretched to ensure their planarity using the NS2 system developed by CERN[67]. The foils are tightly screwed into a plastic frame, which is then tensioned by screws pulling the frame against brass blocks set around the circumference of the frame. By adjusting screw tightness, foil tension can be calibrated until the desired flatness is achieved. A schematic of this system is shown in figure 4.18, while figures 4.19 and 4.20 show these two steps. This frame is then fastened by screws to the aluminium flange to which the readout anode was glued beforehand.

The screws will be glued over to achieve gas tightness of the final system.



Figure 4.18: *NS2 Stretching Systems, as developed by CERN for the new generation of CMS GEM foils. Image from [67].*

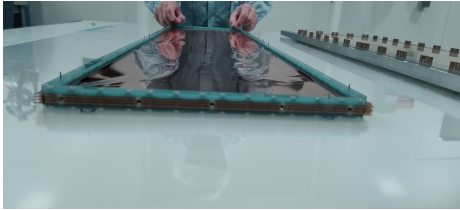


Figure 4.19: *MAGIX GEM foils screwed into the plastic frame. The visible foil surface shows rippling indicating insufficient tension. At the front of the stack the holes for the tension screws are visible, to the side lies the aluminium frame with readout anode and brass blocks visible.*

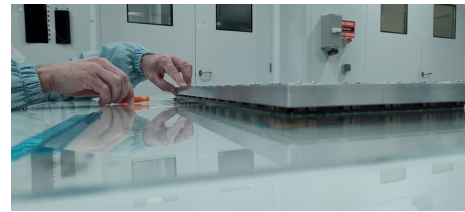


Figure 4.20: *Tensioning of the 40 screws against the brass blocks is done by a careful and experienced hand.*

The voltages are supplied to the GEM foils using spring-loaded contacts of different lengths to reach the contacts on the GEM foils at their varying depths. The spring-loaded contacts for the GEM foil receive their voltages from the voltage supply board, which tops the GEM stack and the SN2 system. This voltage supply board receives its voltages in turn from a voltage divider board, to which the externally supplied voltages are delivered. Both are shown in figure 4.14.

Each GEM foil receives a top and bottom voltage to drive amplification across it. The readout anode serves as ground, since it is electrically connected to the readout electronics. Between the top of one foil and the bottom of the next an induction voltage is applied to drive electrons across the gap. Tuning these voltages can significantly change the amplification and discharge behaviour of the stack. One additional potential level lies above the highest GEM foil, which is applied to a copper surface on the voltage supply board. This potential is the highest voltage supplied to the voltage divider board and is the first of the voltages supplied externally. One possible choice of voltage settings can be seen in table 4.1. For more information about fine-tuning the voltages, see the Bachelor's Thesis by Lucie Bister[68]. For more information about the GEM foils in general, see the dissertation of Pepe Gülker[69].

4.3 Readout Electronics

The 9216 pads of the readout anode each require a dedicated processing channel. The electronics that process each channel must meet these requirements: the large number of channels must be affordable, the time resolution must be 1 ns or better

Position	Voltage	
	relative	absolute
GEM Foil 4	320	3325
Induction 3-4	400	3005
GEM Foil 3	310	2605
Induction 2-3	400	2295
GEM Foil 2	200	1895
Induction 1-2	400	1695
GEM Foil 1	295	1295
Induction Anode-1	1000	1000

Table 4.1: *Lowest level of voltages used in operation tests for the amplification stage[68].*

and the detector must sustain at least a 1 MHz rate of particle tracks. For this, we use a type of **A**pplication **S**pecific **I**ntegrated **C**ircuits(ASICs) with the name of **V**innie’s **M**icro **M**egagas(VMM), named after their original developer and intended use case.

A schematic drawing of the architecture for this ASIC can be seen in figure 4.21.

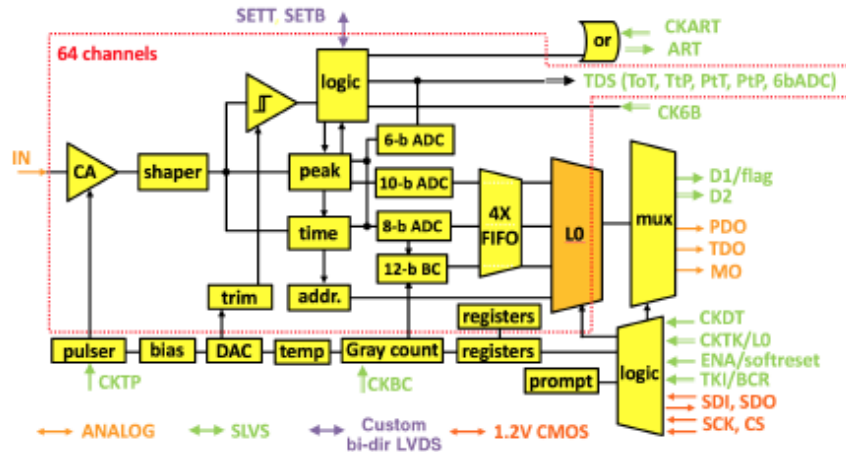


Figure 4.21: *Schematic drawing of the architecture of a VMM ASIC. The signal undergoes the signal processing chain as described in section 3.2.4, beginning with the integrating amplifier, labelled CA here, which can be configured for a variety of different gains for both positive and negative signals. The shaped signal is compared with a global threshold, with per channel offsets, to see whether a readout is triggered, which can also happen when the logic unit receives a neighbouring signal. This neighbouring signal is sent by a triggering channel to its neighbours, to trigger a readout even if these channels are below the threshold. If the logic triggers a readout, the peak height and precise time of the signal are digitised with the **A**nalog **D**igital **C**onverters(ADC). The precise time is generated by measuring the height of a ramped signal, in a **T**ime to **A**nalog **C**onversion(TAC). Image from [70].*

A single VMM ASIC produced according to this architecture has the following capabilities[70]:

- Self-triggering with rates per channel up to 4 MHz

- Globally and per channel configurable triggering threshold
- Neighbouring logic that allows neighbour channels of self-triggering primary to also be read out
- Time resolution of $\mathcal{O}(<1 \text{ ns})$
- 8 different pre-amplifier settings $0.5\text{-}16 \text{ mV fC}^{-1}$ for positive and negative signals
- Requires one 2.9 V and one 3.9 V power supply.

4.3.1 VMM Hybrids

Two of these ASICs are then combined into a VMM hybrid, which additionally hosts a **F**ield **P**rogrammable **G**ate **A**rray(FPGA) responsible for digital data transmission, ASIC configuration and time keeping. The hybrid connects to the readout anode over 140 pin HRS connectors, 128 of which are signal channels. The data transmission, slow control and configuration of the hybrids is done with an HDMI cable, which in our application also carries the 2.9 V and 3.9 V levels to the hybrids. To avoid ground return distorting our signal voltage levels, the hybrids have an additional ground connection to their AUX port, which could alternatively also receive the power supply.

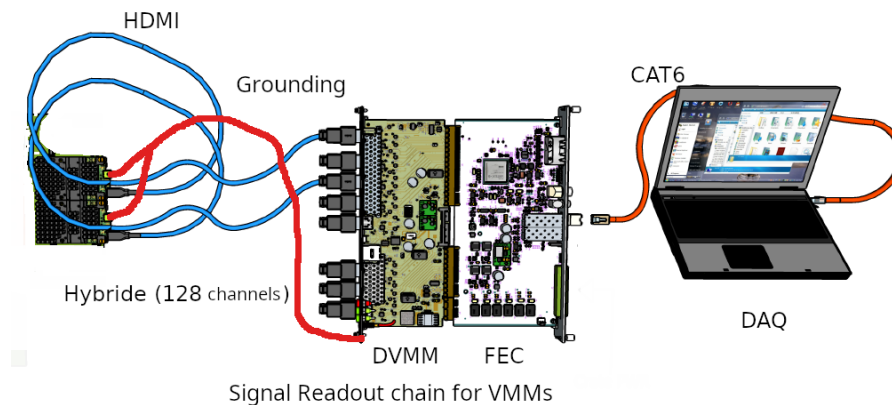


Figure 4.22: Schematic of the VMM hybrid readout chain for two hybrids. Figure from [71].

For more information about VMM hybrids, see L. Scharenberg et al.[71] and my Master’s Thesis[59].

The 9216 channels of the readout anode require 72 VMM hybrids in total. Consequently, each of the three readout anodes hosts 24 connectors. Since each row has a vertical height of 8 mm, which is less than the height taken up by one of the hybrids, the connectors are staggered in sets of three.

Cooling the Hybrids

A single VMM hybrid produces up to 3.5 W of waste heat, which has to be removed to keep the ASICs’ temperature below 60 °C for proper operation. Operational constraints prohibit the use of liquid cooling, as supplying the cooling liquid without possible leaks damaging the electronics was deemed prohibitively complex. With

regard to air cooling, the standard cooling blocks intended for use with VMM hybrids raise their thickness to 45 mm, which exceeds the maximum height per row of 24 mm. This maximum height corresponds to three readout rows, which are read out by one row of hybrids.

A custom cooling and support solution was designed and implemented to deal with this and to provide structural support for the three-dimensional arrangement of the hybrids. This structural support consists of extruded aluminium profiles, which were cut into a shape that leaves the connector elements at the back and front of the hybrid open, covers all active components producing heat and has a total stack height of 2.3 mm, fitting into the maximum height and providing adequate cooling capacity when combined with high static pressure fans.

The three hybrids of one row are mounted between these aluminium profiles, with thermal paste serving as interface and electrical insulation above the ASICs and the FPGAs. The remaining aluminium surface oriented towards the hybrids are covered with plastic to prevent a short circuit between components on the hybrid and the electrically conductive aluminium. One of these sandwiches is shown in figure 4.23.

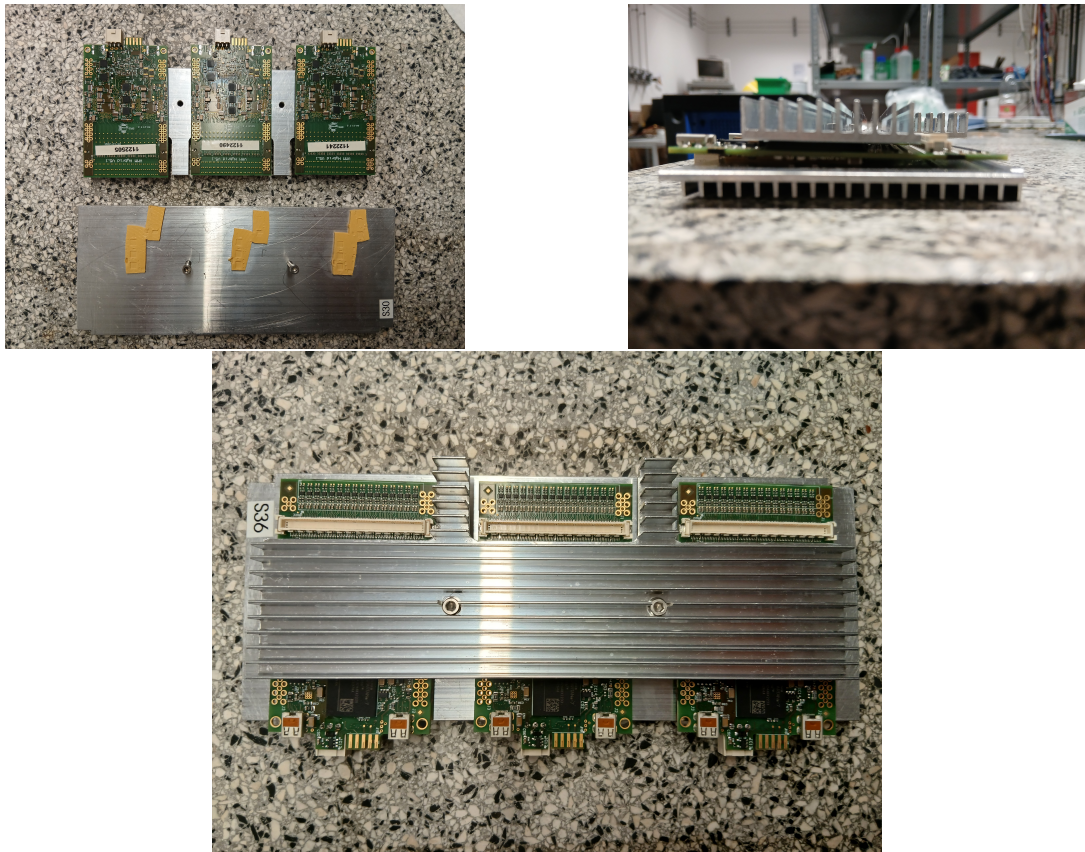


Figure 4.23: *One VMM hybrid sandwich, with three VMM hybrids. Top left image shows a sandwich opened up, showing the electrically isolating, thermally conductive pads covering the high components on the hybrid. Also visible are the white Aux connector boxes, which are used to connect the ground connection. Top right image shows a side view demonstrating the air channels and low total height of the sandwich. The bottom image shows the HRS connectors for connecting to the readout anode at the top, and the HDMI connector at the bottom of each of the hybrids.*

4.3.2 FECs and DVMMs

The hybrids are connected in groups of eight by combined data and power HDMI cables to a **D**igital **V**MM(DVMM) card, which combines their data streams and sends the power supply and control and configuration signals back to the hybrids. To reduce distortions of the data signal carried by the HDMI cable due to ground return caused by simultaneous power transmissions, each hybrid is also grounded to a separate port on the DVMM card. Each of the nine DVMM cards is connected to a **F**ront **E**nd **C**oncentrator(FEC) card, which hosts an FPGA responsible for UDP communication with the control and data acquisition server.

The communication between FEC and server is done with UDP jumbo packets, with an oversized packet size of 9216 bits. These 9216 bits are divided into 192 48 bit hits containing the information of the measured events. The format for one hit is shown in image 4.24.

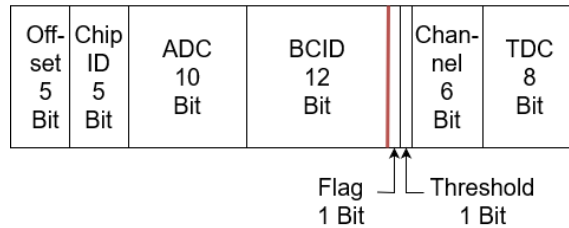


Figure 4.24: Bit format of the communication between FECs and server. Offset and BCID combine into a 17-bit global time, chip ID and channel identifying the ASIC, connected to the FEC, from which the hit originated, and from which channel on said ASIC. ADC is the output of the digitisation of signal height and TDC of the digitisation of the time ramp, which serves as fine time. The threshold bit identifies whether readout was triggered on the channel or from a neighbouring signal, and the flag differentiates the packet as belonging to a detector event, as opposed to packets responsible for timing coordination.

Each of the nine FECs is connected to the switch, which transfers their data to the server in the spectrometer shielding house. The distribution of hybrids to FECs is shown in 4.25.

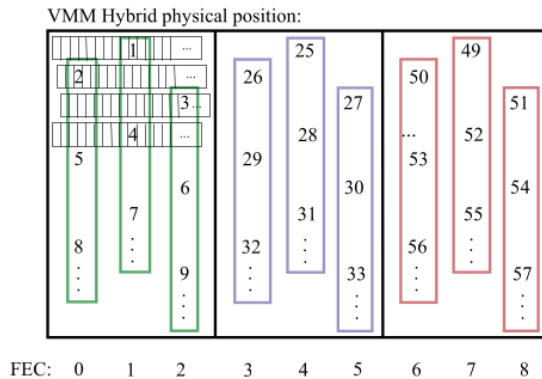


Figure 4.25: Schematic drawing of the position of the SRS connectors for the VMM hybrids on the outward side of the three readout anode PCBs, displaying the 24 rows per PCB, 8 hybrids per FEC and the staggering of the connectors. Figure from [45].

A fully equipped amplification stage with the FECs connected can be seen in figure 4.26.

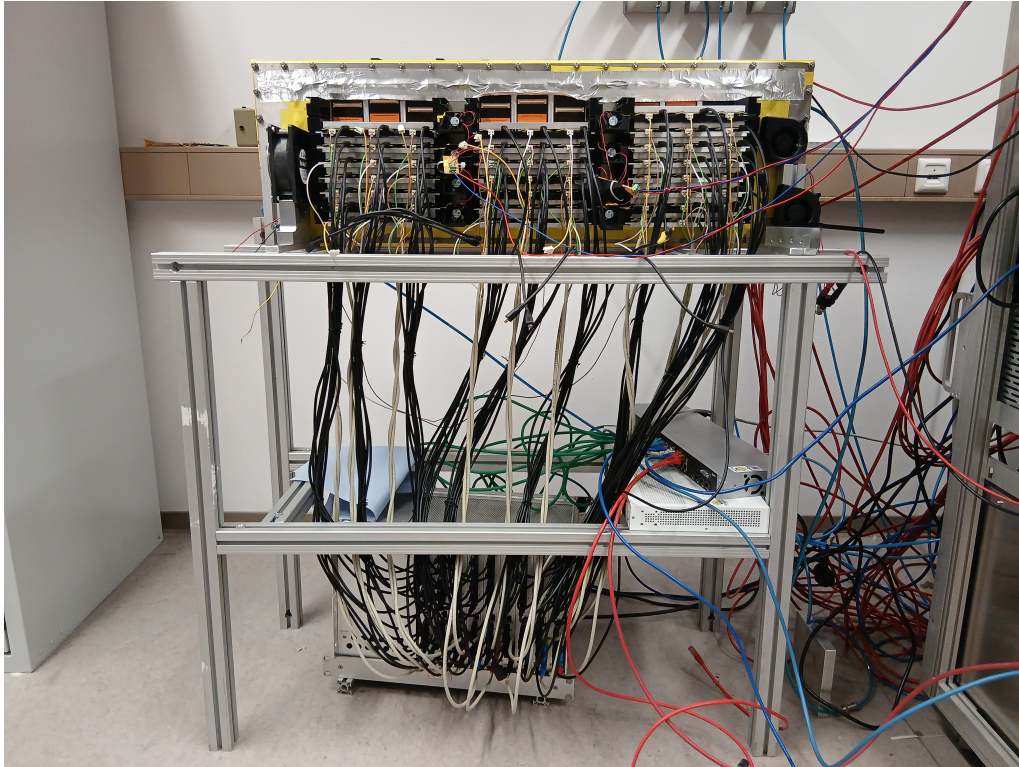


Figure 4.26: Fully equipped amplification stage, with all 72 hybrids, in 24 hybrid sandwiches, with the SRS crate hosting the FECs visible below.

4.3.3 VMM Configuration Registers

The FECs and the VMMs they are connected to have to be configured. For this, they have to receive UDP packets that contain an assignment of each configuration register. Tables 4.2 and 4.3 show a list of all relevant registers that have to be set for each application.

The global registers match the behaviour of our signal processing chain to the shape of the incoming signal. By adjusting the self triggering threshold, electronic noise below the level of our signals is cut off. The TAC rise time defines the rate at which the ramp signal rises. Since this signal is being digitised with eight bits, see figure 4.24, an increase in the signal rise time here increases the duration each bit of the digitisation encodes, and so decreases timing resolution. The rise time has to be adjustable to account for differing clock frequencies, which might have periods longer than the shortest rise time, and so might lose timing information for some part of their clock cycle. The neighbouring logic can be turned off for cases in which adjacent channels on the VMM are not expected to trigger each other. The gain sets the conversion rate between charge and signal height of the integrating amplifier. The peak times determine the time period over which the amplifier integrates.

ADC offsets (bits 1-12 in the local register) and trigger thresholds (bits 13-17) have to be set separately for each channel to compensate for the specific characteristics of each channel due to limitations in manufacturing. The structures of the elec-

Register	Name	Value	Bits					
			31	30	29	28	27	26
0x44	Threshold L	0	0	0	0	0	0	0
		1	0	0	0	0	0	1
	
		63	1	1	1	1	1	1
0x45	Threshold R	0			0	0	0	0
		64			0	0	0	1
	
		960			1	1	1	1
0x45	TAC [ns]	60	0	0				
		100	0	1				
		350	1	0				
		600	1	1				
0x45	Neighbouring Logic	off						0
		on						1
0x45	Gain[mV/fC]	0.5			0	0	0	
		1			0	0	1	
		3			0	1	0	
		4.5			0	1	1	
		6			1	0	0	
		9			1	0	1	
		12			1	1	0	
16			1	1	1			
0x45	Peak Times[ns]	200	0	0				
		100	0	1				
		50	1	0				
		25	1	1				

Table 4.2: Global registers for one VMM. All register bits of 0x44 and 0x45 not listed here are not read by the VMM FPGA. The choice of which bits code for information and which don't is historic. The threshold register, which sets the triggering threshold globally for all channels, is split between two registers due to its size. The threshold applied to the triggering logic is the sum of the values of Threshold L and Threshold R listed here. Peak Times determines the length of integration of the amplifier.

tronics implementing the ADCs and the triggering logic are not perfectly identical between the different channels on a board, or between different boards, and generate slightly different results from identical signals. To correct for these differences and ensure equal signals from different channels correspond to equal signal heights, the ADCs and trigger threshold have to be calibrated separately. Each channel has the capability to generate test pulses for calibration.

These test pulses have two options related to the individual channel settings: first, if test pulses are generated (bit 21), second, which one of the two on-board capacitors per channel is used (bit 20). The test pulses are created by charging one of those

Name	Explanation	Bits
SZ06b	Offset for the 6 Bit ADC, between 0 and 7 mV	1-3
SZ08b	Offset for the 6 Bit ADC, between 0 and 15 mV	4-7
SZ010b	Offset for the 10 Bit ADC, between 0 and 31 mV	8-12
SD	Per Channel trigger threshold, between 0 and 31 mV	13-17
SMX	Output-Mode, irrelevant for our application	18
SM	Channel mask, 1 deactivates the trigger logic for the channels	19
STH	Test pulse-Capacitor, 1 increases test capacity by a factor 10	20
ST	Test pulses, 1 activates	21
SL	Leakage current shielding, 0 activates	22
SC	Large sensor capacity, 1 activates	23

Table 4.3: *Local Register of one VMM channel, on register positions 0x03-0x42.*

two capacitors, with a known and identical capacitance, and discharging them on receiving the time signal from the hybrid FPGA. In this way, signals of known height are created at known times. These signal can then be used to calibrate the per channel offsets of the electronics.

Leakage current shielding(bit 22) and large sensor capacity(bit 23) are options to activate when the problem they were designed to deal with arise. A leakage current could arise due to device defects or damage, and can be somewhat compensated for by activating the shielding against it. The large sensor capacity increases sensor capacity to deal with high amplitude signals.

4.4 Field Cage

The remaining four sides of the active area of the detector, that are not covered by either the anode or the cathode have to ensure that the electric field lines inside the active area are as straight as possible. Deviations from a straight line reduce resolution significantly. Deviations would occur, for example, if cathode and anode were to act as a parallel plate capacitor, where exterior field lines bow out from straight, reduce resolution significantly. The field lines get regularized by placing active elements on all sides, so that these elements step down the voltage between cathode and top GEM foil.

For the MAGIX TPC, the two sides in the non-dispersive direction host the anode and cathode, and the two sides in the dispersive direction are equipped with standard active field cage PCBs. Along the particle entrance direction, however, such material would reduce resolution via multiple scattering. To reduce the material budget, MAGIX developed the open field cage concept. With this, the only material scattered electrons interact with after the target is the 75 μm thick polyimide foil at the vacuum interface.

The field cage requires a total of three voltage inputs: First, the lower active area field cage voltage, which it receives from the top of the amplification stage. Second, the anode analogue voltage, which is one of four voltages passed in externally. Third, the cathode voltage.

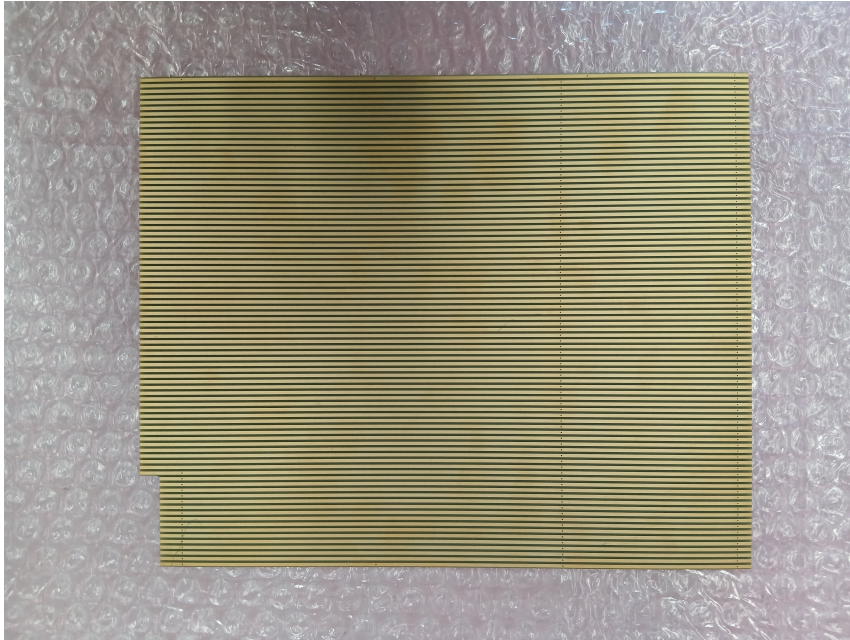


Figure 4.27: *One example of a field cage PCB, this one covering one of the dispersive side of the active area. The open field cage will be on the left when this PCB is installed. The potential lines, shown by the exposed copper and separated by the grey lines of isolator, are uniform here, as they have to provide a uniform field. The visible dots are the vias that carry the voltage from the voltage divider on the backside.*

4.4.1 Active Area Field Cages

The open field cage, the anode and the cathode leave three sides in the TPC that require field cages. The two non-dispersive sides are covered with PCBs, with linear potential lines exposed on the surface: one of these can be seen in figure 4.27. The voltage dividers for these field cage elements receive the top voltage from the cathode and the bottom voltage as the second externally supplied voltage, at a value identical to the voltage at the top of the amplification stage, to keep them and the field cage electrically separated.

To isolate the aluminium of the frame from the high voltages of the active area, these field cage elements are mounted on polyvinyl chloride blocks, which are in turn glued to the aluminium frame.

The exit of the TPC in direction of the scattered electrons is covered by another polyimide foil, this one with conducting strips defining the potential lines printed on. This exit foil receives its voltages from the previous two field cage elements.

4.4.2 Open Field Cage Extension

The purpose of the open field cage at MAGIX is to move the active components necessary to create a homogenous electric field outside the path of the scattered electrons. An analytic solution for the field lines was derived by Harald Merkel[72], from which a charge distribution can be calculated that produces the necessary field homogeneity by expanding the field cage elements on the four sides surrounding the scattered electrons significantly above the focal plane.

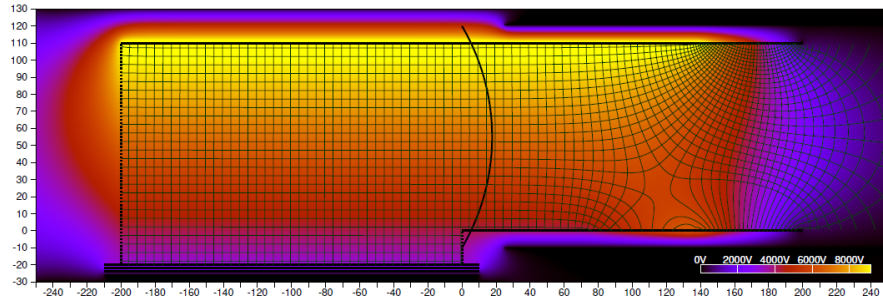


Figure 4.28: *Calculated solution for electric field and potential lines of an open field cage. The black line separating the gas volume on the left and spectrometer vacuum on the right is the gas-tight foil. The GEM foils are at the lower end of the gas volume, lowered by a step to keep the GEM foils outside the direct path of the scattered electrons. The right side shows a saddle point in the field, and at the end, the distortion that arises from having no potential-defining elements along its path, which is moved forward from the focal plane. Figure from [72].*

Four of the six field cage elements required for this are mounted in the vacuum side field cage extension, covering all sides. One of these elements is shown in figure 4.29. The remaining two are inside the active area and cover the step-down to the GEM foils.

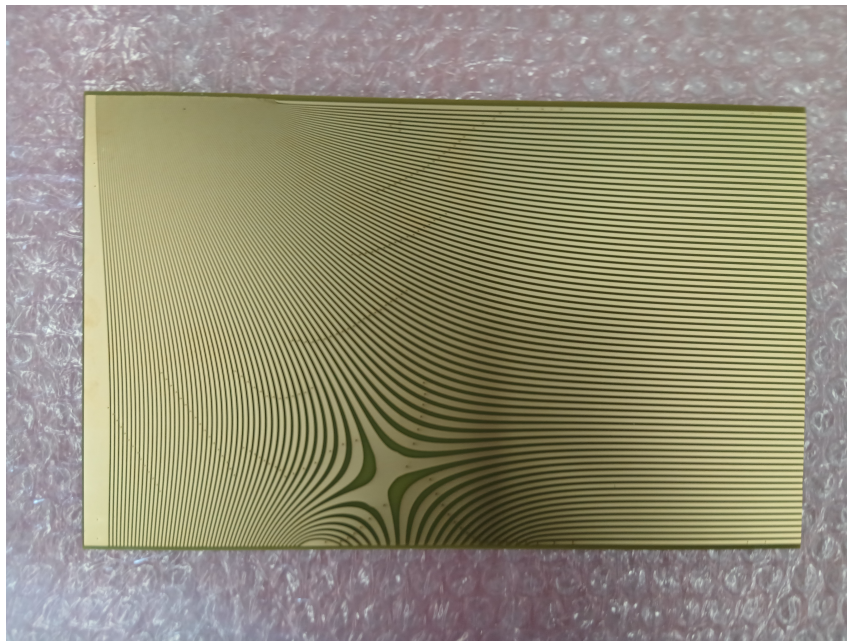


Figure 4.29: *Open field cage extension PCB, covering the dispersive side. The active area will be on the right, when this is PCB installed, and as such the potential lines are uniformly distributed on that end.*

The former four require three voltages to define their potentials: the voltage of the cathode, the voltage of the anode analogue, and a ground. The anode analogue of the field cage extension is the third externally supplied voltage. These three voltages are passed through the vacuum separation foil using spring-loaded contacts, as mentioned above. The latter two receive their voltages directly from the field cage

elements mounted on the non-dispersive sides of the active area.

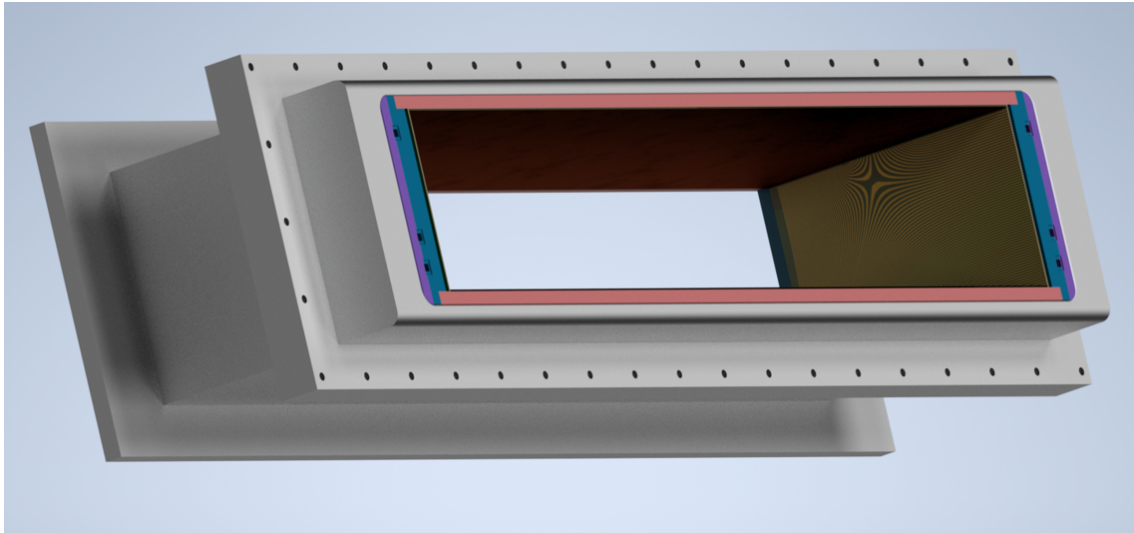


Figure 4.30: CAD rendering of the field cage extension, showing the interface surface onto which the polyimide foil is glued. The visible field cage element shows the saddle point in the potential lines. The polyvinyl chloride isolation blocks here rendered in three colours, blue, red and purple, are all red in reality. The blue elements show the depressions in which the contact plates for the spring-loaded contacts will be glued, and host the cable guides to connect all electronics. The red elements are the top and bottom isolation, and the purple elements the side isolation.

To maintain vacuum tightness, and to avoid openings in the walls of the field cage extension frame weakening its structural integrity, these voltages are passed through the vacuum separation foil by use of spring-loaded contacts mounted on the TPC, instead of using dedicated high voltage vacuum feed-throughs. The spring-loaded contacts connect to receptacles glued into holes in the field cage extension when the TPC is mounted under the spectrometer.

A CAD rendering of this field cage extension is shown in figure 4.30.

4.5 Starry Night

To achieve the desired precision in track reconstruction, it is necessary to diagnose and correct potential deviations in the electric field lines. These can be caused by charging up of isolating materials in the detector, with the greatest potential for concern lying in the thin polyimide vacuum separation foil, where the highly energetic scattered electrons may knock out electrons. At high rates, this might lead to a significant charge, which has to be measured and accounted for when calculating particle trajectories.

At those same high rates, even highly suppressed ion backflow can lead to a build-up of space charges in the drift volume. This also leads to changes in the drift behaviour of primary electrons, which have to be measured and corrected. Those changes in the drift behaviour can be measured using electrons traversing the detector with precisely known position and time of creation. This allows constant monitoring of the actual drift field during a measurement. The calibration system for MAGIX is called Starry Night.

Starry Night works with an application of the photo effect as explained in section 3.3.2. UV light is created in very short pulses and directed onto the cathode, where it causes some electrons to be released from some spatially restrained points. These electrons are then liberated from the surface by an electric field. The design of this photoelectron calibration system was informed by research done for a similar system for the T2K TPC[73] and the dissertation of Dimitri Schaab[74].

The T2K TPC uses a 266 nm-laser and fibre optic cables to direct the light from the anode onto the surface of the cathode, which consists of a copper plate with aluminium patterns deposited on it. As can be seen in figure 4.31, while 266 nm wavelength light has sufficient energy to liberate electrons from aluminium, it lies below the threshold for copper, thus the spatial localisation of the creation of the electrons is given by the position of the aluminium on the surface of the cathode.

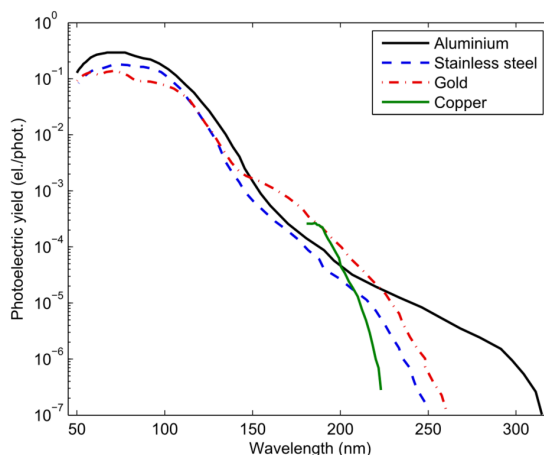


Figure 4.31: Photoelectric yield of different materials as a function of the wavelength[75].

4.5.1 Prototyping the Starry Night Concept

The design principle of the T2K TPC calibration system is applicable to MAGIX, but implementation requires major alterations. The primary reason for this is that MAGIX does not have the space for the fibre optic cables on the anode or around the rest of the detector. However, an initial test using a mercury vapour lamp, which has a peak at 254 nm, shining on aluminised Mylar showed promise. In this setup, which can be seen in figures 4.32 and 4.33, the lamp was mounted on the outside of the detector and a small fused quartz window provided localized light access. Below that laid a cathode made out of a single sheet of aluminised Mylar stretched on top of a GEM stack as a detector.

In this setup, light passes through a transparent material before interacting with the opaque material from which the electrons are generated, in this case, Mylar foil deposited on one side with aluminium. With this, a signal was generated below the window when the lamp was turned on, indicating that some electrons produced by the photo effect were leaving the surface and hitting our detector[76].

To introduce the ability to trigger the light to generate electrons at precise times, a setup roughly equal to the one in figure 4.32 was constructed, replacing the mercury vapour discharge lamp with a 275 nm LED. The LED was connected to electronics

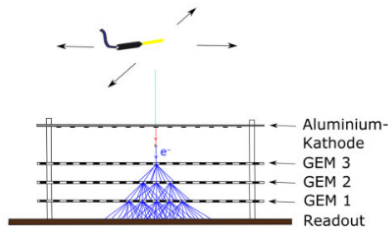


Figure 4.32: Schematic drawing of the setup of the initial tests of the then not yet named *Starry Night*. Image from [76].

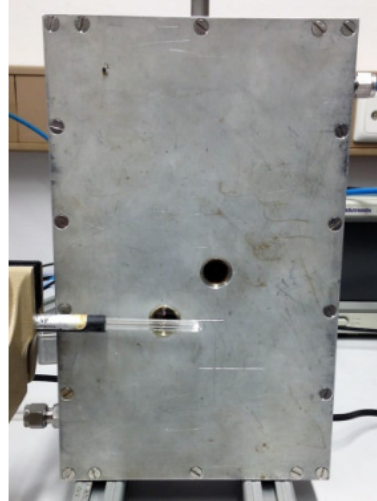


Figure 4.33: Photograph of the setup constructed according to the schematic in figure 4.32, contained in the aluminium frame, with only the mercury vapour lamp and the fused quartz windows visible. Image from [76].

designed to discharge a capacity when a transistor gate was opened, allowing us to generate 10 ns pulses. Using this setup, it was not possible to generate a clear signal of detector events correlated to the triggering of the LED. The best result, for a ten-minute measurement, is shown in figure 4.34.

Further research revealed that Mylar has negligible optical transparency below 310 nm[78], meaning the primary peak of the mercury vapour discharge lamp would be absorbed by the material. Also noticed was that the mercury vapour discharge lamp had another peak at 184.9 nm[79]. The previously seen signal is therefore assumed to be either only possible with a sufficiently high intensity to penetrate through the Mylar and still reach the aluminium, as generated by the discharge of mercury vapour, or with the much higher energies of the second peak.

To proceed, a new, actually optically transparent, carrier material for the aluminium was needed, which, fortunately, was easily available in the form of the fused quartz window used previously. This fused quartz plate had a thin aluminium layer deposited on its surface using an old vapour deposition machine available at the Institute of Nuclear Physics, with a non-determinable thickness due to age and malfunction of the deposition machine. The plate can be seen in figure 4.35.

To enable serialization and control of the timing of the electron production, which is needed to calibrate drift times, a new setup was built with this fused quartz plate and an LED. A PCB powering the LED was mounted on top of a two-layer cathode, so that the fused quartz plate could be positioned between the LED and a hole in the cathode, through which the produced electrons could enter the detector. This assembly was then placed inside a prototype TPC[59], replacing its cathode, which can be seen in figures 4.36 and 4.37[77].

This more complicated setup, replacing the simple stretched aluminised Mylar foil, was necessary since the fused quartz plate itself could not serve as the cathode sur-

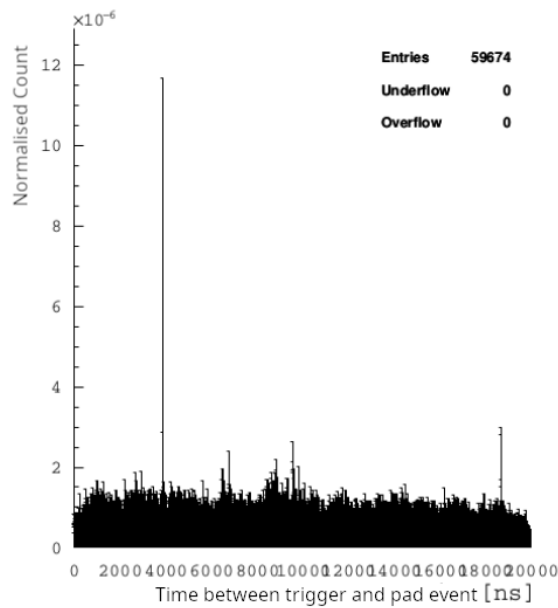


Figure 4.34: Coincidence plot between readout of the pad positioned below the LED, and the trigger signal for the light, normalised to the number of times the LED was triggered. The visible peak would imply a probability of less than 10^{-5} for each LED pulse to generate a detectable electron. Image from [77].

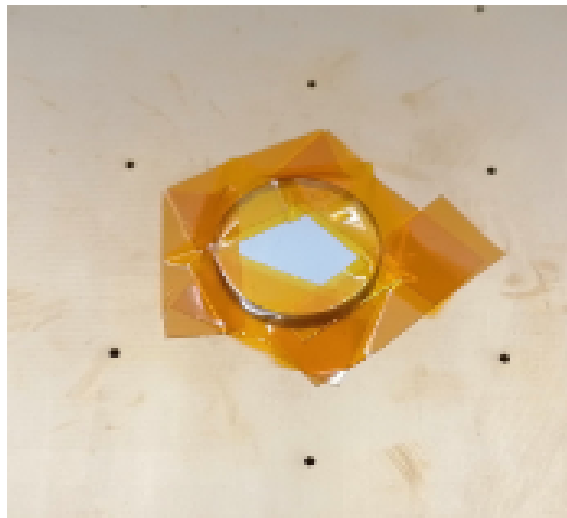


Figure 4.35: Fused quartz plate, deposited with an unknown thickness of aluminium, giving it the appearance of a mirror, attached to a copper plate with orange Kapton tape. Image from [77].

face, due to its limited size and extreme physical fragility. Simultaneously, however, the light intensity of the LED, which is directly correlated to the number of electrons produced and as such has to be preserved as much as possible, drops with the square of the distance between source and target. Unlike the high intensity light provided by the mercury vapour discharge lamp, the LED therefore has to be placed as close as possible to our cathode.

These two constraints introduce significant additional complexity. The PCB pow-

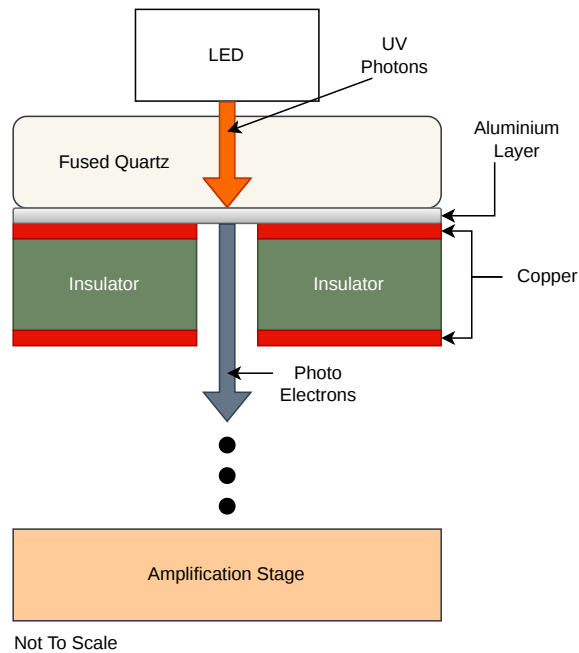


Figure 4.36: Schematic drawing of the basic Starry Night Concept, with a single LED.

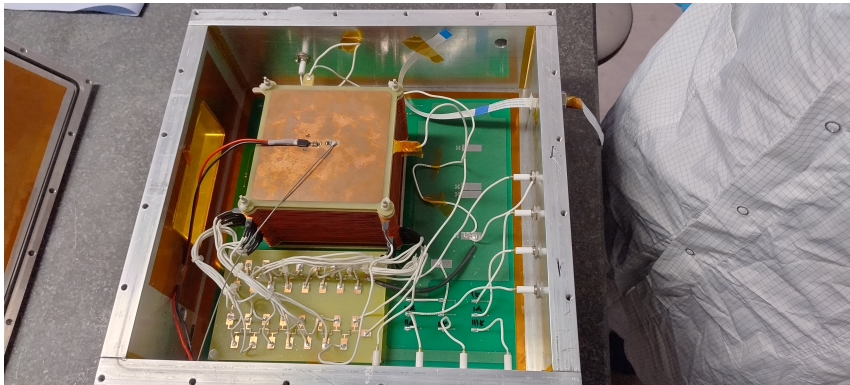


Figure 4.37: Photograph of the prototype TPC hosting the cathode and LED PCBs realising the concept of the image on the left, with the top ground plane of the LED PCB with the power and triggering cables visible.

ering the LED has to be kept at ground potential, while the cathode is intended to have a voltage of up to 20 kV applied. The fused quartz is therefore needed not just as an optically transparent substrate, but also as an electrical insulator. At the same time, the element supporting the fused quartz has to be a two-layered PCB, since a simple copper sheet, which has a uniform voltage applied, would create no potential difference at the surface of the aluminium, potentially reducing the extraction of photo-produced electrons from it. Also, without a drift field accelerating the produced electrons away, they have a high chance to recombine with the now positively charged surface, and would not be suitable for a drift time calibration. It is therefore necessary to apply a suction voltage between the two layers of the

cathode.

In this setup, it was possible to generate a signal for a couple of weeks after the deposition, an example of which can be seen in figure 4.38. Unfortunately, after those two weeks, the signal disappeared[77].

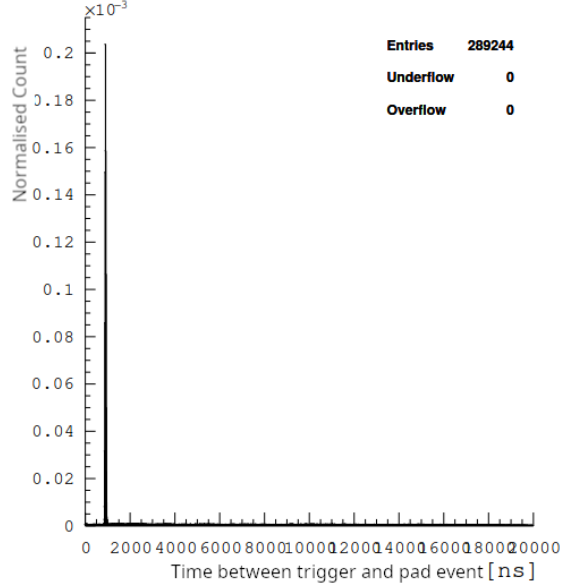


Figure 4.38: *Coincidence plot between readout of the pad positioned below the LED, and the trigger signal for the light, normalised to the number of times the LED was triggered. The visible peak only appears with an active LED and would give us an efficiency of about 10^{-2} for each LED pulse to generate a detectable electron. Image from [77].*

The reason for the disappearance of the signal is presumed to be the formation of a passivating layer of aluminium oxides and aluminium hydroxides, which occurs inevitably when aluminium is exposed to oxygen. The precise chemical makeup, crystal structure and thickness of the passivating layer cannot be easily determined. The passivating layer forms at the first contact of unoxidised aluminium with oxygen, but continues to grow after this point, in a complex chemical process involving the diffusion of oxidising agents through the existing crystal of oxides and hydroxides[80]. The diffusion of oxidisers into and thus thickening of the passivating layer is impacted by the environmental conditions of the surface - heat, pressure, oxygen and water presence - and the thickness and structure of the already present crystals. For aluminium, a critical point is reached at a thickness of 2-10 nm, depending on the previously mentioned parameters[81]. At this point, further diffusion is significantly hindered, halting further oxidation of the underlying substrate. This preservation of the underlying material is the origin of the denotation.

The optical and electrical properties of the passivating layer could not be determined with the tools available, but were presumed to be similar to that of amorphous alumina. Alumina, pure aluminium oxide Al_2O_3 , is transparent for the available wavelengths. However, the transmittance of a 5 nm thick layer exceeded 99.9%, only an insignificant amount of photons was absorbed and thus no electron production took place[82]. Simultaneously, alumina is also an often used electrical insulator, with a volume resistivity of $1 \times 10^{14} \Omega \text{ cm}$, which could play a role in suppressing

the effect of surface electric fields assisting in electron extraction.

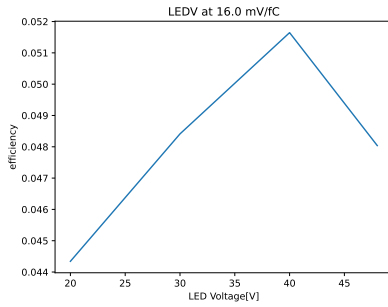


Figure 4.39: Measurement of the efficiency dependent on the LED voltage of a fused quartz plate deposited with 10 nm of tantalum, two weeks after deposition.

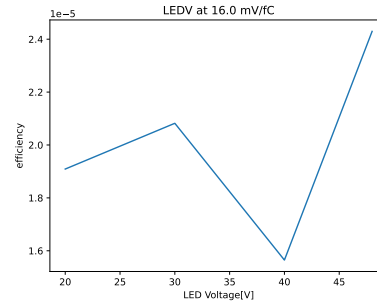


Figure 4.40: Measurement of the efficiency dependent on the LED voltage of a fused quartz plate deposited with 10 nm of titanium, two weeks after deposition. This image is scale by a factor of 10000.

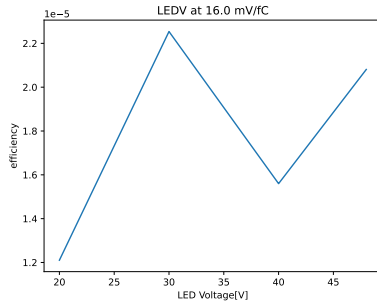


Figure 4.41: Measurement of the efficiency dependent on the LED voltage of a fused quartz plate deposited with 5 nm of titanium dioxide, two weeks after deposition. This image is scale by a factor of 10000.

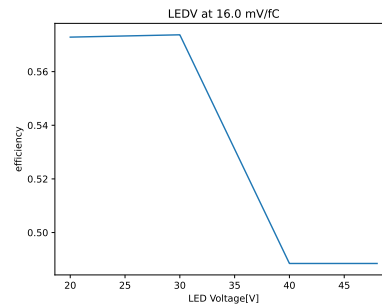


Figure 4.42: Measurement of the efficiency dependent on the LED voltage of a fused quartz plate deposited with 11 nm of aluminium, two weeks after deposition.

Constructing a well-functioning calibration system required finding the best configuration of material, LED and cathode construction, as well as a determination of the optimal level of both the suction voltage and LED voltage.

For the fused quartz plates, we tested two different thicknesses, 1 mm and 0.5 mm, limited above by the desire to have the smallest possible distance between LED and aluminium to maximise photon conversion, and limited below by mechanical tolerances. Fused quartz plates thinner than 0.5 mm cannot be manufactured with a sufficient tolerance to fit into our concept for electrical insulation and might leave gaps[83]. Plates of both thicknesses are fragile enough to be destroyed by careless handling, but 0.5 mm is robust enough to be deposited and installed, and such is the material chosen.

It was decided not to proceed with deposition in-house, since control of layer thickness was determined to be critical and could not be ensured with the existing deposition machine. Instead, deposition was outsourced to magtec coating solutions, which could deliver depositions with a thickness variation below 0.5 nm[84].

A variety of aluminium thicknesses, between 5 nm and 50 nm, and three alternative materials, titanium, titanium dioxide and tantalum, were tested.

The performance of the three alternate materials is shown in figures 4.39 to 4.42, which show the efficiency, the number of signals detected by our readout divided by the number of times the LED triggered, dependent on the voltage supplied to the LED. Both titanium and tantalum form a passivating layer and have work functions that lie around the 4.51 eV carried by 275 nm light, depending on their crystallographic orientation[85]. Titanium dioxide has a polymorph, rutile, with a work function of potentially as low as 4.3 eV. Unfortunately, none of these alternatives gave us better results than aluminium. Also important to note is the overall inconsistent behaviour, with higher LED voltages generally expected to always result in higher efficiencies due to generating a higher number of photons per pulse, which was not always the case during our measurements. The figures presented here are the highest stability achieved during tests.

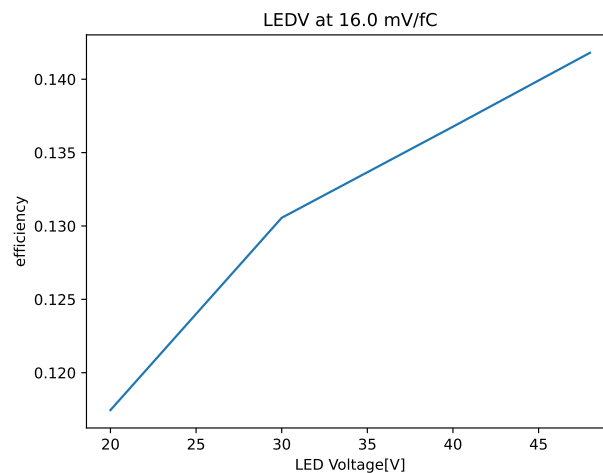


Figure 4.43: *Impact of LED Voltage on the efficiency of 11 nm aluminium, six months after deposition.*

The aluminium samples with thicknesses between 7 nm and 11 nm all performed similarly freshly after delivery, as shown in figure 4.42, while the 5 nm sample never delivered a signal and anything above 15 nm showed a signal during the first test, but not after a month.

Comparing equal thicknesses between two deliveries showed a significant degradation, as observed by comparing figure 4.42, 11 nm two weeks after deposition, and figure 4.43, the same thickness after six months. However, even this thickness, chosen because it performed best, still did not meet the requirements, especially due to still ongoing struggles to find conditions under which the aluminium performed predictably.

Attempts were made to remove the passivating layer that formed during transport, and then maintain the plates in a low oxygen environment, under the assumption that the then forming passivating layer would be thinner and therefore more conducive towards stability. To remove the first passivating layer formed during transport, the fused quartz plate was placed in a solution of nitric acid and iron-II nitrate, which only attacks aluminium oxide. While this succeeded in removing the aluminium oxide, the new passivating layer that formed immediately upon removal

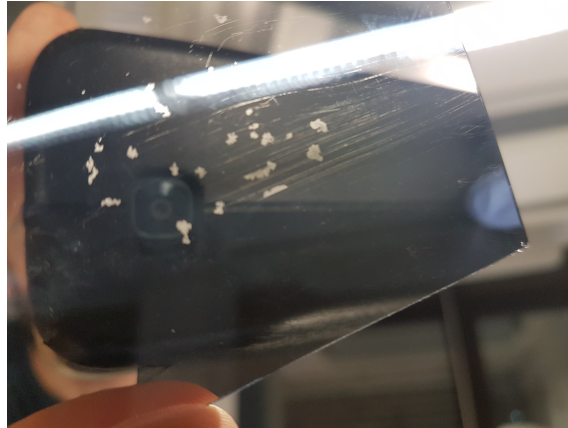


Figure 4.44: *Fused quartz plate after acid treatment. The white, non-reflective spots on the mirror surface are areas where the deposited material was removed entirely.*

from the solution reached all the way to the substrate, as shown by the white spots of pure alumina in figure 4.44.

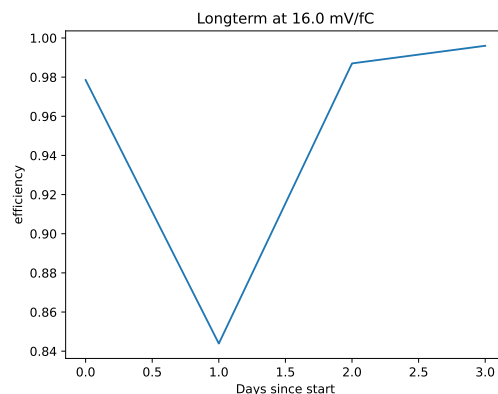


Figure 4.45: *Measurement of 11 nm thick aluminium, eight months after deposition, with constant LED voltage, over three days.*

After these methods failed, we chose to switch to a 255 nm wavelength LED[86]. This wavelength corresponds to a photon energy of 4.86 eV, which is potentially above the work function of the copper present in our TPC, which can be as low as 4.6 eV[87], depending on surface structure. With this lower wavelength, we were able to generate a long-term measurement, shown in figure 4.45, which demonstrated a varying but consistently high efficiency.

With the cathode construction now clear in principle, we could finish the design of Starry Night, which will be detailed in the following.

4.5.2 Designing a Starry Night

Based on the design developed in the previous section, of a single spot with one LED, a design for the whole active area to be illuminated with electrons was then developed. For this, the requirements on the calibration system and the physical and electrical limits of our LEDs and fused quartz had to be brought into alignment.

The number and position of the LEDs are determined by the competing interests of maximising the precision of the evaluation of the drift field and the cost and effort of trying to cover the whole area. All LEDs are placed so that they lie above an intersection between two readout pads on our anode. The edges of the cathode are equipped with LEDs with a dense interval of one LED on every fourth gap between pads, corresponding to 8 mm. This was not extended to the edge along the exit foil, where distortions are not as relevant or expected. That edge shares the same pattern as the interior, with one LED on every eighth gap between pads, corresponding to 16 mm. This pattern can be seen in figure 4.46.



Figure 4.46: CAD drawing of the Starry Night cathode, oriented with the top towards the spectrometer magnets, with blue showing the exposed copper on active area side and red that on the other. Visible in this red area as white dots is the hole pattern, with each hole having an LED positioned above it. Image from [88].

To power the LEDs in such a way that they release a short burst of light, a transistor-mediated discharging of three capacitors is employed. With a total of 1223 LEDs, a two-layered segmented control board is required to distribute power and control inputs to all of them individually. With this, a 3 ns pulse of sufficient intensity can be created at a rate of up to 1 kHz. Figures 4.47 and 4.48 show one individual stack and all 16 of them combined, respectively.

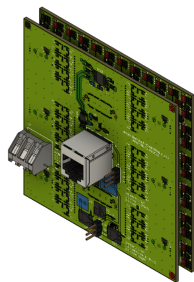


Figure 4.47: CAD drawing of the stacked LED and control PCB[88].

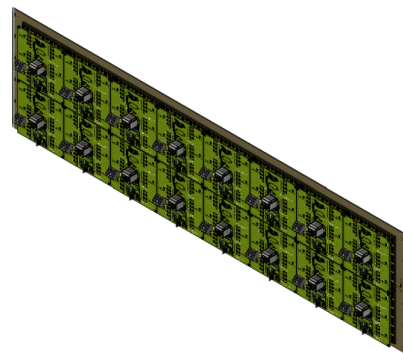


Figure 4.48: CAD drawing of the full 2×8 pattern of boards for Starry Night [88].

The LEDs directly touch the surface of the fused quartz plates, which in turn are in electrical contact with the upper layer of the cathode PCB. The cathode must be a two layered PCB instead of a copper plate with holes in it. A copper sheet of

sufficient thickness so it does not sag while spanning a distance of 800 mm would be too thick, even if supported along the span. No electric field of sufficient strength to extract free electrons from the aluminium surface could exist in the holes of such a copper plate. Instead, two layers of copper separated by an isolator allow the creation of a suction voltage above the voltage level of the cathode. This voltage at the top of the cathode is the fourth externally supplied voltage.

The electrically grounded LEDs are kept isolated from the high voltages of the cathode by the electrical impermeability of fused quartz. It is however complicated by the rigidity of the fused quartz and its low threshold for splintering when under tension. A light sacking, as might happen during installation of the 800 mm wide cathode, might put sufficient stress on some of the plates to damage them, if they were to be installed in such a way as to provide a continuous electrical isolation. This necessitates gaps between the plates to compensate for any potential mechanical action.

The scheme for the final design of Starry Night is shown in figure 4.49, evolved from the original design shown in figure 4.36 above.

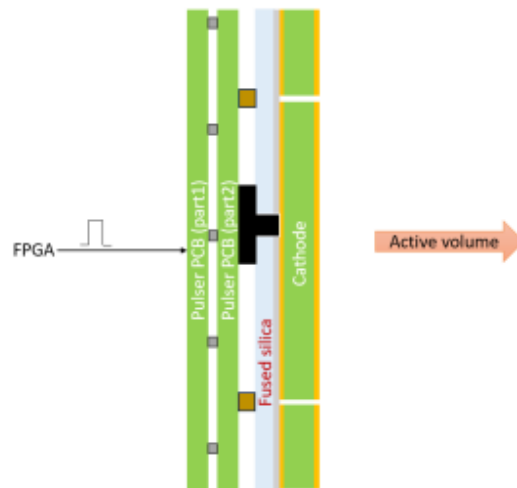


Figure 4.49: Schematic drawing of the concept for Starry Night. The two layers of the LED PCBs are externally supplied with a voltage of up to 48 V, charging up a bank of capacitors, and a trigger signal that opens a transistor allowing the charge from those capacitors to flow through the LED. The right-hand of the two boards (Pulsar PCB part 2) hosts the orange LEDs. The fused silica, deposited with aluminium, on which these LEDs rest are separated by black spacer to prevent damage. Image from [88].

The gaps between fused quartz plates are now filled by a 3D-printed frame that covers the whole upper side of the cathode. Into this frame, individual fused quartz plates are placed, which are connected by electrically conductive tape along the areas of the plates that are not in line between LEDs and holes.

For more information about the design of the electronics and mounting structure see the Master’s Thesis of Daniel Steger[88].

4.6 Software

For future use of this detector, it is necessary to both control the operation of the detector and its component systems, and to receive the information sent by the FECs. For these purposes, two pieces of software exist that are closely intertwined. All systems of MAGIX will be controlled with the **Experimental Physics and Industrial Control System**(EPICS)[89], and all detectors will send their information to an instance of the MiniDAQ.

4.6.1 Slow Control

EPICS is based on only two elements, the **Input Output Controllers**(IOC) and the **Channel Access Client**(CAC). IOCs manage communication with connected devices, keep the record of **Process Variables** (PV) associated with control and measurement values of those devices and participate in the channel access protocol. The channel access protocol is connecting the IOCs to the CACs, which receive input from automated processes or human operators, in such a way that any number of IOCs and CACs can be connected to a single EPICS network and any CACs can control a PV using only its name, without having to specify its host.

All experiments and the accelerator group at MESA use this system. It allows for easy communication of important information between the different parts of the facility.

4.6.2 Data Acquisition System

The **Data Acquisition**(DAQ) system in use at MAGIX is, unlike its Slow Control system, a wholly custom piece of software, currently still called by its prototype name MiniDAQ. MiniDAQ's main three functions are receiving, managing data files, and synchronizing initialisation and termination of data transmission from the detectors. For this, MiniDAQ is connected as a CAC to the EPICS system. MiniDAQ receives PVs telling it to send start and stop information to the detector systems, and makes information about file names and sizes of currently active data runs available to the channel access protocol.

MiniDAQ was independently developed for the Trigger Veto System and the TPC, and unified once the TVS and a prototype of the full TPC electronics could be installed together in the spectrometer hall. The development for the TPC extended MiniDAQ with the functionality of sending the VMM configuration data as well as the start and stop signal. This was required as it is both necessary to maintain a record of the configuration of the electronics associated with any measurement run, which is done using EPICS, and to send said configuration to the FECs faster than it is possible when extracting the full set of configuration information from EPICS when it is to be sent, since this requires several minutes.

For this, each configuration register, see tables 4.2 and 4.3, available to be managed for each of the 9 FECs and 72 hybrids per spectrometer, was assigned a PV, utilizing the MultiChannel Access extension to EPICS[20] to make it scalable. Each of these PVs informs MiniDAQ every time it is changed, and MiniDAQ maintains a dictionary of all PVs, which is loaded once on startup of MiniDAQ, shortening the time to configure and start all VMMs from two minutes to ten seconds.

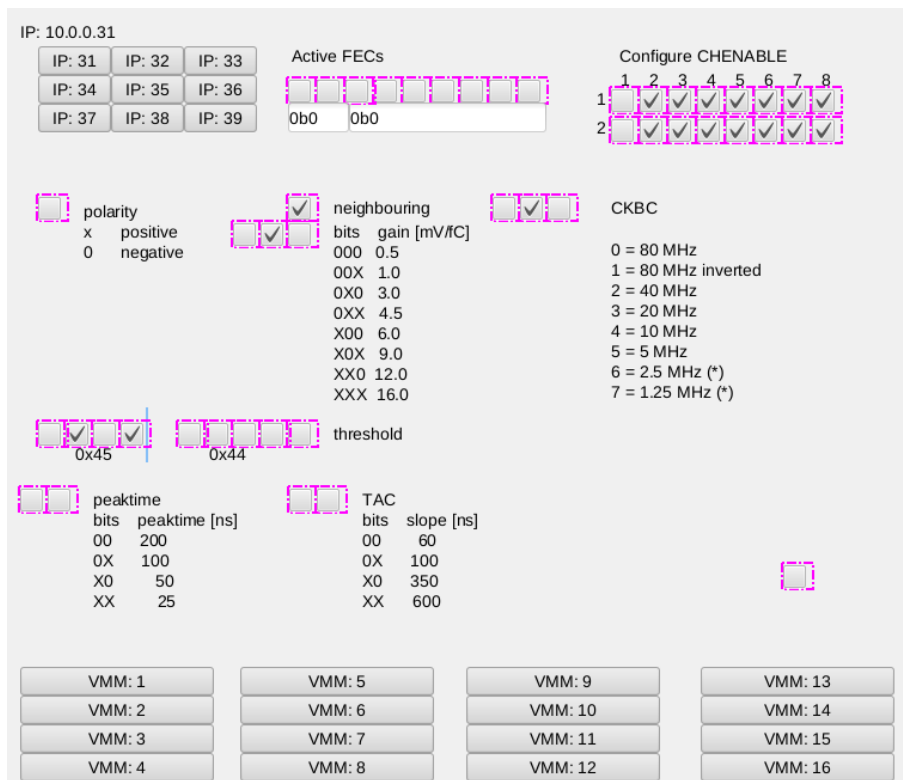


Figure 4.50: Phoebus interface showing selection of available FECs at the top left, control and current run information for MiniDAQ at the top right. At the bottom of the top image are shown the registers for each VMM channel of the selected VMM, with options to view the other 15 at the very bottom. The second image shows global configuration options per FEC.

The standard interface for human operators to EPICS is Phoebus, a CAC software for providing an easily accessible and modifiable graphical user interface. One example of such an interface, showing the screens for setting the calibration and managing

the DAQ, is given in figure 4.50.

4.7 Analysis

The data sent by the FECs, collated on the spectrometer servers and stored on the storage server, is analysed on the counting room PCs. This is done by first converting the raw binary file format into a ROOT tree[90], and then analysed with the help of multiple ROOT macros.

The program to convert a packet dump, as saved by MiniDAQ, into a ROOT tree, is named `vmm2root`. `vmm2root` first dissects the packet file into individual events and converts bit strings into information according to the structure shown in figure 4.24. Then the information is written into a ROOT tree and a global timestamp is assembled for each event. `vmm2root` is written to accept a live analysis script, which enables online monitoring of data as it is received.

This concludes the explanation of all individual components of the MAGIX TPC. The third and final chapter of this part will deal with the results that have already been achieved.

Chapter 5

Results

The first full scale MAGIX TPC has been completed, after a two year delay in the design, construction and delivery of the field cage PCBs. The two major modules, the amplification stage and Starry Night, were tested, and found to be performing as desired.

5.1 Amplification Stage

The amplification stage was tested in its transport container, shown in figure 5.1, which was originally to safely transport the GEM foils from the CERN workshop to Mainz. To turn it into a functioning particle detector, a copper sheet was glued into the box coplanar with the surface of the GEMs to form a TPC. With this setup, the full electronics setup was tested and minor problems eliminated.

With this setup, we were able to take cosmic data, measuring muon tracks. Figure 5.2 shows the best result of these initial measurements.

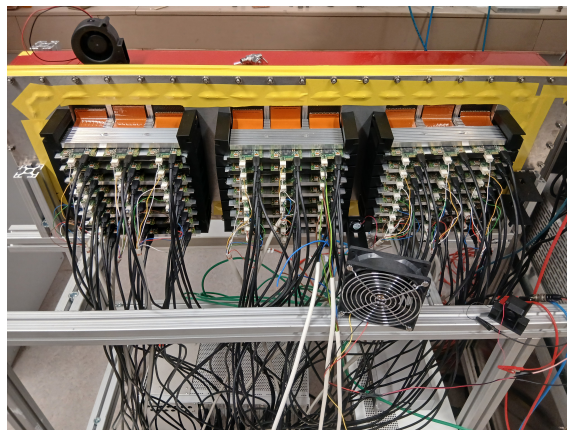


Figure 5.1: *The amplification stage connected to the red polyvinyl chloride transport box containing a copper sheet as cathode for testing purposes. Yellow tape is placed over the NS2 screws to achieve temporary gas tightness. In the front the 24 VMM hybrids and their cabling can be seen, as well as a temporary laboratory fan setup.*

These initial functional tests of the amplification stage were done without any field cage elements. Extending the view from the two-dimensional to the three-dimensional, as done in figure 5.3 with the inclusion of not just the hit map but also

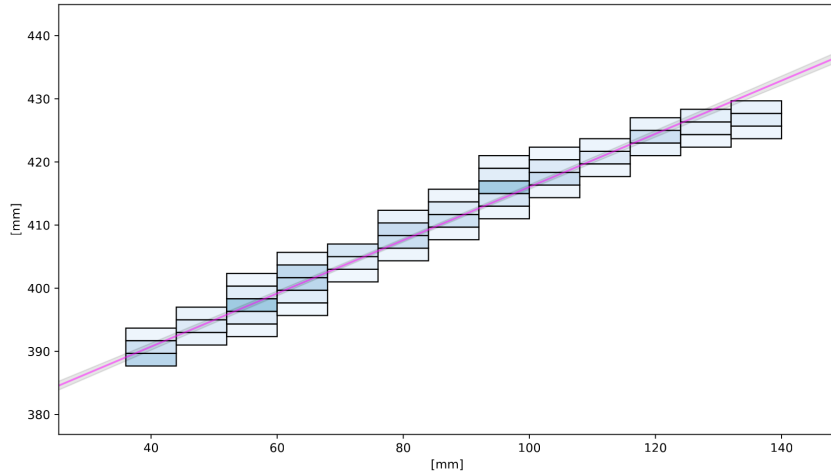


Figure 5.2: *Hitmap of a single cosmic muon on our readout plane, with signal intensity, corresponding to charge deposition, indicated by colour depth. A regression fit of the pads was performed and the resulting track over-layed. Over the 13 rows of the track, a multiplicity of five is reached in three. The top six and bottom five rows of the TPC did not generate a signal for this track.*

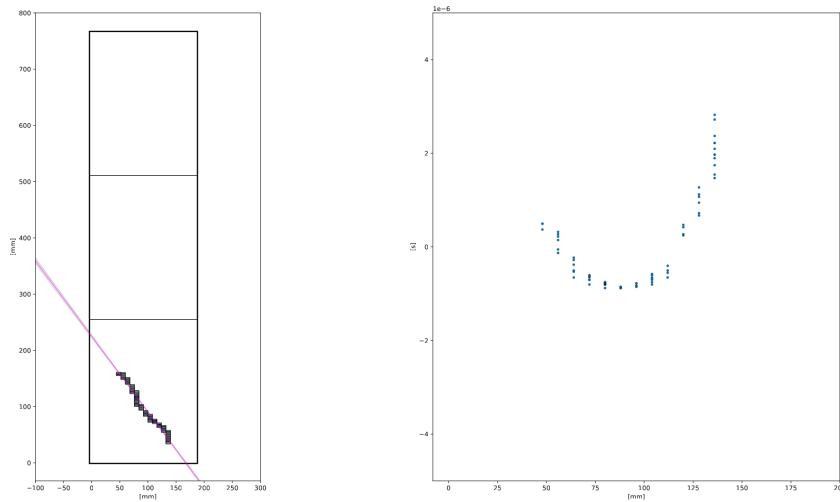


Figure 5.3: *Hit map of x and y-direction on the left and arrival time to y-direction plot on the right. Reducing the field strength on the outsides of the cathode led to increased drift time, distorting the arrival time plot.*

the arrival time to y-position plot, shows that the electric field distortions due to these missing elements increase the drift speed of electrons with increasing distance from the centre.

Looking at all identified tracks, shown in figure 5.4, it becomes apparent that the top and bottom five rows of the readout do not receive any signal that can be identified as belonging to a particle track. With this, the restricted length of the track in figure 5.2 becomes clear, where 13 out of an expected 24 rows created data.

The reason for this can be intuited from figure 5.3: the drift time over the ten most outlying rows is increased significantly, and reaches the point that the drift electrons become completely lost due to electron attachment. Nevertheless, the full

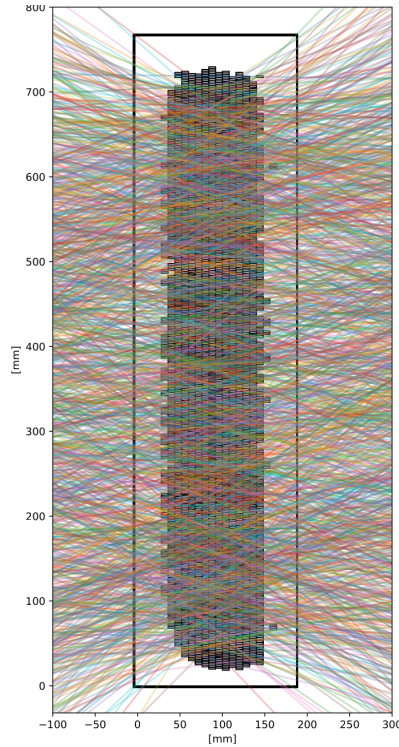


Figure 5.4: *All particle tracks captured during one run of the preliminary measurement, overlaying all pads contributing to those tracks. The black box containing the pads indicates the total size of the readout anode. The active pads are surrounded by a border of pads that do not receive a signal.*

illumination figure shows that the amplification stage is fully functioning. However, the identified deficiencies mean that no proper calibration or tuning of readout or amplification parameters is possible with this setup, and instead requires the construction of the full scale TPC, with both active area and field cage extension.

5.2 Starry Night

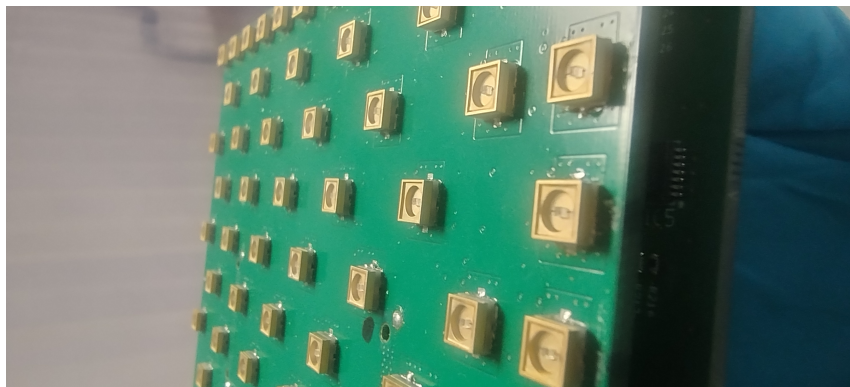


Figure 5.5: *LEDs on the surface of the first level PCB. Image from [91].*

The full version of the Starry Night calibration system is the only major module not yet completed, but is expected to be before the detectors are planned to be installed

in the spectrometers.

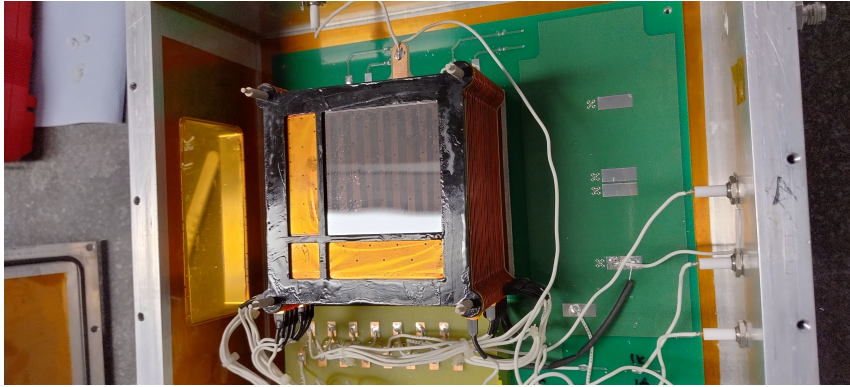


Figure 5.6: 3d printed black frame, with the large top right quadrant showing the fused quartz plate fixed in place with conductive tape in between rows of holes. Image from [91].

One of the Starry Night cells was tested and found to perform as required. For this test the PCBs of one module was equipped with a full set of LEDs, as seen in figure 5.5, and a one-off frame for the fused quartz plate was 3d-printed, shown in figure 5.6. This setup was then mounted in a prototype TPC[59] and its function tested. The LEDs were operated at 1 kHz with a pulse width of 10 ns.

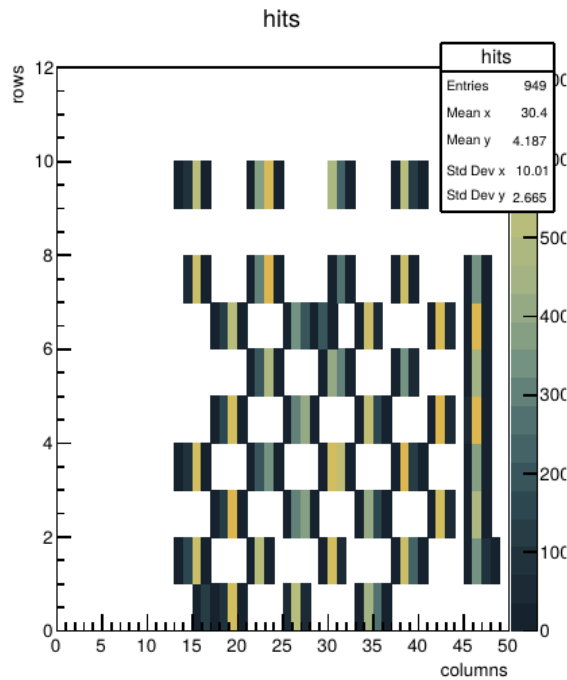


Figure 5.7: Hit map of the readout of the prototype TPC with the Starry Night module as cathode.

Figure 5.7 shows all LEDs are visible in the readout and figure 5.8 shows the temporal separation of the individual pulses.

With this demonstration of a fully functioning module, it only remains to construct the full 14 module Starry Night system, which is in progress and expected to complete before initial tests of the full detector system in the spectrometers.

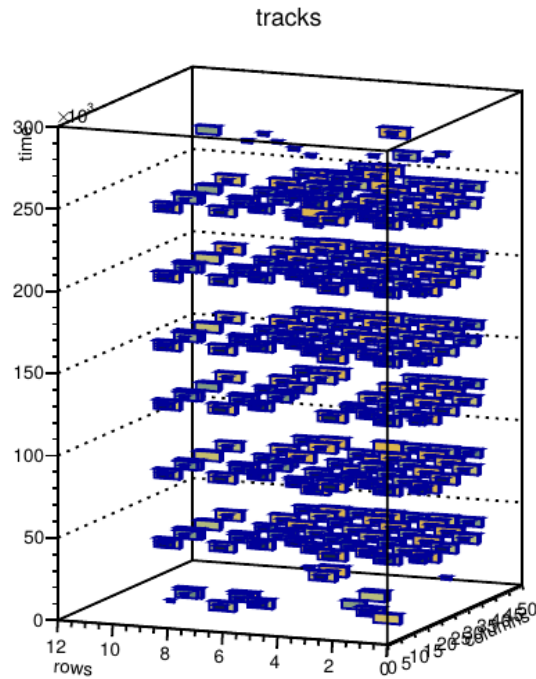


Figure 5.8: *Three-dimensional hit map, with the z axis showing the time of the readout event, and clear layers corresponding to LED pulses visible.*

5.3 Construction

After all components for the construction of the TPC active area had arrived, construction began in December 2025. At the end of January 2026, the first TPC active area was assembled, missing only the not yet arrived bridge PCBs.

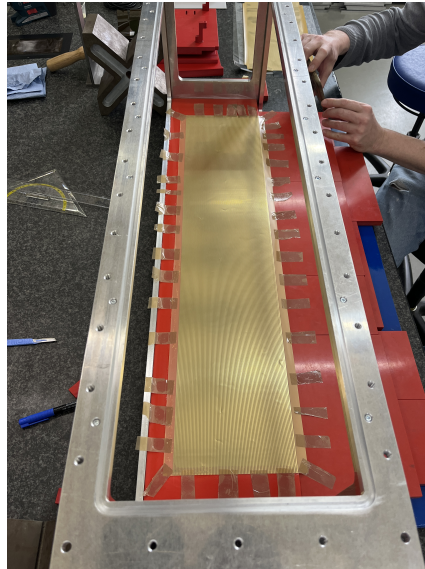


Figure 5.9: *Exit foil after being glued in and stretched by tape along its circumference. The tape is not applying a significant amount of force, merely enough to ensure the foil is fully stretched along its length and width and no folds that might cause problems in the future remain.*

The assembly began by installing the polyvinyl chloride elements holding the exit

foil. Then, the exit foil was glued in and stretched, as shown in figure 5.9. This stretching while being glued increases tension and thereby reduces the chance of plastic deformations under changes of mechanical load. Any such deformation impact the electrical properties of the exit foil.

Following that, the field cage PCBs were glued to the polyvinyl chloride isolator blocks, which were then mounted in the chamber, as shown in figure 4.10. With the field cage PCBs in place, the cables for their voltage dividers were connected to the high-voltage feed-throughs of the interface plates. During this process, the electrical properties of the PCBs and the ability of the assembled setup to maintain 20 kV were continuously tested. Points at which the voltage stability was being endangered, such as where isolated cables touched the bare metal of the frame, were corrected.

In place of the completed Starry Night system, an unequipped cathode PCB was mounted. The Starry Night frame was covered with a Kapton foil to achieve chamber closure in the absence of the components that would ordinarily rest there.



Figure 5.10: *Interior view from the direction of amplification stage into the interior of the active area. The two field cage PCBs on the side are glued onto the red polyvinyl chloride blocks behind them. The large vertical plate in the middle is the cathode, with the holes for Starry Night visible, though the Starry Night modules themselves are not yet installed. The horizontal surface is the exit foil, stretched and glued into the polyvinyl chloride frame.*

The completed frame, before the mounting of the amplification area, is shown in figure 5.10. The completed active area, after the mounting of the amplification area and in the process of being re-equipped with the readout electronics, is shown in figure 5.11.

The chamber will shortly begin operations and start taking cosmic ray measurements to test and optimise its performance.

For more information about the assembly of the first MAGIX TPC and for the results of its first tests, see the Master's Thesis of Lucie Bister[92].



Figure 5.11: *Front view of the completed TPC. The field cage extension it is connected to consists of only the frame, with no components installed. This is done to achieve gas tightness until the components of the extension can be installed. The yellow tape covering the NS2 screws from figure 5.1 has been removed, as those screws have been topped with glue.*

5.4 Conclusion

The initial tests of the amplification stage showed that our readout chain was fully functioning, but not yet reaching its full capability due to deficiencies of the temporary setup to test this amplification stage. No calibration or characterization could be done on it.

Starry Night has shown full functionality of a single module, meaning the full Starry Night setup requires only the work to complete 14 of them.

The first MAGIX TPC has been assembled and will soon begin its testing and calibration phase.

Part III

Preparing the Target, Software and Analysis for the first Measurement at MAGIX

Chapter 6

Preparing the Experimental Infrastructure for the first Measurement Run

Before MAGIX in general can begin taking data, all detectors need to be finished. Before a specific experiment can be run, a number of preparations have to be dealt with. In this part of my thesis I will detail some of the specific preparations that are necessary to run MAGIX's first measurement with an electron beam.

MAGIX will have to operate in the EB mode for this run, due the accelerator not being fully online yet. In EB mode, there is no need for a gas-jet target, and so, to spare the complexities of operating that target and to achieve a higher rate of data that can be used to calibrate our detectors, MAGIX will use a solid state target at first. During this initial operation, plentiful data will have to be taken to characterise and calibrate the detectors. It will also be used to perform a measurement of data relevant to few body and astrophysics, specifically the transition from factor from the ground state of carbon 12 into the excited Hoyle State.

6.1 Hoyle State

The formation of carbon 12 in stars takes place through the triple- α -process. During this process, two helium 4 nuclei combine to form the highly unstable beryllium 8, with a lifetime of 8.19×10^{-17} s. Before this isotope decays, a third helium nucleus has to be captured to form carbon 12. This only happens at extremely high temperatures, in excess of 10^8 K. Even then the observed amount of carbon 12 in the universe can only be explained if both capture reactions are favoured by having cross sections in excess of what would normally be expected of nuclear fusion reactions. Indeed, the mass of two helium 4 nuclei closely matches the mass of beryllium 8, but no such obvious correlation exists for the ground states of the participants of the second capture reaction. This lack led to the postulation[93] of the excited Hoyle State, shortly followed by its discovery four years later[94], with an excitation energy of 7.654 MeV. With this excitation energy, which lies only about 300 keV above the sum of the masses of beryllium 8 and an α -particle, the probability for that α -particle to fuse with a beryllium 8 nucleus is boosted by several orders of magnitude[95].

The Hoyle State has three decay end states. The first and most common is its

disintegration back into 3 α -particles. The other two are a transmission into the ground state carbon 12, by sequential emission of either two gamma particles, or an electron positron pair. To determine relative abundances, the combined decay width of these two radiative transmissions, Γ_{rad} , is crucial, as, at relevant temperatures, the reaction rate $r_{3\alpha}$ is influenced by it and two further factors:

$$r_{3\alpha} = \Gamma_{\text{rad}} \cdot \exp\left(-\frac{Q_{3\alpha}}{kT}\right). \quad (6.1)$$

The temperature T is given by the environment, and $Q_{3\alpha}$ is the energy released by the reaction. Γ_{rad} cannot be measured directly, and instead is determined as the product of three factors as:

$$\Gamma_{\text{rad}} = \Gamma_{\gamma} + \Gamma_{\pi} = \frac{\Gamma_{\gamma} + \Gamma_{\pi}}{\Gamma_{\text{total}}} \cdot \frac{\Gamma_{\text{total}}}{\Gamma_{\pi}} \cdot \Gamma_{\pi}. \quad (6.2)$$

One of those factors, Γ_{π} , the decay width of the pair emission decay, is the value of interest for MAGIX. Its more precise measurement is useful both for improving the precision of the $r_{3\alpha}$ value, as detailed above, and as a test of various few body physics theories.

Γ_{π} can be extracted from the cross section of inelastic electron scattering off carbon 12. For this, electron scattering data of the reaction $^{12}\text{C}(e, e')^{12}\text{C}^*$ has to be taken and its cross section extracted[96].

Before running any experiment to take such data the expected rate of signal events, and thus statistical error for a given run length, and signal-to-noise ratios, which are crucial for determining at which experimental settings it even makes sense to run, have to be determined.

6.2 Signal Rates for Electron Scattering

When accelerated electrons hit a nuclear target of mass M_T and scatter, they do so with an initial energy E_i , a final energy E_f and under an angle $\Omega = (\Phi, \Theta)$. The number of electrons n subsequently detected during an experiment of duration T under a solid angle $\Delta\Omega$ depends on multiple factors and can be expressed as:

$$n = \int_{\Delta\Omega} \int_T \frac{d\sigma}{d\Omega}(\Phi, \Theta) \cdot A(\Theta, E_f, t) L(t) d\Omega dt. \quad (6.3)$$

The three major variables here are the acceptance A , which depends on the particularity of the detector setup, the luminosity L , which is determined by the properties of the beam and target, and the cross section $\frac{d\sigma}{d\Omega}(\Phi, \Theta)$, which contains all information about the nuclear interaction.

The detector acceptance in our case is given by the spectrometer angular and momentum acceptance. Since our spectrometers can be rotated and have their central momentum varied, the acceptance has to be calculated for a given experimental setting.

The luminosity L for a fixed target experiment is defined as:

$$\begin{aligned}
L &= \text{Particles of Beam per unit of time} \times \text{Target Particles per Area} \\
&= \frac{I(t, x, y) \cdot \varrho \cdot l(x, y) \cdot N_A}{e \cdot A_u},
\end{aligned} \tag{6.4}$$

with the beam current $I(t, x, y)$, which is a distribution of electrons arriving across the surface of the target varying with time, the target density $\varrho(x, y)$, the length of the target in direction of beam $l(x, y)$, which is not uniform across the target's surface, Avogadro's number N_A , the elementary charge e and A_u , the atomic weight of the target molecules. ϱ and l are often combined into the areal density ϱ_A .

The cross sections, which contain the desired information about the physics of the investigated target, are often known approximately and can be inferred from existing data, but vary with scattering angle.

The complexity and interrelatedness of these factors means that an analytical solution to equation 6.3 cannot be found, and instead a numerical solution method for solving the integral has to be employed.

The following three chapters will detail how the luminosity of our experiment and the cross section of our interaction will be calculated and how these elements are combined to produce our rate expectations. The final chapter will then show the results of these calculations and give initial values for the experimental settings to be used.

Chapter 7

Determining the Target Areal Thickness of the Diamond Target

The luminosity of our experiment, as given by equation 6.4, depends on two variables, the beam intensity and the target areal density. Of these two variables, beam intensity is determined by the accelerator and measured along the path of the electron through it, while the areal density is determined and has to be measured by the experiment itself.

The alternative to determining the luminosity from these component variables is running two simultaneous measurements, one observing the reaction of interest, with a cross section to be determined, and the other a reaction with a well known cross section. For the case of a measurement of the Hoyle State, the luminosity monitor would be the elastic scattering of the ground state. With our momentum acceptance and at our energies, we can measure the scattering off the ground and excited state with one spectrometer. However, an absolute determination of the luminosity remains desirable and is intended for our experiment.

7.1 Choosing a Target

Looking again at equation 6.4, some difficulties with an absolute luminosity determination become apparent. A beam of accelerated electrons is not a static object, always running along the same lines with a homogeneous intensity. A real electron beam has, when viewed in slices along its path, a constantly varying distribution of velocities and positions orthogonal to that path. Only its volume in the four dimensional phase space spanned by those variables remains constant[25].

On average, the beam intensity can be described by a time-dependent electron density distribution that has to be measured and whose variance has to be taken into account when calculating the luminosity. The design goal for MAGIX is, as mentioned in section 2.1, for the beam spot to be Gaussian distributed in both directions, with a standard deviation of 100 μm , and with a beam current that will be measured to a precision of 0.1%

Turning to the factor that is in the hand of MAGIX, the target areal density, the product of ρ and l , has to be measured with a precision of around 1%. The design areal density of this target is restricted from below by the runtime allotted to the experiment. An insufficient areal density leads to unfeasibly low luminosities. The design areal density is restricted from above by multiple scattering induced back-

ground and resolution loss. For this experiment at MAGIX we aim for an areal density of 6.5 mg cm^{-2} , based on past experiments[97].

Indeed, MAGIX has already some experience with measuring the areal density of its gas-jet target[31].

However, a problem arises now, as carbon cannot be used as a pure gas in the gas-jet target, as it is a solid at the required temperatures, and in any case, a calibration run ideally uses a solid target to minimise potential issues and minimise the variance of the produced calibration data. Therefore, the Hoyle State measurement will alternatively utilize a solid target, as mentioned in section 2.2.5 and at the beginning of this part.

Pure carbon is, due to its malleable nature, available in a number of possible allotropes, ranging from the familiar graphite to the exotic Buckminsterfullerene. In the interest of both cost and feasibility, a reasonable choice for nuclear scattering experiments is pyrolytic graphite. Pyrolytic graphite achieves purities in excess of 99.999%, though not isotopically pure, and has sufficient material strength to be shaped into thin foils[98], which are an ideal shape when planning to use it as a target for electron scattering. The target has to be thin by necessity, to achieve our desired areal density, and flat enough to provide a sufficiently large area for the beam spot to be situated entirely on it, without any part of the beam having to interact with the support structure for the target.

Pyrolytic graphite sheets are not available with a native thickness variability below our requirements and are therefore not immediately useable. Measuring the average thickness of a foil by determining its weight and surface dimensions is possible to sufficient precision, but the surface roughness of pyrolytic graphite means that it is not given that the area hit by the beam spot has the average thickness of the whole foil.

A carbon allotrope with superior surface roughness, greater mechanical stability and affordable price has recently become available in the form of diamond created through chemical vapour deposition. Additionally, as diamond is optically transparent, it is possible to use Mach Zehnder Interferometry to determine the thickness of a diamond plate across its whole surface. With such a measurement and with a precise determination of the position of the beam spot, it becomes possible to determine the absolute luminosity of our experiment with sufficient precision.

In the rest of this chapter Mach Zehnder Interferometers will be discussed. It will be explained how to use a continuous wavelet transform using Morlet Wavelets to extract thickness information from the fringe pattern delivered by this Interferometer and the results of this extraction will be presented.

7.2 Mach Zehnder Interferometers

Mach Zehnder Interferometers were developed independently by Ludwig Zehnder in 1891[99] and Ludwig Mach in 1892[100]. They consist of a light source that creates coherent light takes two different paths to a detector, where it generates an interference pattern based on the phase shift between the two paths. For this, the original beam is first split in two and each of the two new beams gets reflected by a mirror. One of the beams travels through a sample of interest and then both beams are merged again, with the combined output being measured. A schematic drawing of this concept is shown in figure 7.1.

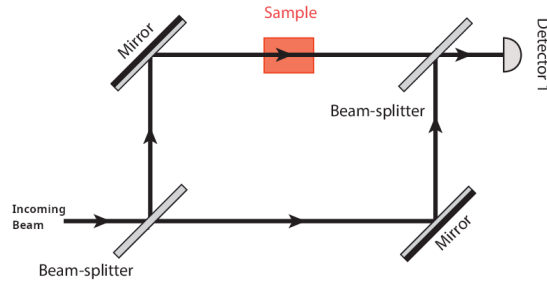


Figure 7.1: Schematic drawing of a Mach Zehnder Interferometer, with the laser source on the bottom left, two beam splitters - mirrors with a 50% reflectivity, so that the incoming beam is half reflected and half transmitted - two mirrors and a detector on the upper right. Slightly modified image from [101].

The phase difference δ creating the interference pattern is determined only from the difference in *optical* path lengths between the two paths, $d_1 - d_2$ and the wavelength λ of the light used and is given by

$$\delta = 2\pi \frac{d_1 - d_2}{\lambda}. \quad (7.1)$$

To determine the thickness of a sample, the interferometer is calibrated by moving the beam splitters and mirrors so that without a sample a regular interference pattern is created. A measurement of this interference pattern of the empty path is then taken. After that, the sample is introduced into the beam and another measurement of the new interference pattern thus created is taken. With that the thickness l of a sample with refractive index n can be determined for any point at which the phase is known as:

$$l = \frac{(\delta_{sample} - \delta_{empty})}{2\pi} \frac{\lambda}{n - 1}. \quad (7.2)$$

Diamond is an optically transparent material, with a refractive index of 2.4105 at a wavelength of 632.8 nm[102], the centre wavelength of a helium-neon laser.

Such an interferometer was set up, which can be seen in figure 7.2. Measured was a diamond plate of 12 mm by 12 mm, where 1 mm on all four sides of the diamond plate is glued onto a silicon substrate as mechanical support, which can be seen in figure 7.4. Also visible in that image is a measurement of the thickness. According to that measurement, the plate had a thickness varying between 12.1 and 12.8 μm .

This manufacturer provided measurement has insufficient accuracy and point resolution to achieve our desired areal thickness resolution, since only this image is available and most information about the measurement setup is not.

As detector for our interferometry, we used a DCMC900, a high resolution camera with a pixel count of 3488 x 2616. One such image is shown in figure 7.5.

These images now have to be digitally processed to extract the phase information at each location corresponding to a pixel. To do this, the information has to be moved from the space domain into the frequency domain, utilizing a more complex version of a Fourier transformation, the continuous wavelet transformation.

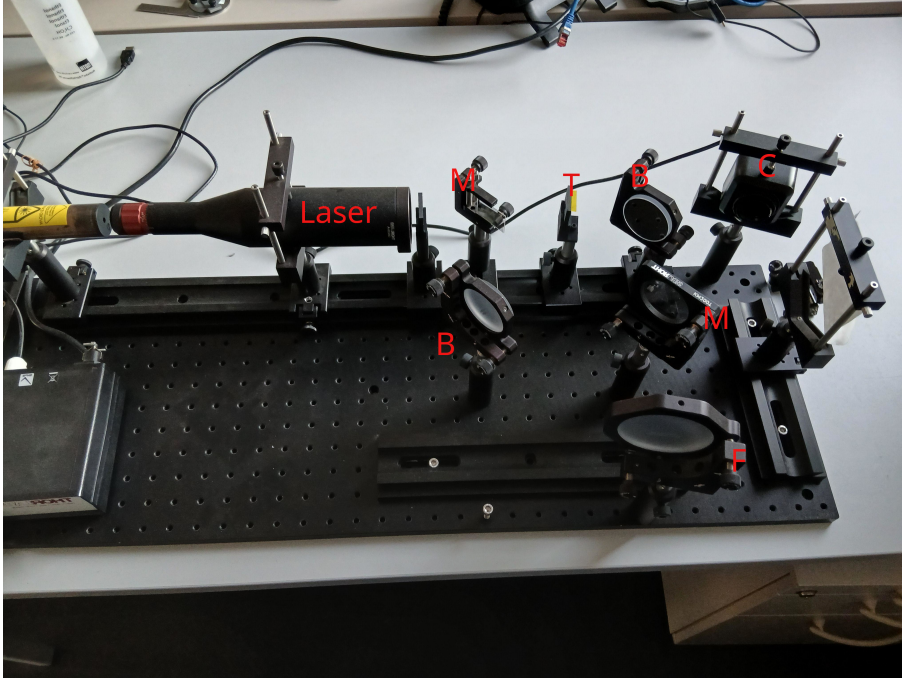


Figure 7.2: *An image of our interferometer setup. To the very left we have our 632.8 nm wavelength laser, with a defocusing assembly, labelled Laser. To the right is the interferometry setup, with two beam splitter labelled B, two mirrors labelled M and our diamond target to be tested labelled T. The diamond target can be seen in more detail in figure 7.3. In place of the detector of figure 7.1 we have a focusing lens labelled F, which has a high resolution camera, labelled C, in its focus. The spread of the beam by the defocusing assembly is calibrated so that the target is illuminated by a beam spot of equal intensity across its surface.*

7.3 Continuous Wavelet Transformation

A continuous wavelet transformation functions like a Fourier transformation which does not compare the input function to complex exponents to extract frequency information for the entire input at once. Instead, a continuous wavelet transformation compares the input sequence with a series of wavelet packets of varying frequency, transforming the one dimensional input into an overdetermined two-dimensional output. With this over-determination the extraction of the phase corresponding to the correct frequency is trivialised.

A continuous wavelet transformation is defined as

$$X_w(a, b) = \frac{1}{|a|^{1/2}} \int_{-\infty}^{\infty} x(t) \bar{\psi} \left(\frac{t-b}{a} \right) dt, \quad (7.3)$$

where $x(t)$ is the one dimensional intensity, for our case one row of pixels of our measurement, $X_w(a, b)$ is the signal in the frequency domain, $\bar{\psi}(c)$ is the complex conjugate of the mother wavelet that is continuous in both domains and a is a scaling factor. The mother wavelet for this use case is a non normalised, since we only care about the phase, Morlet Wavelet, which is defined as

$$\Psi_{\sigma}(t) = e^{-\frac{1}{2}t^2} \left(e^{i\sigma t} - e^{-\frac{1}{2}\sigma^2} \right), \quad (7.4)$$



Figure 7.3: *Photograph of the diamond plate, mounted in a 3D printed support structure for measurements in the interferometer.*



Figure 7.4: *Diamond Plate measured in thin-film interference setup by the manufacturer Diamond Materials. The lines are an interference pattern generated by testing equipment of the manufacturer and show the surface topology with 130 nm thickness variation between each ridge. Variance between these points is unknown and as such this measurement itself is insufficient to reach our desired degree of precision.*

with the admissibility criterion σ , which governs the resolution trade off between the time and frequency domain.

This transformation is now applied to each row of the image to be processed, which generates a frequency and phase matrix, a representative of which can be seen in

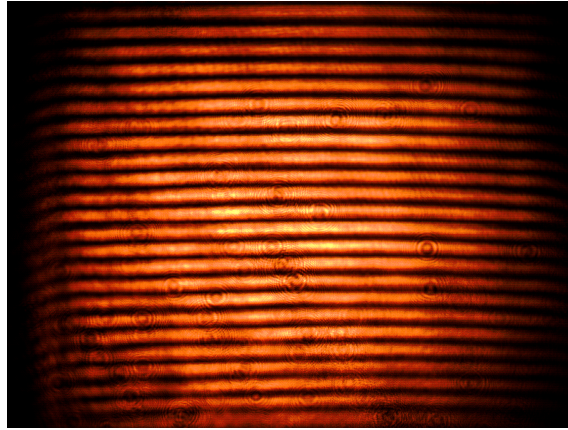


Figure 7.5: *High Definition image of interference pattern generated by camera C in figure 7.1.*

figure 7.6. The frequency of the interference pattern is visible as the white band. The phase of the interference pattern can now be extracted from the phase matrix at the position of the maximum frequency of the frequency matrix of each pixel.

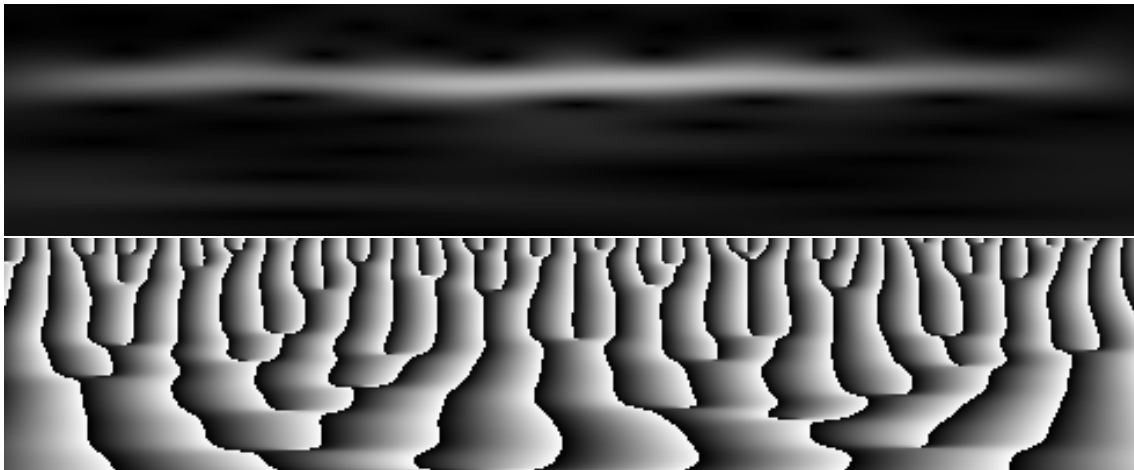


Figure 7.6: *The frequency and phase matrix, visualised as images, of one line of the original image transformed with a continuous wave. The x-axis of the image corresponds to the width of the original image, corresponding to the transformation of one row of pixels.*

Figures 7.7 and 7.8 show the result of a complete transformation and phase extraction for a measurement without sample.

7.4 Results

Forming the difference between images 7.8 and 7.9, accounting for the 2π periodicity of the phase by assuming continuity and applying equation 7.2 for all points yields a thickness distribution of the diamond plate, which can be seen in figure 7.10. Comparing this to the existing characterization from the manufacturer, the same topology can be recognized, with differences in measured thickness accounted for by differing precision.

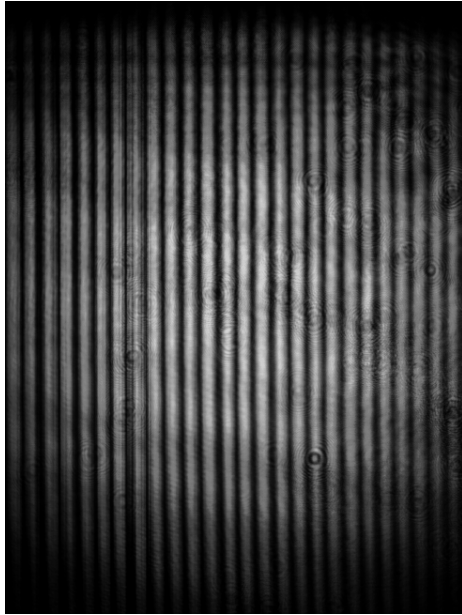


Figure 7.7: *Measurement without sample, rescaled and flipped as preparation for transformation.*

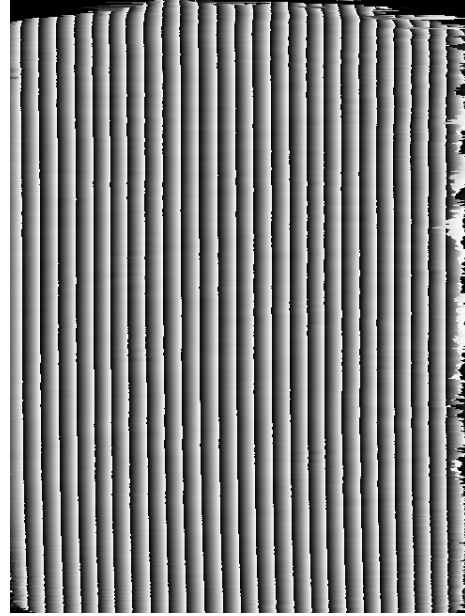


Figure 7.8: *Phase extracted from image to the left.*

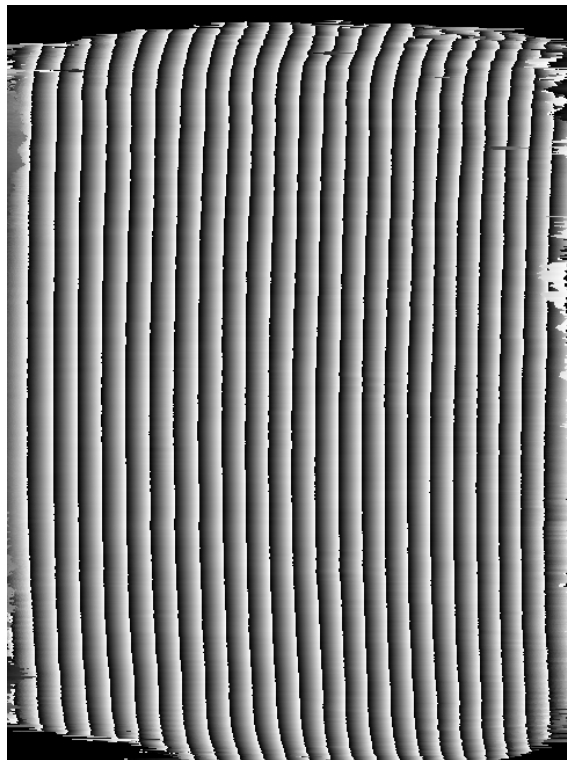


Figure 7.9: *Phase extracted from image 7.5, with diamond plate in beam path.*

The error of this measurement is given by the quantization of the interference pattern and any potential systematic errors. Estimating based on resolution that our measurement of the interference pattern can identify a change in phase of $\frac{2\pi}{8}$, and with a wavelength of 632.8 nm, our assumed error for this measurement is 60 nm, a relative error of about 0.5%.

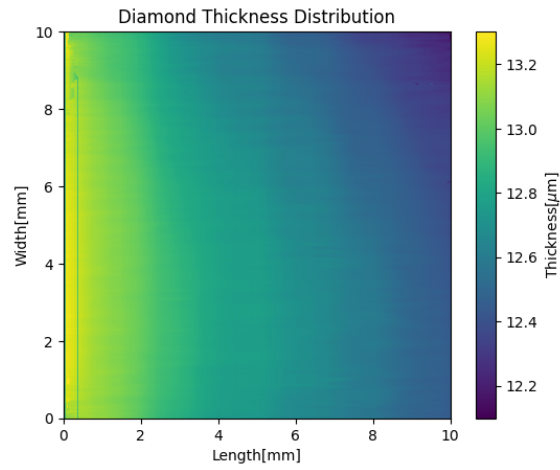


Figure 7.10: *Thickness distribution extracted from the interference pattern generated by the Mach Zehnder Interferometer extracted by a continuous wavelet transform utilizing a Morlet Wavelet.*

Now that the target is chosen and characterized, the following chapter will detail the basis of how the cross section for our experiment has to be calculated.

Chapter 8

Electron Scattering Cross Sections

The cross section for our experiment can be calculated in a number of ways, two of which are immediately relevant. The first is by calculating the expected cross section from known properties of the nucleus, such as its charge distribution, utilizing known theories, and the second is by interpolating between existing measurements. In the following chapter, the background for both of these calculations will be given.

8.1 Electron Scattering

Cross sections are the core of nuclear physics and for our case are derived using time-dependent perturbation theory. Figure 8.1 shows the Feynman diagram of the first order of the electron scattering interaction that we will be using to investigate the Hoyle state.

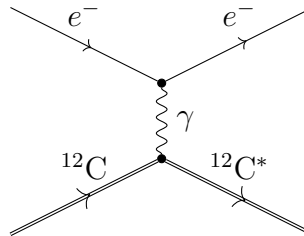


Figure 8.1: *Inelastic Electron Nucleus Scattering, where the carbon 12, indicated by the ^{12}C arrow, remains behind in an excited state, such as the Hoyle State.*

This interaction has one kinematic degree of freedom, which is most often expressed in the momentum transfer q^2 , given by

$$q^2 = -\frac{1}{(\hbar c)^2} 4(E_i E_f) \sin^2 \Theta/2, \quad (8.1)$$

with the initial energy of the electron E_i , the scattering angle Θ , c the speed of light and \hbar the reduced Planck constant.

The final energy of the scattered electron E_f for elastic scattering is given by

$$E_f = E_i + \frac{q^2}{2M_T}, \quad (8.2)$$

with the mass of the target nucleus M_T .

If the electron loses some energy E_x to excitation of the nucleus, as in the case of the 7.654 MeV required to excite the carbon 12 nucleus into the Hoyle State, the final energy equation expands into:

$$E_f = E_i + \frac{q^2 - 2M_T E_x - E_x^2}{2M_T}. \quad (8.3)$$

The cross section of the interaction is given by three components: the cross section of an electron scattering off a point source with nuclear charge Z , i.e. the Mott cross section

$$\left(\frac{d\sigma}{d\Omega}\right)_{\text{Mott}} = \left(\frac{Z\alpha}{2E_i}\right)^2 \frac{\cos^2 \frac{\Theta}{2}}{\sin^4 \frac{\Theta}{2}}, \quad (8.4)$$

the recoil factor that accounts for the energy transferred to the nucleus

$$f_{\text{rec}} = \left(1 + \frac{2E_i \sin^2 \frac{\Theta}{2}}{M_T c^2}\right)^{-1}, \quad (8.5)$$

and the form factors, which contain all information about the structure of the nucleus and its excited state. It is from these form factors that our value of interest, Γ_π , can be extracted. For a non polarised beam, the form factors of a given reaction vary only with the momentum transfer.

8.2 Form Factors

The following discussion of the treatment of inelastic nuclear scattering follows J. Heisenberg in *Advances in Nuclear Physics* Volume 12 unless otherwise specified[103].

This dependency arises because the form factors are the Fourier Bessel transforms into the momentum transfer space of the nuclear charge and current densities. $|F_L^C(q)|$, $|F_L^E(q)|$ and $|F_L^M(q)|$ are the Coulomb, electric and magnetic form factors, respectively, depending on L , the spin quantum number of the nucleus, and are defined as:

$$F_L^C(q) = \frac{\hat{J}_f}{\hat{J}_i} \int_0^\infty \varrho_L(r) j_L(qr) r^2 dr \quad (8.6)$$

$$F_L^E(q) = \frac{\hat{J}_f}{\hat{J}_i} \left[\int_0^\infty (L+1)^{1/2} J_{L,L-1}(r) j_{L-1}(qr) r^2 dr \right. \\ \left. + \int_0^\infty L^{1/2} J_{L,L+1}(r) j_{L+1}(qr) r^2 dr \right] \quad (8.7)$$

$$F_L^M(q) = \frac{\hat{J}_f}{\hat{J}_i} \int_0^\infty J_{L,L}(r) j_L(qr) r^2 dr. \quad (8.8)$$

J_i and J_f are the initial and final spin nuclear state. $j_L(qr)$ denotes the spherical Bessel functions of order L . $\varrho_L(r)$ is the radial function of the nuclear charge density, which is normalised to the nuclear charge Z . $J_{L,L}(r)$, $J_{L,L-1}(r)$ and $J_{L,L+1}(r)$ are the radial functions describing the nuclear currents. These radial functions can be

written as the reduced matrix elements of the nuclear charge ϱ^{op} and nuclear current operator J^{op} between the initial spin state J_i and final spin state J_f as:

$$\langle \Psi_f | \varrho^{\text{op}} | \Psi_i \rangle = \sum_{LM} \langle J_i M_i L M | J_f M_f \rangle \varrho_{L_i}(r_N) Y_L^{M*}(\hat{r}_N) \quad (8.9)$$

$$\begin{aligned} \langle \Psi_f | J^{\text{op}} | \Psi_i \rangle = & \sum_{LM} \langle J_i M_i L M | J_f M_f \rangle \left[J_{L,L-1}(r_N) Y_{L,L-1}^{M*}(\hat{r}_N) \right. \\ & \left. + J_{L,L+1}(r_N) Y_{L,L+1}^{M*}(\hat{r}_N) + J_{L,L}(r_N) Y_{L,L}^{M*}(\hat{r}_N) \right], \end{aligned} \quad (8.10)$$

with the nuclear spin quantum numbers L and M , the distance from the centre of mass r_N , and the spherical harmonic function $Y_{L,L}^{M*}$. The actual calculation of these reduced matrix elements based on a chosen model contains all complexities of nuclear structure and can be compared to experimental results to validate the model given by few body theories.

For a generic case of an electron scattering inelastically, using the Plain Wave Born Approximation of the interaction taking place with only a single photon, as well as neglecting the electron mass. This means that the whole cross section can be expressed as[103]:

$$\frac{d\sigma}{d\Omega} = \left(\frac{d\sigma}{d\Omega} \right)_{\text{Mott}} f_{\text{rec}} \left\{ \sum_{L \geq 0} |F_L^C(q)|^2 + \left(\frac{1}{2} + \tan^2 \frac{\Theta}{2} \right) \times \sum_{L \geq 1} [|F_L^E(q)|^2 + |F_L^M(q)|^2] \right\}. \quad (8.11)$$

For the specific case of an electron scattering off a carbon 12 atom, exciting it to the Hoyle State in the process, a monopole transition between two 0^+ states, the cross section simplifies to[104]:

$$\left(\frac{d\sigma}{d\Omega} \right)_{\text{C}_0} = \left(\frac{Ze^2}{E_i} \right)^2 f_{\text{rec}} \left[\frac{1 + \cos \Theta}{2 \left(1 + \frac{E_x^2}{2E_i(E_i - E_x)} - \cos \Theta \right)^2} \cdot |F_0^C(q)|^2 \right]. \quad (8.12)$$

To get from this cross section to the decay width Γ_π , the reduced transition probability is calculated as[104]:

$$4\pi B_0^C(q) = Z^2 |F_0^C(q)|^2. \quad (8.13)$$

From this reduced transition probability, an expansion of the spherical Bessel function allows the extraction of the monopole matrix element ME as[97]:

$$\sqrt{4\pi B_0^C(q)} = \frac{q^2}{6} (\text{ME}) \left[1 - \frac{q^2}{20} R_{tr}^2 + \frac{q^4}{840} \frac{\langle r^6 \rangle_{tr}}{\langle r^2 \rangle_{tr}} - \frac{q^6}{60480} \frac{\langle r^8 \rangle_{tr}}{\langle r^2 \rangle_{tr}} + \dots \right]. \quad (8.14)$$

Here, this monopole matrix element can now be used to calculate the decay width as[97]:

$$\Gamma_\pi^Z = C(Z, E_x) \frac{8\alpha^2 B(E_x)}{27\pi (\hbar c)^4} \left(\frac{1}{2} E_x - m_e c^2 \right)^3 \left(\frac{1}{2} E_x + m_e c^2 \right)^2 (\text{ME})^2. \quad (8.15)$$

α is the fine structure constant and $C(Z, E_x)$ and $B(E_x)$ are correction functions for the transition width and the electric field, which can be calculated numerically[105].

The decay width is therefore the product of a long chain of calculations all ultimately deriving from a measurement of the number of electrons scattered at a certain angle and energy, which also yields additional information about the nuclear charge and current densities of the nucleus.

To achieve precision of this measurement for both of these purposes however requires consideration of processes higher than the first order one given in figure 8.1. Besides initial and final state radiative corrections of the interacting particles, which are universally applicable for electron scattering experiments and which can be corrected for with known analytical formulas[106], the Hoyle State measurement in the intended energy range has the additional challenge that the Plain Wave Born Approximation, on the basis of which equation 8.11 is written, no longer holds to sufficient precision.

8.3 Distorted Wave Born Approximation

The Plain Wave Born Approximation used above for equations 8.11 and 8.12 assumes only a single photon is exchanged. This photon then carries the whole of the exchanged momentum, which equivalently means that the incoming electron does not see the electric field of the nucleus while approaching and departing. To correct for this, a higher level of perturbation theory is required, accounting for the exchange of multiple soft photons, an approach called the Distorted Wave Born Approximation.

A partial wave analysis for this problem can be formulated, with some more expansive but still simplifying assumptions, namely that the momentum is still exchanged with a single photon and that the electron mass remains negligible.

At this level of perturbation theory, the cross section of an interaction of multipolarity L can be written as[103]:

$$\frac{d\sigma_L}{d\Omega} = \frac{E_f^2}{(2\pi\hbar c)^2} \sum_{M_i, mm'} \frac{1}{2J_i + 1} |A_{if}(LMmm')|^2, \quad (8.16)$$

where A_{if} is the matrix element of the interaction Hamiltonian between the initial and final state. To calculate the matrix element, the distorted waves of the incoming and outgoing electron are written in partial wave expansion as:

$$\psi^\mu(\mathbf{p}, \mathbf{r}) = \frac{4\pi}{\sqrt{2}} \sum_{j, \chi, m} e^{i\delta_\chi j} \langle l m - \mu, \frac{1}{2}\mu | j m \rangle Y_l^{\mu*}(\hat{p}) \Psi_\chi^{jm}(\mathbf{r}), \quad (8.17)$$

with the phase shift δ_χ and the two component wave function

$$\begin{aligned} \Psi_x^m(r) &= \frac{1}{r} \begin{pmatrix} g_x(r) \Phi_\chi^m(\hat{r}) \\ i f_x(r) \Phi_{-\chi}^m(\hat{r}) \end{pmatrix} \\ \Phi_x^m(r) &= \sum_{\mu m'} \left\langle l_\chi \mu, \frac{1}{2} m' | j_\chi m \right\rangle Y_{l_\chi}^{m'}(\hat{r}) \chi_{1/2}^{m'}, \end{aligned} \quad (8.18)$$

with $j_\chi = |\chi| - \frac{1}{2}$ and $l_\chi = \chi$ if $\chi > 0$ and $l_\chi = -\chi - 1$ if $\chi < 0$.

The two radial functions of order χ depend on the central potential $V(r)$, which can be derived from the nuclear currents and densities or modelled phenomenologically.

They are calculated from these coupled differential equations:

$$\begin{aligned}\frac{d}{dr}f_{\chi}(r) &= \frac{\chi}{r}f_{\chi}(r) - [E - V(r)]g_{\chi}(r) \\ \frac{d}{dr}g_{\chi}(r) &= -\frac{\chi}{r}g_{\chi}(r) + [E - V(r)]f_{\chi}(r).\end{aligned}\quad (8.19)$$

With these radial functions, the matrix element A_{if} can be rewritten, with the explicit dependence on the transition and ground state charge and current densities included, as:

$$\begin{aligned}A_{if}(LMmm') &= 8\alpha\pi^2 \langle J_i M_i LM | J_f M_f \rangle \sum_{\chi\chi'} (-1)^{L_i l - l'} (2l + 1)^{1/2} \\ &\quad \times e^{i(\delta_{\chi} + \delta_{\chi'})} \langle l' m + M - m', \frac{1}{2}m' | j' m + M \rangle \langle 0 \frac{1}{2}m | jm \rangle \\ &\quad \times \langle jm LM | j' m + M \rangle \langle j' \frac{1}{2}L 0 | j \frac{1}{2} \rangle \\ &\quad \times \left\{ \frac{1}{2} [1 + (-1)^{l+l'+L}] R^E(\chi, L, \chi') \right. \\ &\quad \left. + \frac{1}{2} [1 + (-1)^{l+l'+L+1}] R^M(\chi, L, \chi') \right\} Y_L^{m-m'}(\Theta, 0),\end{aligned}\quad (8.20)$$

where the two additional functions are defined as

$$\begin{aligned}R^E(\chi, L, \chi') &= ik\hat{L} \int \int \varrho_L(\mathbf{r}_N) G_L(\mathbf{r}_N, r_e) v_{\chi\chi'}^1(r_e) \\ &\quad - ky_{L-1}(\mathbf{r}_N) G_{L-1}(\mathbf{r}_N, r_e) \left[v_{\chi\chi'}^3(r_e) \left(\frac{\chi - \chi'}{L} \right) - v_{\chi\chi'}^2(r_e) \right] \\ &\quad + ky_{L+1}(\mathbf{r}_N) G_{L+1}(\mathbf{r}_N, r_e) \\ &\quad \times \left[v_{\chi\chi'}^3(r_e) - \left(\frac{\chi - \chi'}{L+1} \right) v_{\chi\chi'}^2(r_e) \right] r_N^2 dr_N dr_e\end{aligned}\quad (8.21)$$

for electric transitions and as

$$\begin{aligned}R^M(\chi, L, \chi') &= -k \iint \frac{\hat{L}}{[L(L+1)]^{1/2}} (\chi + \chi') J_{L,L}(\mathbf{r}_N) G_L(\mathbf{r}_N, r_e) \\ &\quad \times v_{\chi\chi'}^2(r_e) r_N^2 dr_N dr_e\end{aligned}\quad (8.22)$$

for magnetic multipoles.

Solving these radial equations numerically delivers a result for the cross section under the Distorted Wave Born Approximation, based on the nuclear charge and currents chosen. However, since the reverse, calculating the nuclear distributions from the cross section, is generally not possible, the experimental results are instead treated as if they were derived purely under the Plain Wave Born Approximation. With that they can be decomposed to deliver the form factors, and the inaccuracy introduced by the inadequacy of the assumptions is instead treated as a distortion that can be corrected for. Correspondingly a correction factor is therefore defined as:

$$f_C = \frac{d\sigma}{d\Omega_{\text{DWBA}}} / \frac{d\sigma}{d\Omega_{\text{PWBA}}}.\quad (8.23)$$

This correction factor can then be applied to the measured values so that the extracted cross section can be treated as if it was the one calculated under the Plain Wave Born Approximation.

Chapter 9

Monte Carlo Simulation with MXSim

This chapter will explain the method and software used to combine the results of the two previous chapters and show how to generate expected signal and background rates for our experiment. For this, the method for numerically solving our rate equation will be explained, and then how the MXSim Framework implements this method, which includes an explanation of the software modules used and created for this thesis.

9.1 Principles of Monte Carlo Simulation

With the theory providing us with the information about the factors and their dependencies, we can now appreciate that equation 6.3 cannot be solved analytically. Instead, the Monte-Carlo method is employed, which can be used to evaluate integrals like this for which analytical methods are not feasible. To determine an approximated value $\langle f \rangle$ for the integral in a parameter area defining a volume V a large number N of random numbers within that volume gets generated and the function to be integrated is evaluated at each of these sample points.

The precise value of $\langle f \rangle$ is defined as:

$$\langle f \rangle = \frac{1}{V} \int_V f(x) d^n x, \quad (9.1)$$

which can be approximated as:

$$\langle f \rangle \approx \frac{1}{N} \sum_{i=1}^N f(x_i). \quad (9.2)$$

With that, a Monte Carlo Integration is defined as: [62]

$$\int_V f(x) d^n x = V \langle f \rangle \approx \frac{V}{N} \sum_{i=1}^N f(x_i) \pm \frac{V}{\sqrt{N}} \sqrt{\langle f^2 \rangle - \langle f \rangle^2}. \quad (9.3)$$

The integration parameters for our case of inelastic scattering with a fixed excitation energy are the angles Φ and Θ of the scattered electron. Our events are expected to be evenly distributed in Φ , but our cross section is proportional to $\frac{1}{q^4}$ and so events will not be evenly distributed in Θ . To reduce the statistical error of our sampling,

it is desirable to remedy this by performing importance sampling, i.e. by generating our q^2 , and thus our Θ , by inverse transform sampling from our desired distribution. With that, the probability distribution for our q^2 becomes[62]:

$$p(q^2) = \frac{1}{\nu} \frac{1}{q^4} \quad \text{with} \quad \nu = \int_{q_{min}^2}^{q_{max}^2} p(q^2) dq^2 = \frac{1}{q_{min}^2} - \frac{1}{q_{max}^2}, \quad (9.4)$$

so that it is generated from a random number $u \in]0, 1[$ as

$$q^2 = \frac{1}{\frac{1}{q_{min}^2} - \nu u}. \quad (9.5)$$

In addition, to account for the switch of integration variables from the polar angle Θ to the momentum transfer, we have to calculate a Jacobian J :

$$J = \frac{d \cos \Theta}{dq^2} = \frac{2}{\left(2E_0 + \frac{q^2}{M}\right)^2}. \quad (9.6)$$

From this we get our total integration weight, which accounts for the integration volume V of equation 9.3, as:

$$w = q^4 \nu J (\Phi_{max} - \Phi_{min}). \quad (9.7)$$

9.2 MXSim

MXSim is a modular Monte Carlo integrator. It consists of a single compiled executable, which receives a configuration file, in which the chosen modules for each function are enumerated and the variables required for those modules listed. For this, each module is compiled into a library, which is dynamically selected at runtime. This obviates the necessity to recompile MXSim for each simulation run and allows separation of different versions of the modules into their own individual library, improving readability and modifiability.

MXSim is written in C++, based on the Cola++ software suite originally written for the A1 experiment[107]. MXSim is designed for simulation of electron scattering experiments at low acceptance spectrometers, and is optimised for those use cases. The main categories of modules are the beam, the target, the scattering generator, and the detector, where this last one is an optional inclusion, while the first three are mandatory. Modules are implemented as child classes of a base class which includes the hook for the dynamic choice. Additionally, for each of these main modules there exists an example module of the simplest case: a temporally uniform beam with a spatial gauss spread, a solid state target, a generator for elastic electron scattering off protons and a detector accounting only for spectrometer acceptance. Running MXSim without specifying a detector to use implies a full acceptance detector, and all generated events are stored as primary events. Besides defining acceptances, detectors are also the means by which potential detector responses are simulated, which adds another storage branches for each detector.

From these simplest cases follow implementations for specific purposes, such as a target module modelling a gas-jet target and a detector class which includes a particle

track reconstruction for the magnetic fields of the spectrometers. Further modules can be added to support multiple detector systems, such as running the TPC and Trigger Veto System simultaneously, or to extend the scattering generator with a cross section calculator based on specific physics models. Supporting all these modules are classes for dealing with geometry, four vector maths, radiative corrections, material interactions and an integration with ROOT.

For this thesis, three MXSim modules were written. The first is a scattering generator to deal with inelastic scattering that leaves behind an excited core. The second is a physics model module that serves as a connection to two existing distorted wave born approximation correction factor calculators, `xfoubes` for inelastic scattering and `ELSEPA` for elastic scattering, by linearly interpolating the results from those programs for a continuous measurement area. The third module is for a solid state target with a variable density distribution, such as the one determined in chapter 7. MXSim expects values and calculates with energies in units of gigaelectronvolts, angles in units of radians and lengths in units of millimetres. MXSim includes a unit conversion list for common alternate units like mega electronvolt and meter. MXSim can be run parallel on multiple cores, with its core calculation consisting of the generation of N events, each of which may either be accepted or not accepted. Each accepted event is stored with its particle track, interaction vertex and event weight. These event weights are in units of accepted events, and as such have to include all parameters relevant to both equation 6.3 and equation 9.3.

MXSim receives its simulation parameters at runtime in the form of a plist file, containing the chosen parameters listed in pseudocode format. One or multiple plist files are processed by the executable program of the MXSim framework, named `mxsim`, to select which modules to run with which settings. Besides the modules, `mxsim` expects one global parameter to be set in the plist files it receives, `run.time`, which defines the run time of the simulated measurement run. This is necessary, since `mxsim` is responsible for applying the luminosity and simulated event weights to the per event weight.

9.3 MXSim Modules for simulating the Hoyle State and its Background

The five modules (Generator, Beam, Target, Physics Model and Detector), are combined as shown in figure 9.1. In the following, each module, its function and its needed parameters will be explained.

9.3.1 Inelastic and Elastic Scattering with GenerateHoyle

The generator module, named `GenerateHoyle`, is called by the MXSim program and is in turn responsible for calling all other modules. `Generate Hoyle` calls the beam and target modules, calculates the integration parameters, mainly q_{min}^2 , q_{max}^2 , and v , and then uses random numbers to determine the kinematic parameters, Θ and q^2 , inside those integration parameters. With the kinematic parameters `Generate Hoyle` calculates the event weight according to equation 9.7. The module also calculates energy losses due to internal bremsstrahlung and applies the radiative correction factors of electron-nucleus scattering to the event weight, as well as energy losses

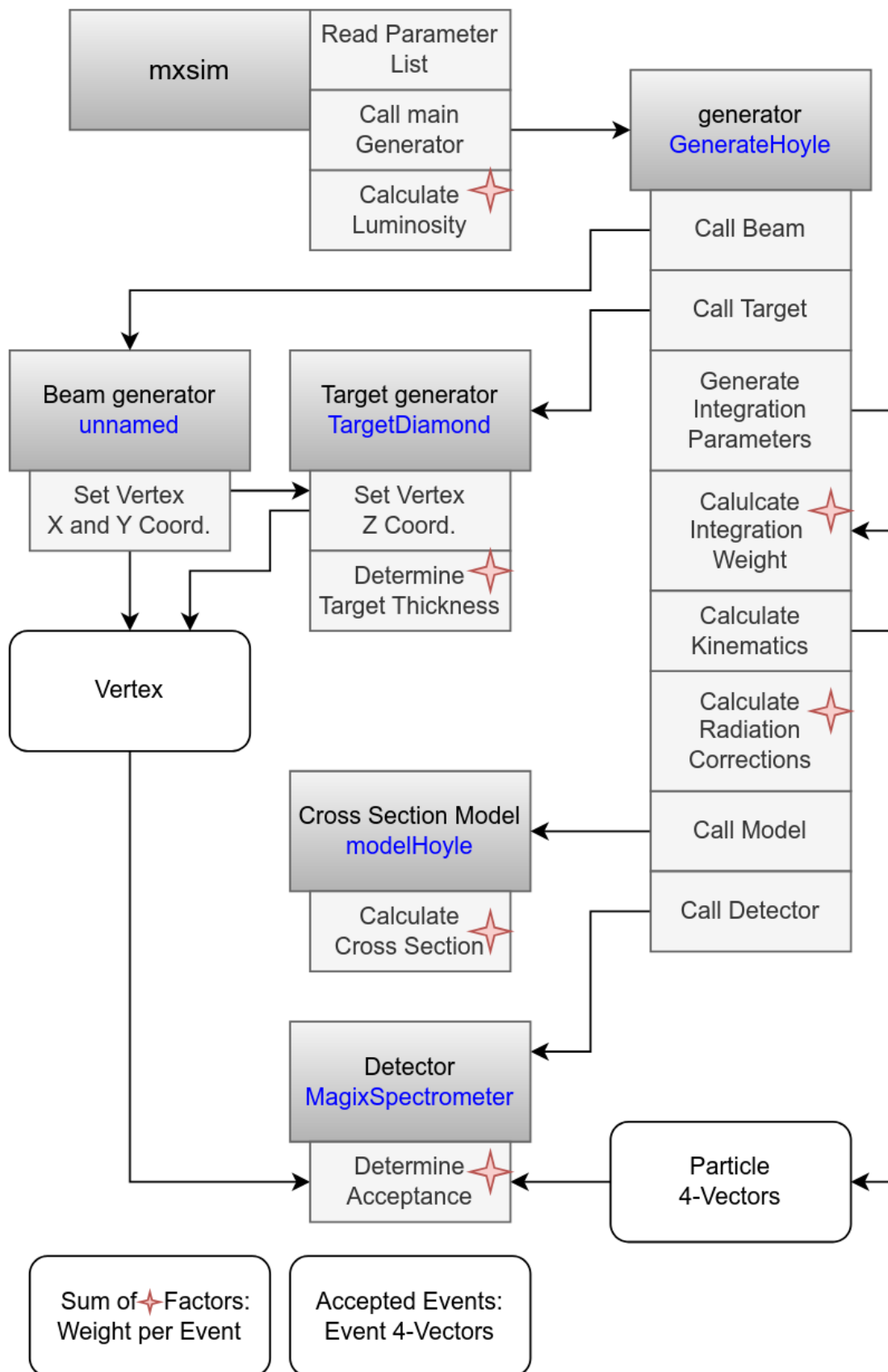


Figure 9.1: Schematic Overview of the simulation of (in)elastic scattering with MXSim.

and angular dispersion from interaction with the rest of the target. `GenerateHoyle` assumes only a single nuclear scattering event.

`GenerateHoyle` requires a number of parameters to be set to define the integration range and expected behaviour, which are given in table 9.1.

`GenerateHoyle`, despite its name, is set up so that by defining the appropriate parameters, and in combination with the correct cross section generator, it can simulate both elastic scattering and inelastic scattering which does not create additional hadrons. Choosing an excitation energy of 0 leads to a calculation of elastic scattering.

Parameter	Example Value	Explanation
generator	"Hoyle"	Specifying which generator module to use
generator.phi	[-70, 70]	Lower and upper bound of Φ in degree
generator.theta	[45, 55]	Lower and upper bound of Θ in degree
generator.mass	12 * 0.93827231 * GeV	Mass of target nucleus
generator.excitation	7.654 * MeV	Excitation energy of the bound state

Table 9.1: *Parameters for GenerateHoyle.*

9.3.2 Generating the Beam

The beam module for `MXSim` generates a two-dimensional Gaussian distributed beam, with a defined beam current, energy and helicity. The beam module accepts the configuration parameters listed in table 9.2, and generates a beam vertex according to those specifications.

Parameter	Example Value	Explanation
beam.energy	30 * MeV	Beam energy
beam.current	0.001 * mA	Beam current
beam.helicity	+1	Beam helicity
beam.sigma.x	1.0 * mm	Standard deviation of beam in x-dir.
beam.sigma.y	1.0 * mm	Standard deviation of beam in y-dir.
beam.offset.x	0.0	Beam offset from centre of target in x-dir.
beam.offset.y	0.0	Beam offset from centre of target in y-dir.

Table 9.2: *Parameters for Beam.*

9.3.3 Target Integration with TargetDiamond

The `MXSim` target module written for this application serves primarily as interface to the measured thickness distribution of our diamond target, but can be used for any target for which such a distribution is known. The module, named `TargetDiamond`, requires the parameters as listed in table 9.3. It has one primary function, `generateZ`, which generates a random z-coordinate for a given vertex by interpolating the thickness of the target at the position of that vertex, and then generating a

uniformly distributed penetration thickness. The interpolated target thickness for that vertex remains available for calculation of energy loss and multiple scattering.

Parameter	Example Value	Explanation
target	"Diamond"	Specifying which target module to use
target.density Distribution FileName	"example Distribution.dat"	Name of the file, to be included in the same directory, which contains the thickness distribution as measured in chapter 7
target.plateWidth	10 * mm	x-dimension of the plate
target.plateHeight	10 * mm	y-dimension of the plate
target.density	0.0035	Density of the target material in kg/cm ³
target.atomicWeight	12.0107	Atomic weight of the target material

Table 9.3: *Parameters for TargetDiamond.*

9.3.4 Cross Section Calculation with ModelHoyle

ModelHoyle can calculate the cross section in three ways, and optionally include the interpolation of the Distorted Wave Born Approximation Correction Factor. The first option is the cross section of the carbon 12 ground state elastic scattering, calculated from the Mott cross section and a form factor parametrization[108] based on real data. The second option is the cross section of inelastic scattering exciting the carbon 12 ground state into the Hoyle state, calculated from a fit on data of equation 8.12[97]. The third option is the same cross section, but instead of using a parametrization, the cross section is instead calculated as an interpolation from a grid of cross section values. These cross section values have to be calculated with an external program. This is a useful option should published cross section data directly be implemented. For this thesis, only the first two options were used.

Table 9.4 shows the parameters required by the module. The file of cross section and correction factor values are expected as comma separated values, with no angle or energy rows or columns. The energies and angles of the grid points are expected to be uniformly distributed between the given start and end values of the angles and energies.

9.3.5 xfoubes and ELSEPA

The external calculations of cross section and correction factors mentioned in the previous sections was performed using xfoubes for the more important inelastic scattering case, since it implements multiple models for full transition densities, as well as accepting external inputs for them. The correction factors for the ground state were calculated using the **E**Lastic **S**cattering of **E**lectrons and **P**ositrons by **A**toms(ELSEPA) program. Both xfoubes and ELSEPA implement a partial wave analysis calculation based on the theory as explained in section 8.3.

Both of these programs are implemented in the FORTRAN77 programming language and perform resource intensive calculations to achieve high precision in their results.

Parameter	Example Value	Explanation
model	"Hoyle"	Specifying which model module to use
model.pwba crossection FileName	"PWBAValue arrayLarge .dat"	Name of the file, to be included in the same directory, which contains the cross section calculated by an external program
model.dwba correction FileName	"CFValue arrayLarge .dat"	Name of the file, to be included in the same directory, which contains the DWBA Correction Factors calculated by an external program
model.energyStart	30 * MeV	Starting energy value
model.energyEnd	105 * MeV	Final energy value
model.angleStart	15	Starting angle value
model.angleEnd	165	Final angle value
model.doDWBA correction	true	Boolean for whether or not the DWBA correction is calculated
model.groundState	false	Boolean for whether the ground state or the Hoyle excitation is calculated
model.extrapolated FormFactor	true	Boolean for whether the cross section is calculated by equation or from interpolation with the file given

Table 9.4: *Parameters for ModelHoyle.*

For this reason, ELSEPA and xfoubes are only used to generate interpolation grids for use in MXSim.

ELSEPA

ELSEPA was originally written by Francesc Salvat, Aleksander Jablonski and Cedric J. Powell[109], and in the version currently used is available at its git repository[110]. ELSEPA has a wide range of possible energies and is designed to deal not only with elastic scattering of electrons and positrons of nuclei, but also deals with the effects of bound electrons, up to and including the effects of molecular bonds on those electrons. ELSEPA calculates the cross section under the Distorted Wave Born Approximation, see equation 8.16, using a number of possible models for the central potential.

When provided with the variables in table 9.5 ELSEPA calculates differential cross sections for the complete angular range between 0 and 180°. The chosen model for central potential, in our case for ease of calculation a uniform distribution, also generates the form factors, with the expectation that the impact of the choice of potential on the correction factor is negligible. If plain cross section values are

desired, more complex central potential are available.

Parameter	Example Value	Explanation
IZ	6	Atomic number of the target nucleus
MNUCL	3	Nuclear charge distribution model
NELEC	6	Number of bound electrons
MELEC	4	Electron charge distribution model
IELEC	-1	Charge of the scattering particle
IHEF	2	high-E factorization of the nuclear screening
EV	3.0E7	Energy of the scattering particle in electronvolt

Table 9.5: *Parameter for ELSEPA.*

The correction factor is extracted from the ELSEPA data using a python wrapper and provided to the ModelHoyle module, which calculates the ground state elastic scattering cross directly from the Mott cross section and a parametrization of the form factor.

What ELSEPA is not equipped to do is calculating inelastic scattering and accounting for the effects of nuclear excitations inherent to that. Since our measurement of the transition to the Hoyle State necessarily has to account for that however, we require an additional cross section calculator that does account for these effects, `xfoubes`, which will be introduced in the following.

xfoubes

`xfoubes`, in the version available for this thesis, was originally written by Jochen Heisenberg[111] and then modified by Maksym Chernykh[97]. `xfoubes` solves the same general set of equations and calculates the same cross section from equation 8.16 that ELSEPA does, but for the more challenging case of inelastic scattering.

Using these formulas `xfoubes` calculates the cross section under the Distorted Wave Born Approximation, and optionally under the Plain Wave Born Approximation as well, which are then used to calculate the correction factor. `xfoubes` has to be supplied with the parameters for this operation with a file, where a parameter is identified only by its line and position within that line. The names of the parameters given in the following table come from the manual therefore, and are not included in the configuration file like is the case for `MXSim` and `ELSEPA`.

A python wrapper is used to generate a grid of cross sections and correction factors, for 380 energies between 30 and 105 MeV and 1500 angles between 15 and 165°.

xfoubes and ELSEPA Results

The existing `xfoubes` code was serialized to produce a dense grid of correction factors for interpolation in the relevant area, a beam energy between 30 and 105 MeV and a scattering angle between 15° and 165°. The correction factors extracted from this are shown in figure 9.2.

Similarly, the same was done for `ELSEPA`, delivering figure 9.3.

Line.Position	Name	Example Value	Explanation
1.1	OUTPUT FILENAME	out	Filename for the result
2.1	Z	6	Nuclear charge
2.2	A	12	Mass in u
2.3	EXE	7.654	Excitation energy in MeV
2.3	RK	7.5	Ground state radius containing all charge in fm
2.3	L	0	Multipolarity
2.3	AERR	0	Added error
2.3	SSTEP	1	Computation parameter determining accuracy
3.1	MODEL	0	Ground state model, here a 3-parameter Fermi distribution
3.2	MODTR	6	Transition density model, 6 means a list is given
3.3	MODFIT	0	Fitting mode
3.4	JINIT	0	Ground state spin
3.5	JFIN	0	Final state spin
4.1	EXBE	6.0	Experimental transition strength
4.1	DEXBE	0.01	Error of experimental transition strength
4.1	BEL	0	Starting value for transition strength of fit
5	GSC(12)		Ground state charge distribution parameters
6.1	R1	0.05	Stepsize of RHO
6.2	NAMP	199	Number of entries in RHO
7	RHO(NAMP)		list of charge density values
8.1	RMOD	10	Cutoff radius for densities
8.2	NPAR	15	Number of Parameters of fit
8.3	NBE	0	Boolean for allowing varying of transition probability
8.4	NITER	4	Number of iterations
8.5	NSTEP	4	Number of recalculations
9	FOPTION	MBRN	Unit format determiner
10.1	E	55	Electron energy in MeV
10.2	DLE	0	Electron energy spread
10.3	THETA	90	Spectrometer angle in degrees
10.4	DTHET	0	Spectrometer horizontal angle(not used)
10.5	VERT	0	Spectrometer vertical angle(not used)
10.6	SIGMA	2.90E-05	External cross section estimate(not used)
10.7	DSIGMA	6.0E-7	Error of cross section estimate(not used)
10.8	TCK	0	Target thickness(not used)

Table 9.6: *Parameters for xfoubes.*

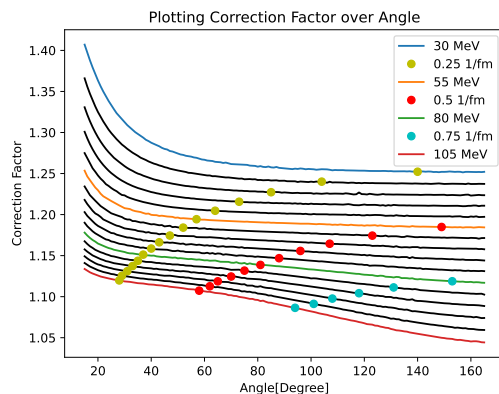


Figure 9.2: Plot of the DWBA correction factor over the MAGIX angle range for inelastic scattering, with the carbon 12 target being excited from the ground state to the Hoyle State.

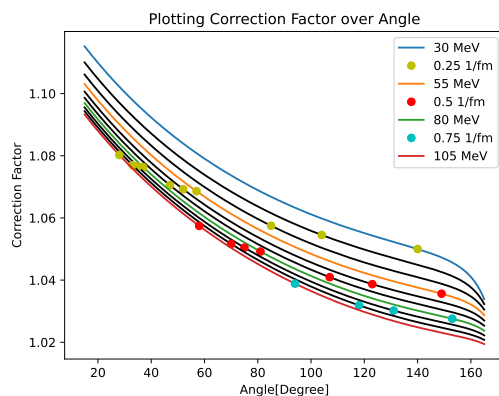


Figure 9.3: Plot of the DWBA correction factor over the MAGIX angle range for elastic scattering of the carbon 12 target.

9.3.6 Detector Simulation with MagixSpectrometer

The MagixSpectrometer detector module is a basic acceptance check. It checks whether a particle track would fit through the acceptance defining collimator, and if the particle has a momentum that would be accepted by the magnet settings of the spectrometer. For this, it only requires the central momentum setting and angular position of the spectrometer, as given in table 9.7. If an event has a track or momentum that would not be accepted by the spectrometer, MagixSpectrometer sets its weight to 0, if it does, the event is stored as valid.

As MAGIX is a two spectrometer experiment, with additional detectors to be deployed along the beam line and in the scattering chamber, it is possible to call multiple instances of a detector class module, unlike with the other types. The electron prefix for the parameters in the table is one instance of a detector class, with a second instance merely requiring a different unique name to differentiate them.

The MXSim Detector class already has an implementation of the algorithm for translation between target and focal plane coordinates, mentioned in section 2.3, and of both types of detectors. With those modules, it is possible to generate not just particle tracks for event rates, but also the full detector response[45]. For the

Parameter	Example Value	Explanation
electron	"MagixSpectrometer"	Specifying which model module to use
electron.momentum	47*MeV	Central momentum of the spectrometer
electron.angle	70.0	Spectrometer angle in degrees

Table 9.7: *Parameters for MagixSpectrometer.*

reconstruction of particle tracks from detector there has been work done using both classical image recognition[59] and machine learning methods[112], with a Master's Thesis by Nils Hesse currently underway to unify and compare the two.

9.4 Analysis

Accepted events are stored in a ROOT tree and analysed using ROOT macros. The ground state and excited state each generate their own independent ROOT trees, that are analysed both separately and combined. To extract signal and background rates in the region of interest, two methods were employed. In the simple case, the combined output of both simulations in the energy region of interest was fitted with a constant background and a crystal ball function[113], to model the excitation peak with radiative losses, and the two resultant functions integrated. Where no fit was possible, the signal and background rates were counted directly.

The final chapter of this part will now discuss the result of the analysis of these simulations.

Chapter 10

Results

Combining everything from the three previous chapters, the results of our simulations can now be investigated. Based on these results, the expected reach and recommended settings of the first measurement at MAGIX are provided.

10.1 Validating the Results

To validate the simulation, the results are first compared very qualitatively with real data. The A1 facility has taken data at higher energies than are reachable with MESA, with a thicker target and additional radiative losses. Figures 10.1 and 10.2 compare data to simulation with the same kinematics. The data includes additional nuclear excitations and has much wider peaks due to higher radiative losses, but agrees with the simulation qualitatively.

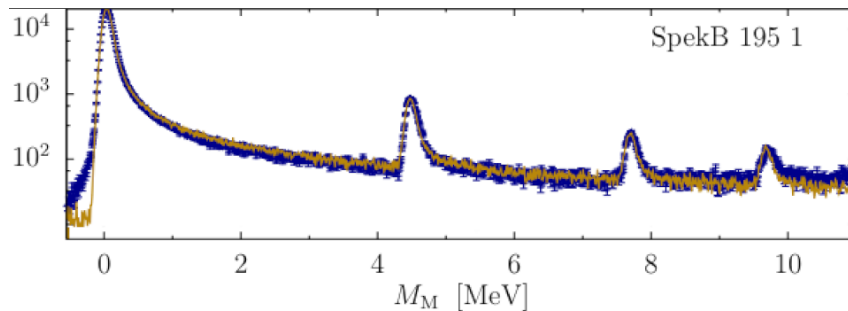


Figure 10.1: Real measurement of electron scattering off carbon at the A1 facility, with a spectrometer central momentum of 195 MeV and spectrometer angle of 15° . Image from [114].

To check the analysis, figure 10.3 shows a comparison between the equation that generates the form factor of the transition between the ground state and the Hoyle State, equation 8.14, and the same value extracted from the simulated data. This shows that what goes into the simulation is correctly extracted again after the full simulation and analysis chain.

Missing Mass

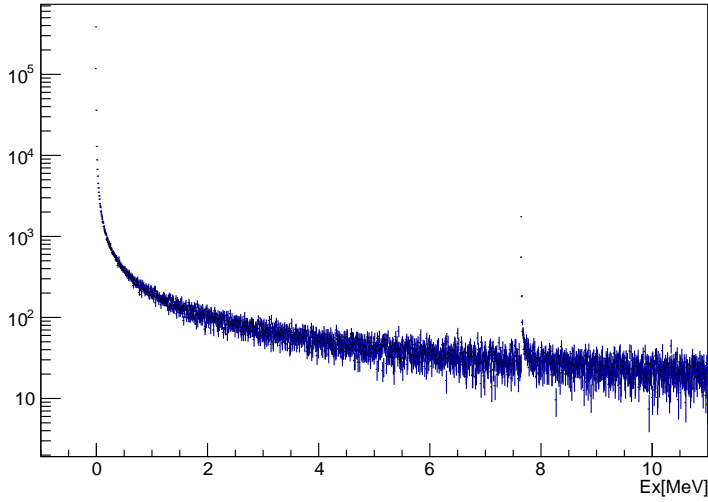


Figure 10.2: *Equivalent measurement at MAGIX, at a spectrometer central momentum of 195 MeV and spectrometer angle of 15°.*

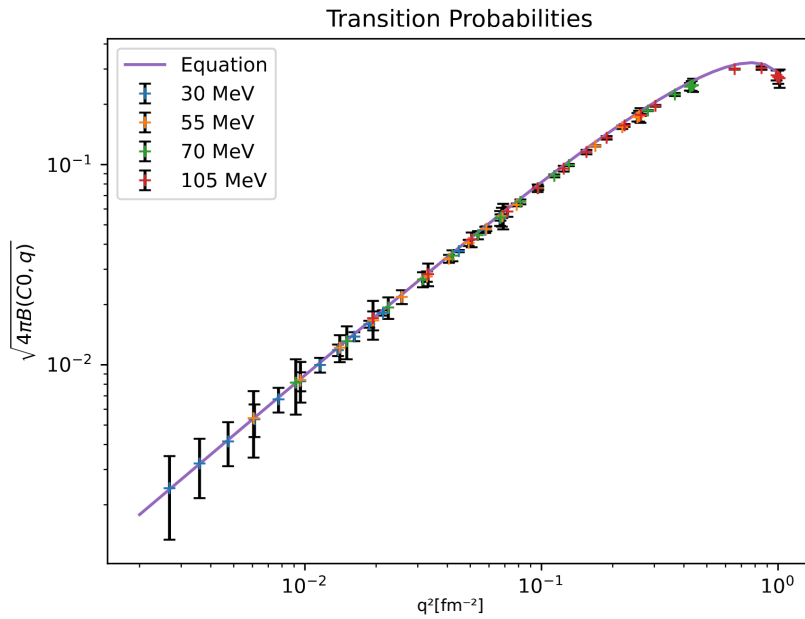


Figure 10.3: *Transition form factor as given by Chernykh, used to simulate the data, compared to the transition form factor extracted from that simulated data.*

10.2 Expected Reach for the MAGIX Hoyle State Measurement

MXSim was used to simulate the expected signal and background rates of measurements of the Hoyle State for momentum transfers q^2 between 0.0158 and 1.09 fm^{-2} , equating to a grid of energies between 30 and 105 MeV and spectrometer angles between 15 and 165°. For this, a conservative assumption on the intensity and availability of accelerator and experiment is made, with a beam current of 1 μA and

a run time per setting of one hour. The target is the diamond plate as measured in chapter 7. At the beginning of data taking at MESA, the only energy expected to be available is 55 MeV, with the upper limit of 105 MeV becoming available some time after that. 30 MeV is the lower bound of the energy available at MESA, to come at some point after that, with investigation into the possibility of lowering this underway. 70 MeV completes the sequence, but this beam energy is not planned to be available for the measurement.

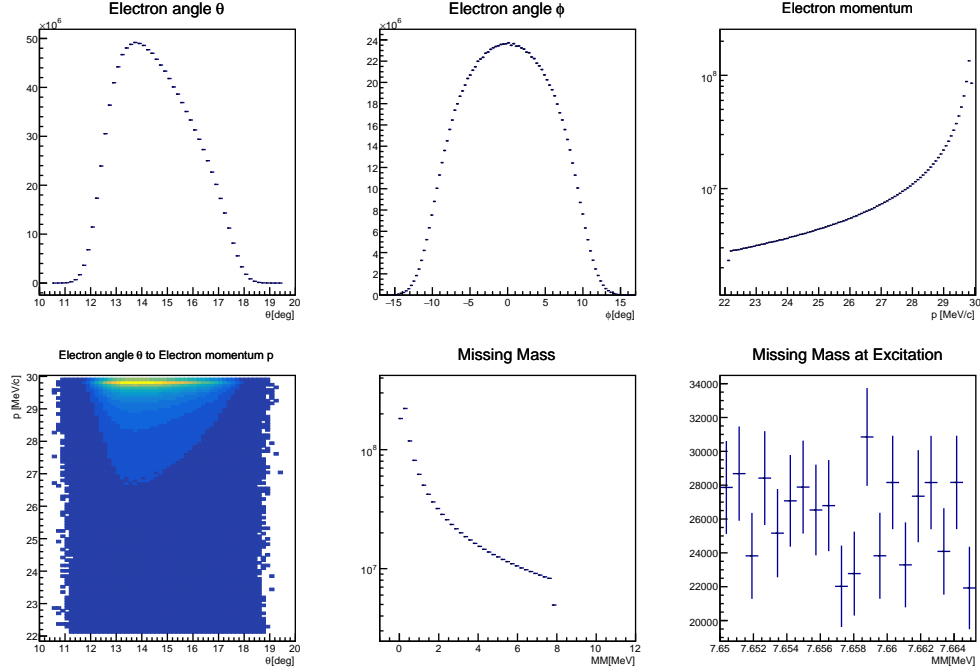


Figure 10.4: *Result of 30 MeV and 15° run.*

Figures 10.4 and 10.5 show the results of the simulations for the lowest $q^2 = 0.00268 \text{ fm}^{-2}$, at an energy of 30 MeV and spectrometer angle of 15°, and highest $q^2 = 1.09333 \text{ fm}^{-2}$, at an energy of 105 MeV and spectrometer angle of 165°. The two figures show the angles and momentum of the scattered particles in the first row. The two histograms of angular distribution show the acceptance of our circular collimator, and the histograms including scattering momentum show momentum acceptance.

The second row begins with a plot of scattering angle Θ plotted against scattering momentum, with the elastic peak very visible at the top, as of course no scattered particles can exceed that energy. The last two plots in the second row are histograms of the missing mass, the first over the whole reach, and the second only in close vicinity of the excitation energy. The missing mass is defined by the difference between the mass of the target nucleus and the invariant mass of the four-vector of the target nucleus after scattering. The four-vector of the target nucleus after scattering can be calculated from the two known initial four-vectors of the beam electron and the target nucleus of known mass, which is assumed to have negligible energy compared to the electron, and the measured four-vector of the scattered electron:

$$M_M = \sqrt{(E_i + M_T - E_f)^2 - \|\vec{p}_i - \vec{p}_f\|^2}, \quad (10.1)$$

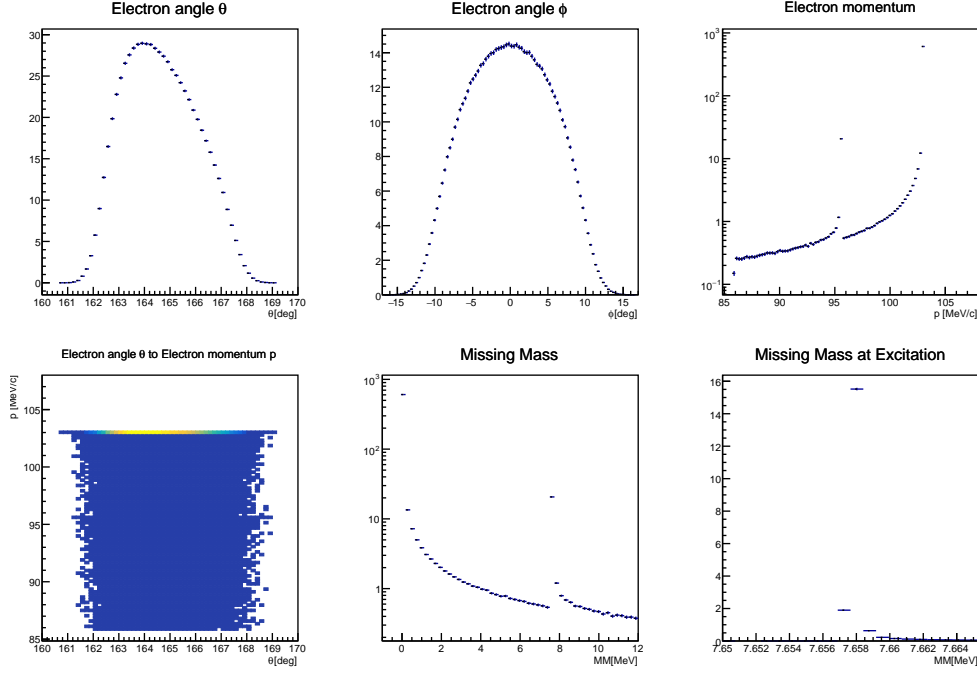


Figure 10.5: *Result of 105 MeV and 165° run.*

with the initial energy E_i and the final energy E_f of the electron, the mass of the target nucleus M_T , and the initial momentum \vec{p}_i and final momentum \vec{p}_f of the electron.

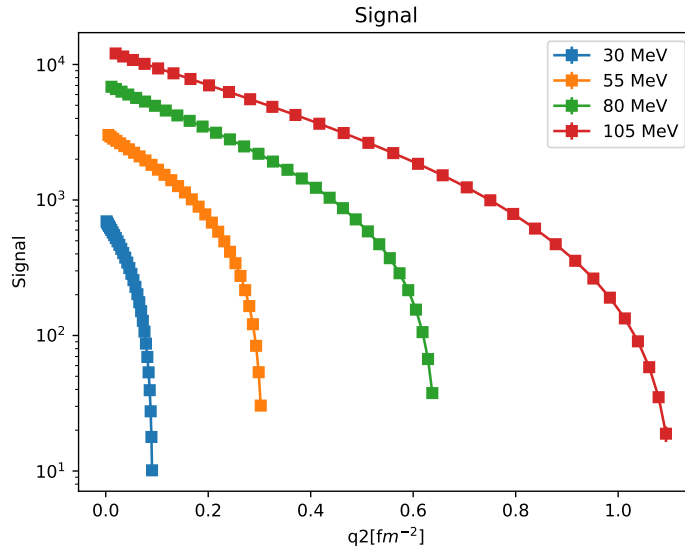


Figure 10.6: *Plot of Signal Rates in dependence of Q^2 for all four energies and 31 angles.*

This missing mass is used to cleanly identify the peak belonging to the excitation into the Hoyle State, since unlike the equivalent peak in the scattering momentum or energy loss spectrum, the position of events belonging to excitations into the Hoyle State remains at the same position in the missing mass spectrum. Placing an upper and a lower limit on the missing mass of an event, thereby cutting on the

missing mass, is therefore used to identify events that are either our signal, or part of the background.

For this simulation, only a single source of background was simulated, the irreducible background of the radiative tail of the elastic peak. There is an additional component to the irreducible background from the radiative tail of the first excited state of carbon 12. This is expected to be negligible compared to that of the elastic peak and therefore is not simulated.

Due to MAGIX's ultra low background setup, we expect little to no other experiment dependent background that will be picked up by the detectors. With the veto capability of the Trigger Veto System, we predict to be able to exclude the supermajority of experiment independent or beam related background. As such, both of these sources of background are not simulated here.

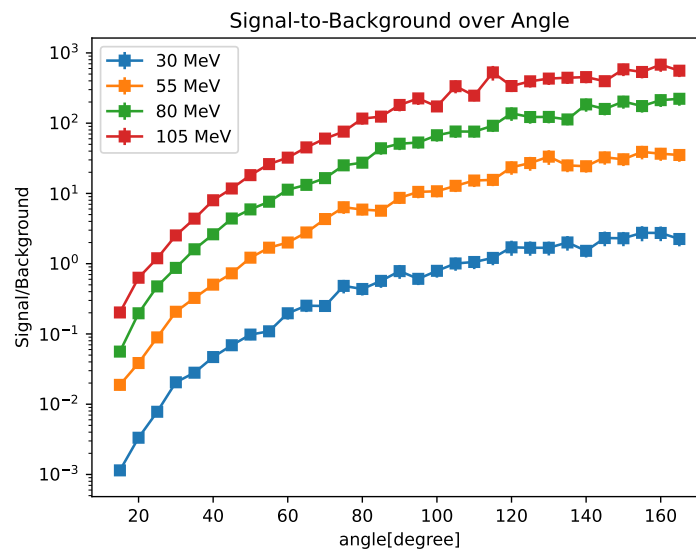


Figure 10.7: *Plot of Signal-to-Background ratio over the angle range of the MAGIX spectrometers.*

To understand the criteria for a meaningful measurement, the signal rate and the signal-to-background ratio, consider figures 10.4 and 10.5. The plot in figure 10.4 shows no visible peak in the Missing Mass at Excitation histogram, meaning that no reasonable measurement is possible at this kinematic setting and runtime. Figure 10.5, on the other hand, shows a clear peak in both histograms, meaning a measurement is possible at this setting. However, here the total number of events in the peak is extremely low, numbering only 20. This is not enough to extract a value of interest with meaningful precision, meaning that no reasonable measurement is possible at this kinematic setting and runtime, either.

Between these two extremes in energy and angle, there lies a region where data can be taken at acceptable rates without a background that makes measuring those rates impossible. Increasing the runtime or beam current would improve both signal rates and signal-to-background ratio, by reducing the statistical spread of the background, thereby enabling a clearer identification of the signal, and by increasing the signal rate. This would increase the region at which we can measure. To identify the region for the beam current and runtime chosen for this simulation, figures 10.6 to 10.8 are generated.

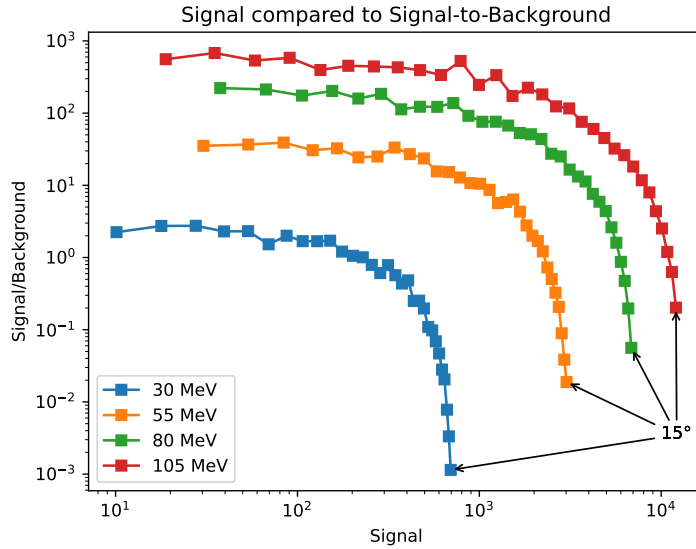


Figure 10.8: *Signal/Background Ratio plotted against Signal rate for the four different energies and over the 15° to 165° angular range. Each energy reaches an upper limit to its signal rate with decreasing angle, and an upper limit to its signal to noise ratio when increasing the angle.*

Energy [MeV]	Angle	q^2 [fm ⁻²]	Signal	Background
55	35	0.0281	2622	8048
55	40	0.0363	2500	4967
55	45	0.0454	2365	3245
55	90	0.155	1137	131
55	95	0.168	1010	96
105	20	0.0341	11453	18144
105	25	0.0530	10792	9031
105	30	0.0758	10105	4001
105	100	0.658	1522	9
105	105	0.704	1239	4

Table 10.1: *Recommended energy and angle settings for the first MAGIX measurement run, with the q^2 and expected signal and background counts.*

Signal and background rates for these plots are the number of events given by a fit of the peak and background in the missing mass histogram if possible, and by direct count of the two differing data sets if not. It is apparent from figure 10.6 that signal rates increase both with lower q^2 , and therefore lower angles, and higher energies. At the same time, figure 10.7 shows that signal-to-background also improves with increased energy, and decreases sharply at lower angles. Combining these two leads to figure 10.8.

Figures 10.10 to 10.13 show the point at which the signal-to-background ratios reach the point that a fit of the peak was possible, which was chosen as the lower limit of the angle. This is a preliminary criterion, with plenty of opportunity for refinement, by, for example, improving the cut condition.

At the energies planned to be in use, 55 MeV and 105 MeV, we are therefore restricted

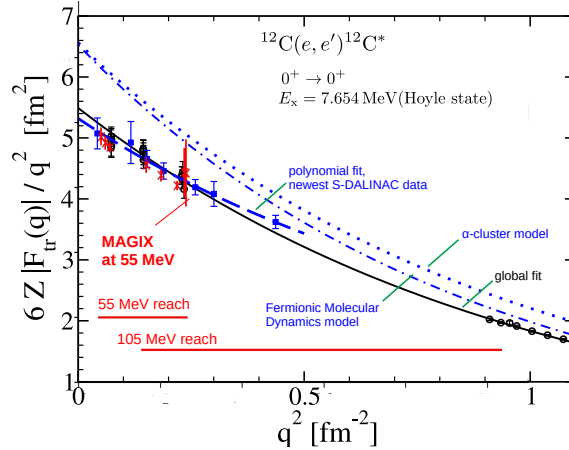


Figure 10.9: Projected reach of the MAGIX measurement of the transition form factor. Image from [115], over-layed with the reach of MAGIX.

to angles above 35° and 20° , respectively. The upper angle limit is given by the signal rate, where an expected count of more than 1000 events is desired. With these limits the expected range of q^2 is between 0.028 and 0.704 fm^{-2} .

The recommended settings for the first measurement at MAGIX are therefore enumerated in table 10.1.

These settings are preliminary and based on expectations on the beam intensity, available energies and possible runtime as mentioned above, which can and will be updated once the accelerator is completed. A finer grid of samples in the energy range might slightly lower the permitted angles as well. All this leads to a prediction of the reach of MAGIX for the transition form factor of the excitation from the ground state of carbon 12 into the Hoyle State, which is shown in image 10.9.

With this, the measurement of the Hoyle State at MAGIX awaits only the completion of its detectors and initialization of beam on target by MESA.

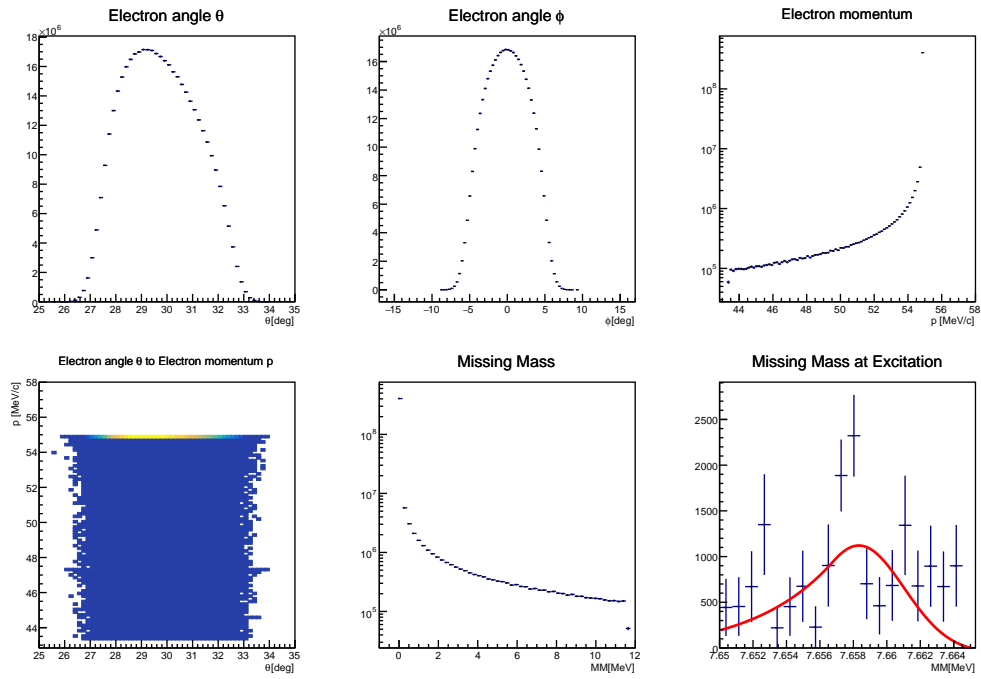


Figure 10.10: *Result of 55 MeV and 30° run.*

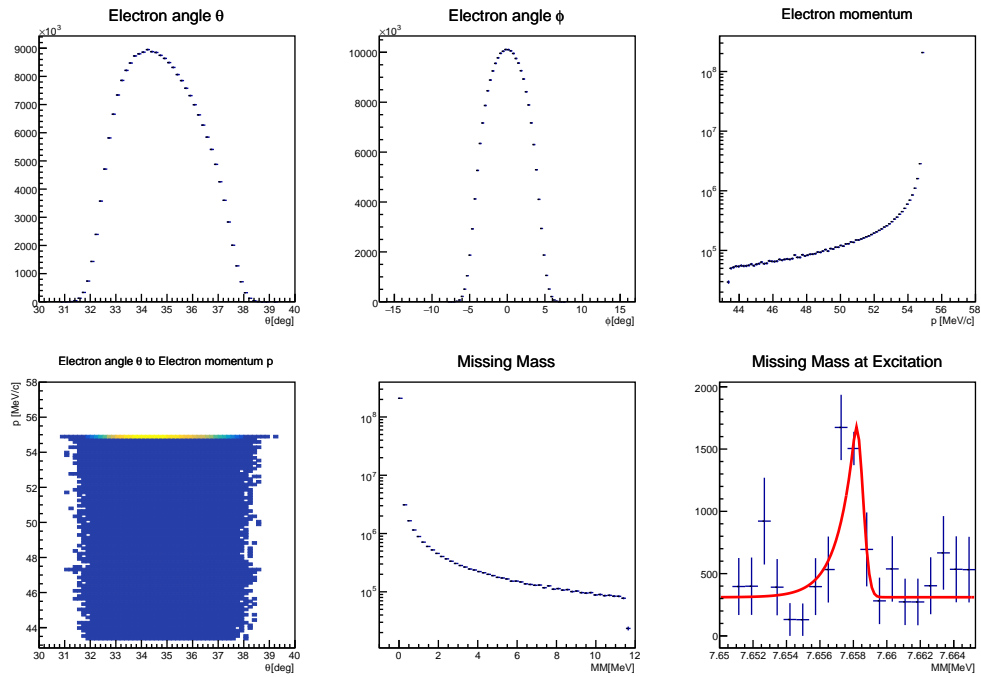


Figure 10.11: *Result of 55 MeV and 35° run.*

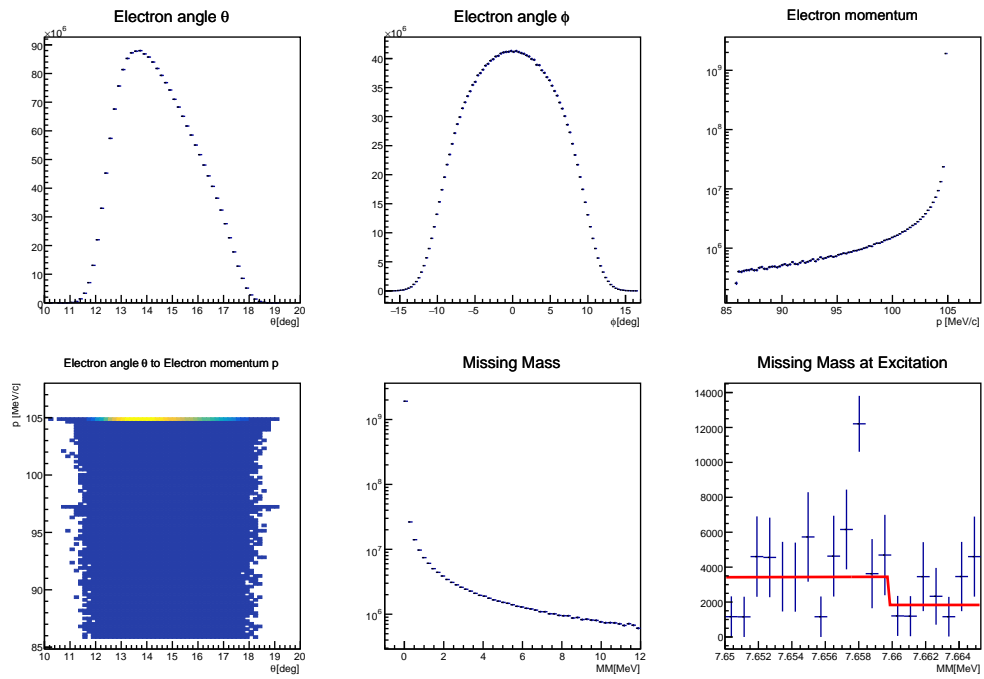


Figure 10.12: *Result of 105 MeV and 15° run.*

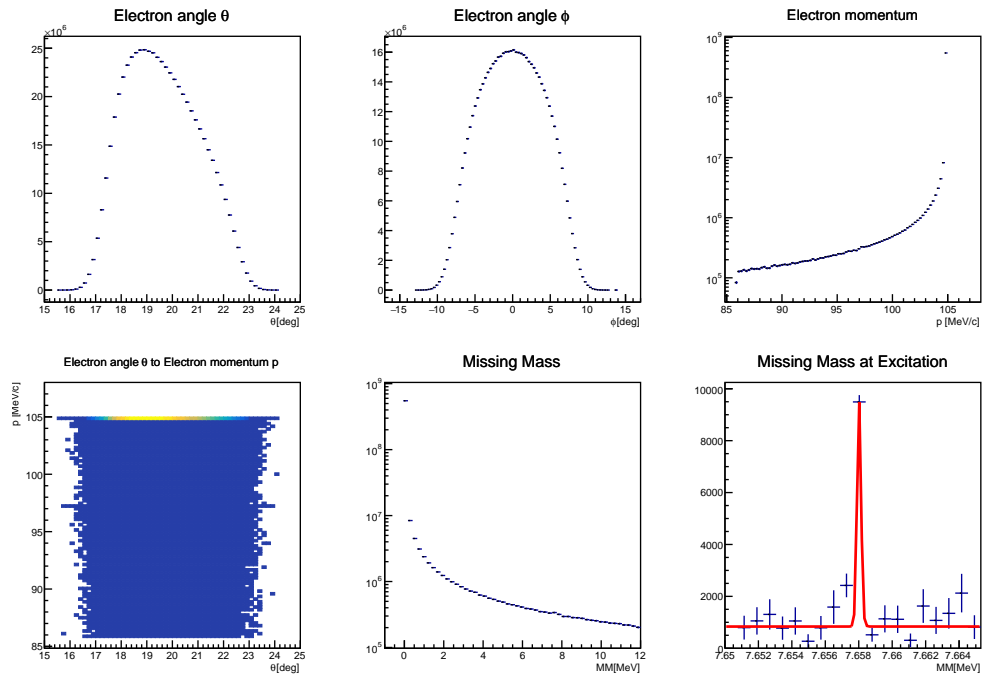


Figure 10.13: *Result of 105 MeV and 20° run.*

Part IV
Conclusion

Summary and Conclusion

In this thesis, the complete design of the focal plane tracking detectors for the MAGIX experiment is presented. It provides a comprehensive reference for the construction and operation of the TPCs that form the tracking system of MAGIX. The first full-scale TPC has been successfully constructed and is now operational for configuration, calibration tests, and subsequent measurements. In addition, this work establishes the framework for the simulation of the first physics run at MAGIX and for the analysis of the resulting experimental data.

The first part of this thesis outlined the wide range of physics topics that can be explored with MAGIX, and described the accelerator MESA and the three major experiments that will be run on it, with a focus on MAGIX. The physics topics include precision measurements of the electric and magnetic form factors of the proton, searches for particles in the dark sector, investigations in few body physics, and reactions of astrophysical relevance. In particular, the formation of oxygen 16 through the α -capture on carbon 12 and the production of carbon 12 via the triple- α -process were discussed. The experimental design, centred around the gas-jet target and optimised to minimise background while maintaining high luminosity, enables precision measurements of these processes under well-controlled conditions.

The second part focused on the focal plane tracking detectors, which serve as the primary measurement instruments of the MAGIX spectrometers by reconstructing the trajectories of scattered particles. The five major components of the detector system were described in detail, together with their respective roles in the overall design. Particular emphasis was placed on two key innovations: the open field cage design and the calibration method based on electron generation via the transmissive photoelectric effect. Initial tests demonstrate that the amplification and readout systems perform reliably, even under non-ideal operating conditions, confirming the viability of the detector concept and the stability of the readout chain.

The third part described the preparations for the first experiment to be performed at MAGIX, namely the measurement of the transition from the carbon 12 ground state to the Hoyle State. This work included the identification, acquisition, and characterization of the target material, a study of the theoretical background and the treatment of the dominant correction factors required for the interpretation of the data, the implementation of dedicated MXSim modules to perform realistic simulations of the measurement, and the determination of the optimal experimental settings.

With the work presented in this thesis, the first focal plane tracking detector of MAGIX is ready to enter its testing and calibration phase, and the groundwork for the first experimental measurement has been established. The experience gained during the construction and commissioning of the first TPC will guide the improved construction of the two remaining detectors. Once completed, the Starry Night

calibration modules will be integrated into the system to enable precise detector calibration. At the same time, the simulation framework will continue to evolve alongside the ongoing development of MAGIX and MESA, ensuring that the experiment is fully prepared to begin data taking as soon as the accelerator beam becomes available.

Taken together, the work presented here establishes the detector infrastructure and methodological foundation required for the first generation of precision measurements at MAGIX and represents an important step toward the realization of its experimental physics program.

Bibliography

- [1] K. Freese. “Review of Observational Evidence for Dark Matter in the Universe and in upcoming searches for Dark Stars”. In: *EAS Publications Series* 36 (2009), pp. 113–126. ISSN: 1638-1963. DOI: 10.1051/eas/0936016. URL: <http://dx.doi.org/10.1051/eas/0936016>.
- [2] D. et all Clowe. “A Direct Empirical Proof of the Existence of Dark Matter”. In: *The Astrophysical Journal* 648.2 (Aug. 2006), pp. L109–L113. ISSN: 1538-4357. DOI: 10.1086/508162. URL: <http://dx.doi.org/10.1086/508162>.
- [3] *Chandra X-Ray Observatory Website*. URL: <https://chandra.harvard.edu/photo/2025/bullet/> (visited on 07/15/2025).
- [4] S. Merkel. “Precision Monte Carlo Studies for Dark Photon Searches at MAGIX”. Bachelor’s Thesis. Johannes Gutenberg-Universität Mainz, 2025.
- [5] M. Christmann et al. “Detector response of Cherenkov radiators for calorimetry in the energy range below 14 MeV”. In: *Nuclear Instruments and Methods in Physics Research Section A: Accelerators, Spectrometers, Detectors and Associated Equipment* 960 (2020), p. 163665. ISSN: 0168-9002. DOI: <https://doi.org/10.1016/j.nima.2020.163665>. URL: <https://www.sciencedirect.com/science/article/pii/S0168900220302369>.
- [6] B.S. Schlimme et al. *The MESA physics program*. 2024. arXiv: 2402.01027 [nucl-ex]. URL: <https://arxiv.org/abs/2402.01027>.
- [7] G. A. Miller. “Defining the proton radius: A unified treatment”. In: *Phys. Rev. C* 99 (3 Mar. 2019), p. 035202. DOI: 10.1103/PhysRevC.99.035202. URL: <https://link.aps.org/doi/10.1103/PhysRevC.99.035202>.
- [8] C. Legris et al. *Nucleon charge radius measurement with low-energy electron scattering*. 2025. arXiv: 2507.19862 [nucl-ex]. URL: <https://arxiv.org/abs/2507.19862>.
- [9] E. E. Chambers and R. Hofstadter. “Structure of the Proton”. In: *Phys. Rev.* 103 (5 Aug. 1956), pp. 1454–1463. DOI: 10.1103/PhysRev.103.1454. URL: <https://link.aps.org/doi/10.1103/PhysRev.103.1454>.
- [10] R. Pohl et al. “The size of the proton”. In: *Nature* 466 (2010), pp. 213–216. DOI: <https://doi.org/10.1038/nature09250>.
- [11] H. Merkel. *Proton Form Factor Measurements*. Presentation at the MAGIX collaboration meeting 2023. 2023.
- [12] A. Gasparian et al. *PRad-II: A New Upgraded High Precision Measurement of the Proton Charge Radius*. 2022. arXiv: 2009.10510 [nucl-ex]. URL: <https://arxiv.org/abs/2009.10510>.

- [13] *MUSE Website*. URL: <https://www.psi.ch/en/muse/experiment> (visited on 11/18/2025).
- [14] K. Eichhorn. Presentation at the MAGIX Mainz Meeting. URL: https://indico.cern.ch/event/1459380/contributions/6525079/attachments/3078151/5448783/2025-06_AMBER_PRM_PAW_Eichhorn.pdf.
- [15] Y.-H. Lin, H.-W. Hammer, and U.-G. Meißner. “The proton magnetic radius: A new puzzle?” In: *Science Bulletin* 69.4 (2024), pp. 419–421. ISSN: 2095-9273. DOI: <https://doi.org/10.1016/j.scib.2023.12.038>. URL: <https://www.sciencedirect.com/science/article/pii/S209592732300909X>.
- [16] M. Wang et al. “The AME 2020 atomic mass evaluation (II). Tables, graphs and references*.” In: *Chinese Physics C* 45.3 (Mar. 2021), p. 030003. DOI: 10.1088/1674-1137/abddaf. URL: <https://dx.doi.org/10.1088/1674-1137/abddaf>.
- [17] E. M. Burbidge et al. “Synthesis of the Elements in Stars”. In: *Rev. Mod. Phys.* 29 (4 Oct. 1957), pp. 547–650. DOI: 10.1103/RevModPhys.29.547. URL: <https://link.aps.org/doi/10.1103/RevModPhys.29.547>.
- [18] Marc R. “Origin and evolution of the elements: edited by Andrew McWilliam and Michael Rauch”. In: *Meteoritics & Planetary Science* 40.2 (2005), pp. 331–332. DOI: <https://doi.org/10.1111/j.1945-5100.2005.tb00385.x>. eprint: <https://onlinelibrary.wiley.com/doi/pdf/10.1111/j.1945-5100.2005.tb00385.x>. URL: <https://onlinelibrary.wiley.com/doi/abs/10.1111/j.1945-5100.2005.tb00385.x>.
- [19] M. Aliotta et al. “Exploring Stars in Underground Laboratories: Challenges and Solutions”. In: *Annual Review of Nuclear and Particle Science* 72. Volume 72, 2022 (2022), pp. 177–204. ISSN: 1545-4134. DOI: <https://doi.org/10.1146/annurev-nucl-110221-103625>. URL: <https://www.annualreviews.org/content/journals/10.1146/annurev-nucl-110221-103625>.
- [20] S. Lunkenheimer. *Studies of the $^{16}\text{O}(\gamma^*, \alpha)^{12}\text{C}$ reaction for astrophysical relevance at MAGIX/MESA*. 2019.
- [21] P. Yin et al. *Alpha-Particle Monopole Form Factors with Ab Initio No-Core Shell Model*. 2025. arXiv: 2412.18037 [nucl-th]. URL: <https://arxiv.org/abs/2412.18037>.
- [22] S. Dürr et al. “Ab Initio Determination of Light Hadron Masses”. In: *Science* 322.5905 (2008), pp. 1224–1227. DOI: 10.1126/science.1163233. URL: <https://www.science.org/doi/abs/10.1126/science.1163233>.
- [23] R. Machleidt and F. Sammarruca. “Chiral EFT based nuclear forces: achievements and challenges”. In: *Physica Scripta* 91.8 (July 2016), p. 083007. ISSN: 1402-4896. DOI: 10.1088/0031-8949/91/8/083007. URL: <http://dx.doi.org/10.1088/0031-8949/91/8/083007>.
- [24] S. Bacca et al. “Isoscalar Monopole Resonance of the Alpha Particle: A Prism to Nuclear Hamiltonians”. In: *Phys. Rev. Lett.* 110 (4 Jan. 2013), p. 042503. DOI: 10.1103/PhysRevLett.110.042503. URL: <https://link.aps.org/doi/10.1103/PhysRevLett.110.042503>.

- [25] D. Simon. “Gesamtkonzept für den MESA-Teilchenbeschleuniger unter besonderer Berücksichtigung von Strahloptik und Kryogenik”. Dissertation. Johannes Gutenberg-Universität Mainz, 2021.
- [26] D. Becker et al. “The P2 experiment”. In: *Eur. Phys. J. A* 54.11 (2018), p. 208. DOI: 10.1140/epja/i2018-12611-6. arXiv: 1802.04759 [nucl-ex].
- [27] R. Thapa. *Overview of the MESA*. 2023. URL: <https://indico.kit.edu/event/3681/contributions/13720/attachments/6434/10177/KITMESAOverview.pdf>.
- [28] *AG Berger - P2 Website*. URL: <https://agberger.kph.uni-mainz.de/experiments/p2/> (visited on 05/20/2025).
- [29] M. Christman. *DarkMESA – Status and Next Step, Collaboration Meeting 2025*. Presentation at the MAGIX collaboration meeting 2025. 2025.
- [30] M. Lauss. “Characterization and Optimization of Calorimeter and Active Veto Systems for Light Dark Matter Searches at DarkMESA”. Dissertation. Johannes Gutenberg-Universität Mainz, 2026.
- [31] B.S. Schlimme et al. “Operation and characterization of a windowless gas jet target in high-intensity electron beams”. In: *Nuclear Instruments and Methods in Physics Research Section A: Accelerators, Spectrometers, Detectors and Associated Equipment* 1013 (Oct. 2021), p. 165668. ISSN: 0168-9002. DOI: 10.1016/j.nima.2021.165668. URL: <http://dx.doi.org/10.1016/j.nima.2021.165668>.
- [32] S. Grieser et al. “A cryogenic supersonic jet target for electron scattering experiments at MAGIX@MESA and MAMI”. In: *Nuclear Instruments and Methods in Physics Research Section A: Accelerators, Spectrometers, Detectors and Associated Equipment* 906 (2018), pp. 120–126. ISSN: 0168-9002. DOI: <https://doi.org/10.1016/j.nima.2018.07.076>. URL: <https://www.sciencedirect.com/science/article/pii/S0168900218309124>.
- [33] A. Täschner. “Entwicklung und Untersuchung von Cluster-Jet-Targets höchster Dichte”. Dissertation. Westfälischen Wilhelms-Universität Münster, 2012.
- [34] J. Froning. *Plans for operating the MAGIX target in filament mode, Collaboration Meeting 2025*. 2025.
- [35] S. Stengel. “Design and Development of the MAGIX Trigger Veto System”. Dissertation. Johannes Gutenberg-Universität Mainz, 2024.
- [36] *Micron Semiconductor Silicon Catalogue*. Available at <http://www.micronsemiconductor.co.uk/wp-content/uploads/2024/03/2024-MSL-Catalogue.pdf>. Micron Semiconductor Ltd. Lancing, West Sussex, UK, 2024.
- [37] J. Schlaadt. “Konstruktion eines neuen Veto-Detektors für den Strahl-Halo am MAGIX-Experiment”. Bachelor’s Thesis. Johannes Gutenberg-Universität Mainz, 2021.
- [38] F. Höwelberend. “Spurparametrisierung und Fokalebenensimulation für die MAGIX-Spektrometer”. Bachelor’s Thesis. Johannes Gutenberg-Universität Mainz, 2023.
- [39] H. Merkel. *MAGNET DESIGN CONSIDERATIONS*. presentation at the MAGIX meeting. 2019.

- [40] J. Müller. “Entwurf eines Spektrometers für Niederenergieexperimente an MESA”. Diploma Thesis. Johannes Gutenberg-Universität Mainz, 2014.
- [41] H. Kolanoski and N. Wermes. *Teilchendetektoren*. Springer, 2016. ISBN: 978-3-662-45350-6.
- [42] G. Ranucci. *Gaseous Detectors*. June 11, 2016. URL: https://www.desy.de/~garutti/LECTURES/ParticleDetectorSS12/L4_gasDetectors.pdf#page=2&zoom=auto,-211,10.
- [43] F. Sauli. *Gaseous Radiation Detectors - Fundamentals and Applications*. Springer-Verlag GmbH, 2022. ISBN: 978-1-009-29121-7.
- [44] *Radiology Key Website*. URL: <https://radiologykey.com/gas-filled-detectors/> (visited on 09/20/2021).
- [45] S.Fechner. “Digital Twin of a 4-stage GEM Time Projection Chamber”. Master’s Thesis. Johannes Gutenberg-Universität Mainz, 2025.
- [46] M.C. Arena et al. “Recuperation systems for fluorinated gases at the CERN LHC Experiments”. In: *Nuclear Instruments and Methods in Physics Research Section A: Accelerators, Spectrometers, Detectors and Associated Equipment* 1068 (2024), p. 169789. ISSN: 0168-9002. DOI: <https://doi.org/10.1016/j.nima.2024.169789>. URL: <https://www.sciencedirect.com/science/article/pii/S0168900224007150>.
- [47] C. Szyszka. “Bestimmung und Überwachung von Gasparametern einer Zeitprojektionskammer bei MAGIX”. Bachelor’s Thesis. Johannes Gutenberg-Universität, 2020.
- [48] S. Caiazza. “The GridGEM module: a new GEM based readout module for a large TPC”. PhD thesis. University Hamburg, 2018.
- [49] J. Rausch. “Aufbau und Vermessung eines Spurendriftkammer-Prototypen für MAGIX”. Master’s Thesis. Johannes Gutenberg-Universität Mainz, 2019.
- [50] H. Spieler. *Analog and Digital Electronics for Detectors*. URL: <https://www.desy.de/~garutti/LECTURES/ParticleDetectorSS12/spieler.pdf>.
- [51] University of Warwick. *Light Emitting Diodes*. URL: <https://warwick.ac.uk/fac/sci/physics/current/postgraduate/regs/mpagswarwick/ex5/devices/led/>.
- [52] W. Demtröder. *Experimentalphysik 3*. Springer-Verlag GmbH, 2016. ISBN: 978-3-662-49094-5.
- [53] I. Mathews. “High-Efficiency Photovoltaics through Mechanically Stacked Integration of Solar Cells based on the InP Lattice Constant”. PhD thesis. May 2014.
- [54] E. F. Schubert. *Light-emitting diodes research, manufacturing, and applications*. Bellingham, Wash, 2001. ISBN: 978-0-8194-3956-7.
- [55] S. Nakamura et al. “High-Power GaN P-N Junction Blue-Light-Emitting Diodes”. In: *Japanese Journal of Applied Physics* 30.12A (1991), p. L1998. DOI: 10.1143/JJAP.30.L1998. URL: <https://dx.doi.org/10.1143/JJAP.30.L1998>.
- [56] A. Einstein. “Über einen die Erzeugung und Verwandlung des Lichtes betreffenden heuristischen Gesichtspunkt”. In: *Annalen der Physik* 322.6 (1905), pp. 132–148. DOI: 10.1002/andp.19053220607.

- [57] W. Demtröder. *Experimentalphysik 2*. Springer-Verlag GmbH, 2008. ISBN: 9783540682196.
- [58] C. N. Berglund and W. E. Spicer. “Photoemission Studies of Copper and Silver: Theory”. In: *Phys. Rev.* 136 (4A 1964), A1030–A1044. DOI: 10.1103/PhysRev.136.A1030. URL: <https://link.aps.org/doi/10.1103/PhysRev.136.A1030>.
- [59] D. Markus. “Effizienz und Auflösung des MAGIX TPC Prototypen”. Master’s Thesis. Johannes Gutenberg-Universität Mainz, 2021.
- [60] *Manufacturer website for Araldite 2011*. URL: <https://products.huntsman.com/products/araldite-2011-a-b> (visited on 02/05/2026).
- [61] F. Guarino et al. “Compilation of radiation damage test data - Part IV: Adhesives”. In: *Computer Physics Communications* (2001). ISSN: 0007-8328. URL: <https://cds.cern.ch/record/531818/files/CERN-2001-006.pdf>.
- [62] H. Merkel. *Electron Scattering - Simulation*. Presentation at the MAGIX Mainz Meeting.
- [63] *Manual for EHS on iseg website*. URL: https://iseg-hv.com/files/media/docitems_file_20250424121904.pdf (visited on 01/14/2026).
- [64] *Manual for CC on iseg website*. URL: https://iseg-hv.com/files/media/docitems_file_20240701110032.pdf (visited on 01/14/2026).
- [65] *Manual for ECH on iseg website*. URL: https://iseg-hv.com/files/media/docitems_file_20240314093107.pdf (visited on 01/14/2026).
- [66] B.S. Schlimme. *Private Kommunikation*. Oct. 29, 2021.
- [67] A. Marinov. *Status of no-stretch no-spacer GEM assembly. The NS2 Technique Method and experimental result*. URL: https://indico.cern.ch/event/176664/contributions/1442160/attachments/229650/321300/The_NS2_Technology.pdf.
- [68] L. Bister. “Inbetriebnahme der GEM Amplification Stage für die MAGIX TPC”. Bachelor’s Thesis. Johannes Gutenberg-Universität Mainz, 2024.
- [69] P. Gülker. “TBA”. Dissertation. Johannes Gutenberg-Universität Mainz, 2027.
- [70] G. Iakovidis. *The VMM ASIC*. URL: https://indico.cern.ch/event/1051087/contributions/4416280/attachments/2267328/3849776/2021_06_17_Iakovidis_VMM_RD51.pdf. 2021.
- [71] L. et al Scharenberg. “Development of a high-rate scalable readout system for gaseous detectors”. In: *Journal of Instrumentation* 17.12 (Dec. 2022), p. C12014. DOI: 10.1088/1748-0221/17/12/C12014. URL: <https://doi.org/10.1088/1748-0221/17/12/C12014>.
- [72] H. Merkel. *FIELD CAGE AND CONSTRUCTION*. presentation at the MAGIX meeting. 2021.
- [73] T2K ND280 TPC collaboration. *Time Projection Chambers for the T2K Near Detectors*. 2010. eprint: 1012.0865. URL: <https://arxiv.org/abs/1012.0865>.

- [74] D. Schaab. “Entwicklung einer Spurkammer für das Studium von Driftfeld-Kalibrationsmethoden”. Dissertation. Rheinische Friedrich-Wilhelms-Universität Bonn, 2021.
- [75] J. Laulainen et al. “Photoelectron emission from metal surfaces induced by VUV-emission of filament driven hydrogen arc discharge plasma”. In: *AIP Conference Proceedings*. Vol. 1655. AIP Publishing LLC, 2015, p. 020007. DOI: 10.1063/1.4916416. URL: <http://dx.doi.org/10.1063/1.4916416>.
- [76] J. Geimer. “Neues Verfahren zur Kalibration eines GEM-Detektors für das MAGIX-Experiment”. Bachelor’s Thesis. Johannes Gutenberg-Universität Mainz, 2018.
- [77] D. Steger. “Prototypentwicklung eines Kalibrierungssystems für die Spurendriftkammer am MAGIX”. Bachelor’s Thesis. Johannes Gutenberg-Universität Mainz, 2022.
- [78] D. Kieber et al. “Wavelength and temperature-dependent apparent quantum yields for photochemical formation of hydrogen peroxide in seawater”. In: *Environmental science. Processes & impacts* 16 (Mar. 2014). DOI: 10.1039/c4em00036f.
- [79] UVP Website. *DBA Analytik Jena US. PEN-RAY LAMP SPECTRA*. 2025. URL: https://www.uvp.com/fileadmin/content/products/UVP_Pen-Ray_Lamps/Rare_Gas_Lamp_Spectra.pdf.
- [80] J. Gorobez et al. “Growth of Self-Passivating Oxide Layers on Aluminum—Pressure and Temperature Dependence”. In: *physica status solidi (b)* 258.5 (2021), p. 2000559. DOI: <https://doi.org/10.1002/pssb.202000559>. URL: <https://onlinelibrary.wiley.com/doi/abs/10.1002/pssb.202000559>.
- [81] L. Nguyen et al. “Atomic-Scale Insights into the Oxidation of Aluminum”. In: *ACS Applied Materials & Interfaces* 10.3 (2018), pp. 2230–2235. DOI: 10.1021/acsami.7b17224. URL: <https://doi.org/10.1021/acsami.7b17224>.
- [82] Daniel Franta et al. “Dispersion model for optical thin films applicable in wide spectral range”. In: *Optical Systems Design 2015: Optical Fabrication, Testing, and Metrology V*. Ed. by A. Duparré and R. Geyl. Vol. 9628. International Society for Optics and Photonics. SPIE, 2015, 96281U. DOI: 10.1117/12.2190104. URL: <https://doi.org/10.1117/12.2190104>.
- [83] *Fused Quartz Information at PGO*. URL: <https://www.pgo-online.com/de/natuerliches-quarzglas.html> (visited on 01/02/2026).
- [84] *magtec coating solutions website*. URL: <https://magtec-cs.de/> (visited on 01/02/2026).
- [85] R. G. Wilson. “Vacuum Thermionic Work Functions of Polycrystalline Nb, Mo, Ta, W, Re, Os, and Ir”. In: *Journal of Applied Physics* 37.8 (July 1966), pp. 3170–3172. ISSN: 0021-8979. DOI: 10.1063/1.1703180. URL: <https://doi.org/10.1063/1.1703180>.
- [86] Laser Components. *Data Sheet of the PKB-10-F35 LED*. URL: <https://datasheet.octopart.com/PKB-10-F35-Laser-Components-datasheet-180553338.pdf>.

- [87] P.A. Anderson. “The Work Function of Copper”. In: *Phys. Rev.* 76 (3 Aug. 1949), pp. 388–390. DOI: 10.1103/PhysRev.76.388. URL: <https://link.aps.org/doi/10.1103/PhysRev.76.388>.
- [88] D. Steger. “A Starry Night for MAGIX Time Projection Chamber”. Master’s Thesis. Johannes Gutenberg-Universität Mainz, 2025.
- [89] *Website of the EPICS collaboration*. URL: <https://epics-controls.org/> (visited on 10/11/2021).
- [90] *Root Website at CERN*. URL: <https://root.cern/> (visited on 10/26/2021).
- [91] TPC group. *internal communication*. 2025.
- [92] L. Bister. “To be released”. Master’s Thesis. Johannes Gutenberg-Universität Mainz, 2026.
- [93] F. Hoyle. “On Nuclear Reactions Occuring in Very Hot Stars. 1. The Synthesis of Elements from Carbon to Nickel”. In: *Astrophys. J. Suppl.* 1 (1954), pp. 121–146. DOI: 10.1086/190005.
- [94] C. W. Cook et al. “B¹², C¹², and the Red Giants”. In: *Phys. Rev.* 107 (2 July 1957), pp. 508–515. DOI: 10.1103/PhysRev.107.508. URL: <https://link.aps.org/doi/10.1103/PhysRev.107.508>.
- [95] M. Freer and H.O.U. Fynbo. “The Hoyle state in ¹²C”. In: *Progress in Particle and Nuclear Physics* 78 (2014), pp. 1–23. ISSN: 0146-6410. DOI: <https://doi.org/10.1016/j.pnpnp.2014.06.001>. URL: <https://www.sciencedirect.com/science/article/pii/S0146641014000453>.
- [96] E. E. Salpeter. “52. Nuclear Reactions in Stars without Hydrogen”. In: *A Source Book in Astronomy and Astrophysics, 1900–1975*. Cambridge, MA and London, England: Harvard University Press, 1979, pp. 349–352. ISBN: 9780674366688. DOI: doi:10.4159/harvard.9780674366688.c57. URL: <https://doi.org/10.4159/harvard.9780674366688.c57>.
- [97] M. Chernykh. “Electron Scattering on C¹², the Structure of the Hoyle State and a Neutron Ball for (e,e’n) Experiments at the S-DALINAC”. Dissertation. Technische Universität Darmstadt, 2008.
- [98] *American Elements Website*. URL: <https://www.americanelements.com/pyrolytic-graphite-7782-42-5> (visited on 11/18/2025).
- [99] L. Zehnder. “Ein neuer Interferenzrefraktor”. In: *Zeitschrift für Instrumentenkunde* 11 (1891), pp. 275–285.
- [100] L. Mach. “Über einen Interferenzrefraktor”. In: *Zeitschrift für Instrumentenkunde* 12 (1892), pp. 89–93.
- [101] D. Kajtoch. “Novel schemes for generation of strongly squeezed atomic states”. PhD thesis. University of Warsaw, June 2015.
- [102] H. R. Phillip and E. A. Taft. “Kramers-Kronig Analysis of Reflectance Data for Diamond”. In: *Phys. Rev.* 136 (5A Nov. 1964), A1445–A1448. DOI: 10.1103/PhysRev.136.A1445. URL: <https://link.aps.org/doi/10.1103/PhysRev.136.A1445>.

- [103] J. Heisenberg. “Nuclear Transition Density Determinations from Inelastic Electron Scattering”. In: *Advances in Nuclear Physics*. Ed. by J. W. Negele and Erich Vogt. Boston, MA: Springer US, 1981, pp. 61–133. ISBN: 978-1-4613-9889-9. DOI: 10.1007/978-1-4613-9889-9_2. URL: https://doi.org/10.1007/978-1-4613-9889-9_2.
- [104] H. Theissen. *Springer Tracts in Modern Physics - Spectroscopy of light nuclei by low energy (< 70 MeV) inelastic electron scattering*. Springer, 1972. ISBN: 978-3-540-37527-2.
- [105] D.H. Wilkinson. “Evaluation of E0 pair transitions”. In: *Nuclear Physics A* 133.1 (1969), pp. 1–9. ISSN: 0375-9474. DOI: [https://doi.org/10.1016/0375-9474\(69\)90444-8](https://doi.org/10.1016/0375-9474(69)90444-8). URL: <https://www.sciencedirect.com/science/article/pii/0375947469904448>.
- [106] D. Markus. “Simulation zur radiativen Korrekturen bei der Elektron-Proton-Streuung an MAGIX”. Bachelor’s Thesis. Johannes Gutenberg-Universität Mainz, 2019.
- [107] *Git Repository for Cola++*. URL: <https://gitlab.rlp.net/kph-a1-software/cola/-/tree/master/Cola> (visited on 07/01/2025).
- [108] W. Reuter et al. “Nuclear charge distribution and rms radius of ^{12}C from absolute elastic electron scattering measurements”. In: *Phys. Rev. C* 26 (3 Sept. 1982), pp. 806–818. DOI: 10.1103/PhysRevC.26.806. URL: <https://link.aps.org/doi/10.1103/PhysRevC.26.806>.
- [109] F. Salvat, A. Jablonski, and C.J. Powell. “elsepa—Dirac partial-wave calculation of elastic scattering of electrons and positrons by atoms, positive ions and molecules”. In: *Computer Physics Communications* 165.2 (2005), pp. 157–190. ISSN: 0010-4655. DOI: <https://doi.org/10.1016/j.cpc.2004.09.006>. URL: <https://www.sciencedirect.com/science/article/pii/S0010465504004795>.
- [110] *ELSEPA GitHub*. URL: <https://github.com/eScatter/elsepa> (visited on 10/16/2025).
- [111] J Heisenberg and H P Blok. “Inelastic electron scattering from nuclei”. In: *Annu. Rev. Nucl. Sci.; (United States)* 33:1 (Dec. 1982). ISSN: ISSN ARNUA. DOI: 10.1146/annurev.ns.33.120183.003033. URL: <https://www.osti.gov/biblio/6581436>.
- [112] N. Hesse. “Particle track classification using a Long Short-Term Memory Neural Network at MAGIX”. Bachelor’s Thesis. Johannes Gutenberg-Universität Mainz, 2024.
- [113] *Definition of the Crystal Ball function used by ROOT*. URL: <https://root.cern.ch/doc/v636/classRooCrystalBall.html> (visited on 01/14/2026).
- [114] T. Kolar. “ANALIZA NEELASTIČNEGA SIPANJA ELEKTRONOV NA OGLJIKOVH JEDRIH”. Master’s Thesis. UNIVERZA V LJUBLJANI FAKULTETA ZA MATEMATIKO IN FIZIKO, 2016.
- [115] M. Chernykh et al. “Structure of the Hoyle State in ^{12}C ”. In: *Phys. Rev. Lett.* 98 (3 Jan. 2007), p. 032501. DOI: 10.1103/PhysRevLett.98.032501. URL: <https://link.aps.org/doi/10.1103/PhysRevLett.98.032501>.

Lebenslauf

Persönliche Daten **David Christian Alexander Gabriel Markus**
geboren am 19. Juni 1998 in Haan
Adresse Willi-Wolf Straße 5, 55128 Mainz
Email: dmarkus@uni-mainz.de
Mobil 01522 - 23319319

Studium

10/2016 – 09/2019 Bachelorstudium Physik, Johannes Gutenberg-Universität Mainz,
Thema der Bachelorarbeit: Simulation zu radiativen
Korrekturen bei der Elektron-Proton-Streuung an MAGIX
10/2019 – 12/2021 Masterstudium Physik, Johannes Gutenberg-Universität Mainz,
Thema der Masterarbeit: Effizienz und Auflösung
des MAGIX TPC Prototypen
3/2022 - 3/2026 Promotionsstudium Physik, Johannes Gutenberg-Universität Mainz

Schulbildung

08/2004 – 07/2006 Grundschule Sechseckschule, Erkrath
08/2006 – 07/2008 Gemeinschaftsgrundschule Gruiten, Haan
08/2008 – 07/2016 Städtisches Konrad-Heresbach-Gymnasium, Mettmann